

Distributed Voltage-driven Demand Response: Flexibility, Stability and Value Assessment

Jinrui Guo

Department of Electrical and Electronic Engineering
Imperial College London

This dissertation is submitted for the degree of
Doctor of Philosophy

June 2020

*Dedicated to
my loving families*

Declaration of Originality

I hereby confirm that this thesis is the result of my own research work; and, where appropriate, contributions from other people have been properly acknowledged.

Jinrui Guo
June 2020

Copyright Declaration

The copyright of this thesis rests with the author and is made available under a Creative Commons Attribution Non-Commercial No Derivatives licence. Researchers are free to copy, distribute or transmit the thesis on the condition that they attribute it, that they do not use it for commercial purposes and that they do not alter, transform or build upon it. For any reuse or redistribution, researchers must make clear to others the licence terms of this work.

Jinrui Guo
June 2020

Acknowledgements

Firstly, I would like to express my sincere gratitude to my supervisor Dr Balarko Chaudhuri for the continuous support of my Ph.D. study and related research, for his patience, understanding, and immense knowledge. His guidance shaped my mind and helped me become a better person. I could never imagine having a better advisor and mentor than him.

I am also very grateful to Professor Shu Yuen Ron Hui and Dr Fei Teng for all the helpful discussions and suggestions along the way. I would like to take this opportunity to thank my collaborators Dr Diptargha Chakravorty, Mr Tong Chen and Mr Luis Badesa for their insights and help.

Many thanks also goes to Professor Jihong Wang and Professor Tim Green for being my examiners under such a difficult situation (COVID-19 pandemic). Their insightful and valuable suggestions have helped me immensely to improve the thesis.

I would like to acknowledge Imperial College London and China Scholarship Council for supporting my studies, as I would not have accomplished this without their sponsorship.

I feel so fortunate to all the friends I made in the Control & Power group. Time at Imperial would not have been so fabulous and memorable without you guys.

Finally, I owe my biggest gratitude to my parents and my aunt. Without their loving care and constant encouragement, I would not have been able to achieve this.

Abstract

The need for operating reserve from energy storage, demand reduction (DR) etc. is expected to increase significantly in future low-carbon Great Britain (GB) power system with high penetration of non-synchronous renewable generation. One way to provide the reserve is to use power electronic compensators (PECs) for point-of-load voltage control (PVC) to exploit the voltage dependence of loads.

This thesis focuses on the quantification of DR capability from PVC in the domestic sector using high-resolution stochastic demand models and generic distribution networks in GB. The effectiveness of utilising PVC in contributing to frequency regulation is analysed and demonstrated through time domain simulations. The techno-economic feasibility of such technology is evaluated considering the investment cost of the PEC deployment as well as the economic and environmental benefits of using PVC. The payback period varies between 0.3 to 6.7 years for different future scenarios considering a range of converter price. It is demonstrated that PVC could effectively complement battery energy storage system towards enhanced frequency response provision in future GB power system.

For practical application of PVC for flexible demand and voltage regulation in future distribution networks/microgrids, it is important to investigate the overall small signal stability of the system. In this thesis, the linearised state space model of a distribution network/isolated microgrid with converter-interfaced distributed generators (CDGs) working in grid following mode along with loads with PVC is developed. The stability performance is revealed through both modal analysis and time domain simulations. It is shown that multiple loads with PVC for voltage regulation in distribution networks are not likely to threaten the small signal stability of the system. In the case of a microgrid, the introduction of PVC is shown to have marginal impact on the low frequency modes associated with the droop control of the CDGs. However, there is a trade-off when choosing the droop gain of the loads with PVC. Lower droop gains could ensure better frequency regulation in face of intermittent renewables but at the expense of a lower stability margin for an oscillation mode at a frequency slightly higher than 20Hz.

Table of Contents

List of Figures	xvii
List of Tables	xxi
Notation	xxiii
1 Introduction	1
1.1 Motivation	1
1.2 Background and Literature Review	2
1.2.1 Demand Side Response	2
1.2.2 Point-of-load Voltage Control	5
1.2.3 System Stability with Point-of-load Voltage Control for Voltage Regulation	9
1.2.4 System Stability with Point-of-load Voltage Control for Flexible Demand	10
1.3 Outline and Contributions	11
1.4 List of Publications	13
2 Flexible Demand from Point-of-load Voltage Control	15
2.1 Demand Reduction	16
2.2 Power Electronic Compensator	20
2.3 Generic Low Voltage Feeder	22
2.3.1 Domestic Demand Model	23
2.3.2 Demand Reduction Capability	25
2.3.3 Power Electronic Compensator Power	29
2.3.4 Sensitivity Analysis	30
2.4 CIGRE Benchmark MV/LV Network	32
2.4.1 Network Description	32

2.4.2	Demand Reduction Capability	34
2.4.3	Power Electronic Compensator Rating	36
2.5	Conclusion	37
3	Value of Point-of-load Voltage Control in Great Britain Power System	39
3.1	Estimation of Enhanced Frequency Response from Point-of-load Voltage Control	40
3.1.1	Approach	40
3.1.2	Enhanced Frequency Response Capability with Point-of-load Voltage Control	43
3.1.3	Investment in Power Electronic Compensators	46
3.2	Value of Enhanced Frequency Response from Point-of-load Voltage Control	46
3.2.1	Methodology	47
3.2.2	Scenarios	49
3.2.3	Point-of-load Voltage Control in Normal Mode	50
3.2.4	Point-of-load Voltage Control in Fully Controllable Mode	55
3.2.5	Impact of Battery Energy Storage System	58
3.3	Conclusion	59
4	Virtual Inertia from Point-of-load Voltage Control	61
4.1	Load-side Virtual Inertia	61
4.2	Test Case: CIGRE Benchmark Microgrid	64
4.2.1	System Description	65
4.2.2	Estimated Virtual Inertia from Point-of-load Voltage Control	65
4.2.3	Time Domain Verification	67
4.3	Conclusion	69
5	System Stability with Point-of-load Voltage Control for Voltage Regulation	71
5.1	Vector Control of an PVC-Q	72
5.1.1	Choice of Reference Frame (d -axis)	72
5.1.2	Current Control Loop	74
5.1.3	Point of Coupling Voltage Control Loop	75
5.1.4	Phase-Locked Loop	77
5.1.5	DC Link Control Loop	77
5.1.6	Performance Validation	77
5.2	Linearised State Space Model of an PVC-Q	79
5.2.1	Phase-Locked Loop	80

5.2.2	Point of Coupling Voltage Control Loop	80
5.2.3	Current Control Loop	82
5.2.4	Filter	83
5.2.5	Network and Loads	84
5.2.6	Validation of Linearised State Space Model	86
5.3	Frequency Domain Analysis	87
5.3.1	Distance from Substation	89
5.3.2	Electrical Proximity	89
5.3.3	Distribution Network Voltage Level	90
5.4	Conclusion	92
6	System Stability with Point-of-load Voltage Control for Flexible Demand	93
6.1	Isolated Microgrid with Smart Loads	94
6.1.1	Operation of Smart Loads	94
6.1.2	Control of Smart Loads	95
6.1.3	Performance vs. Stability	97
6.2	Linearised State Space Model	99
6.2.1	DC Link and its Voltage Controller	99
6.2.2	Current Controller of the Shunt Converter	100
6.2.3	Shunt Converter Filter	100
6.2.4	Voltage-dependent Load	101
6.2.5	Overall Model	103
6.2.6	Validation	103
6.3	Stability Analysis	103
6.3.1	Modal Analysis	103
6.3.2	Droop Gain of Smart Load	106
6.3.3	Phase-Locked Loop	107
6.3.4	Line Parameters	109
6.3.5	Voltage Controller Gain of Series Converter	110
6.3.6	Active Power Voltage Sensitivity of Smart Load	110
6.4	Conclusion	112
7	Summary and Future Work	113
7.1	Summary of Contributions	113
7.2	Future Work	114
	References	117

Appendix A	Derivation of Equation (2.2)	129
Appendix B	Summary of Generator Parameters	131
Appendix C	Equivalent DG Models	133
Appendix D	System Parameters	135
Appendix E	Eigen Values and Participation Factors for IMG with a SL	137

List of Figures

1.1	Comparison between conservation voltage reduction (CVR) with line drop compensation (LDC), mid-feeder compensation (MFC) and point-of-load voltage control (PVC)	6
1.2	(a) PVC with reactive power compensation only (PVC-Q) (b) PVC with back-to-back configuration (PVC-B2B)	7
2.1	Variation of ΔDR and DR capability with loading level	19
2.2	Power electronic compensator (PEC) for point-of-load voltage control (PVC)	21
2.3	Incidence of appliances within a household over a typical (a) winter weekday; (b) summer weekday	23
2.4	Numerical comparison of the power consumption of 50 customers at V_{min} .	25
2.5	Calculation of demand reduction capability	26
2.6	Aggregate active power consumption and active power-voltage exponent at CDCs for winter and summer weekdays	27
2.7	Voltage across CDCs for winter and summer weekdays	28
2.8	Demand reduction (DR) capability of PVC and comparison with that of VCS (ΔDR) for winter and summer weekdays	29
2.9	Total apparent power processed by the power electronic compensators (PECs) for winter and summer weekdays	30
2.10	Impact of loading level on demand reduction (DR) capability and PEC rating required	31
2.11	Impact of number of CDCs on demand reduction (DR) capability	31
2.12	CIGRE LV/MV benchmark network	33
2.13	Aggregate active power consumption and active power-voltage exponent at CDCs for winter and summer weekdays	34
2.14	Voltage across CDCs for winter and summer weekdays	35
2.15	Demand reduction (DR) capability of PVC and comparison with that of VCS (ΔDR) for winter and summer weekdays	35

2.16	Rating of power electronic compensators (PECs) at different buses across all the LV feeders with 155 clusters of domestic customers (CDCs)	36
3.1	An outline for estimating EFR from PVC in the urban domestic sector across GB	40
3.2	GB generic urban distribution network MV model	41
3.3	Demand profiles of a CDC as well as EV and HP loads for a typical winter day (a) Smart Case; (b) Non-Smart Case	42
3.4	Voltage across CDCs for the 2030 GnW ‘Smart Case’	44
3.5	Comparison between EFR with PVC and EFR with VCS for the 2030 GnW ‘Smart Case’	45
3.6	Example of a scenario tree used in the SUC model	47
3.7	Operation cost and payback period for (a) 2030 GnW Non-Smart Case; (b) 2030 GnW Smart Case; (c) 2030 SwP Non-Smart Case; (d) 2030 SwP Smart Case	51
3.8	24-hour dispatch profile for different types of generation and frequency response for a day with low net-demand in 2030 GnW SC	52
3.9	24-hour dispatch profile for different types of generation and frequency response for a day with high net-demand in 2030 GnW SC	53
3.10	Average wind curtailment (% of available wind) for (a) 2030 GnW Non-Smart Case; (b) 2030 GnW Smart Case; (c) 2030 SwP Non-Smart Case; (d) 2030 SwP Smart Case	54
3.11	Avoided CO ₂ emissions (g/kWh) for (a) 2030 GnW Non-Smart Case; (b) 2030 GnW Smart Case; (c) 2030 SwP Non-Smart Case; (d) 2030 SwP Smart Case	55
3.12	Operation cost and payback period for 2030 GnW Smart Case under normal (Case A) and fully controllable cases (Case B)	56
3.13	Correlation between the urban domestic sector consumption and system net demand (with 0.5GW BESS, 100% of urban domestic loads with PVC) (a)winter; (b)spring; (c)summer; (d)autumn	57
3.14	Impact of BESS on the economic value of EFR provision from PVC, for two different ratings of the BESS: 0.5GW and 1GW	58
3.15	Correlation between the urban domestic sector consumption and system net demand (with 1GW BESS, 100% of urban domestic loads with PVC) (a)winter; (b)spring; (c)summer; (d)autumn	59
4.1	Block diagram of a generator supplying a load with PVC-B2B	63

4.2	Block diagram of system frequency with equivalent effect of PVC	65
4.3	Equivalent inertia for (a) winter weekdays and (b) summer weekdays	66
4.4	(a) Frequency and (b) load-side voltage response before and after sudden disconnection of 50% of wind generation	67
4.5	Frequency response under wind fluctuations	68
5.1	PVC-Q configuration	72
5.2	Phasor diagram with d -axis aligned with PoC voltage	73
5.3	Phasor diagram with d -axis aligned with filter capacitor voltage	74
5.4	PoC voltage control scheme	76
5.5	Bode plot and step response of the PoC voltage control loop	76
5.6	Test system for validation of PoC voltage controller	78
5.7	Dynamic response of (a) PoC, load and injected voltages; (b) inverter, load and filter capacitor current; (c) RMS value of PoC voltage and (d) DC link voltage	78
5.8	Injected voltage (V_c) and load current (I_{nl}) (a) before the disturbance (inductive mode) and (b) after the disturbance (capacitive mode)	79
5.9	Block diagram of (a) PoC and (b) load voltage control loops	81
5.10	Comparison of dynamic response of state variables in linearised state space model and non-linear model due to a small disturbance	87
5.11	Study system with two PVC-Qs used for frequency-domain analysis	88
5.12	Root locus with (a) PVC-Q and (b) DG inverters when length of L1 & L2 is varied from 0.1km to 2km (red to blue) while keeping the other line parameters constant	89
5.13	Root locus with (a) PVC-Q and (b) DG inverters when length of L3 is varied from 0.1km to 2km (red to blue) while keeping the other line parameters constant	90
5.14	Root locus with (a) PVC-Q and (b) DG inverters when R/X ratios of L1 & L2 are varied from 1 to 10 (red to blue) while keeping the other line parameters constant	91
5.15	Root locus plot with (a) PVC-Q and (b) DG inverters when R/X ratio of L3 is varied from 1 to 10 (red to blue) while keeping the other line parameters constant	91
6.1	A smart load (SL) with a series-shunt converter arrangement of voltage compensator (VC)	94
6.2	Control of series and shunt converter (SeC and ShC) of a smart load	95

6.3	(a) Relation between V_{cd} and system frequency for different droop gains; (b) droop characteristic of a converter-interfaced distributed generator (CDG) and smart load (SL)	97
6.4	An isolated microgrid (IMG) test system with two converter-interfaced distributed generators (CDGs) fuelled by wind and solar PV with battery energy storage and a smart load (SL)	97
6.5	Dynamic response of (a) microgrid frequency; (b) Active power output of CDG1; (c) RMS value of SL's load voltage; (d) DC-link voltage	98
6.6	Comparison of dynamic response from the linearised state space model (LSSM) and non-linear simulation model	104
6.7	Participation factor (PF) of dominant state variable in low frequency modes (a) Case1, Mode1; (b) Case2, Mode1; (c) Case3, Mode1; (d) Case3, Mode2	106
6.8	Impact of varying droop gain of SL between 0.001 and 0.1 (a) root locus plot; (b) participation factors for Mode 1	107
6.9	Impact of bandwidth of PLL on low frequency modes	108
6.10	Impact of cut-off frequency of PLL's low pass filter (LPF) (a) root locus; (b) participation factors in Mode 2	108
6.11	Impact of R/X ratio of Line1 on low frequency modes (a) root locus plot; (b) participation factors for Mode 1	109
6.12	Impact of R/X ratio of Line2 on low frequency modes (a) root locus plot; (b) participation factors for Mode 1	110
6.13	Impact of integral gain of voltage controller of the SeC on low frequency modes (a) root locus plot; (b) participation factors for Mode 1	111
6.14	Root locus plot with active power voltage sensitivity of smart load varying between 0 and 2	111
A.1	Electrical equivalent of a radial distribution network	129
B.1	(a) Block diagram of the turbine and governor; (b) Block diagram of the excitation system (IEEE DC1A)	131
C.1	Equivalent DG configuration	133
C.2	PoC voltage control scheme	134
C.3	Bode plot and step response of the PoC voltage control loop	134

List of Tables

1.1	Categories of Price based DSR schemes [1]	4
2.1	ZIP Load Model Coefficients	24
2.2	Parameter Range for Demand Reduction Calculation	26
3.1	Target voltage boost considering load drop compensation, where nominal target voltage is 1.0 p.u.	43
3.2	Characteristic of Main Thermal Plants	50
6.1	Low Frequency Oscillatory Modes with and without Smart Loads	105
6.2	State Variable Description	105
B.1	Parameters of the Isolated Microgrid (IMG)	132
D.1	Parameters of the Isolated Microgrid (IMG)	135
D.2	Parameters of the Smart Load	136
E.1	State Variable Description II	137
E.2	Oscillatory Modes of the Test System (Case 3)	138

Notation

Symbols

Indices and Sets

n, \mathcal{N}	Index Set of nodes in the scenario tree
g, \mathcal{G}	Index, Set of generators
s, \mathcal{S}	Index, Set of storage units

Constants and Parameters

$\Delta\tau(n)$	Time-step corresponding to node n (h)
$\pi(n)$	Probability of reaching node n
c^{ls}	Load shed penalty (£/MWh)
c_g^{st}	Startup cost of generating units g (£)
c_g^{nl}	No-load cost of generating units g (£/h)
c_g^{m}	Marginal cost of generating units g (£/MWh)
f_0	Nominal frequency of the power grid (Hz)
H_g	Inertia constant of generating units g (s)
H_L	Inertia constant of tripped generator (s)
P_g^{max}	Maximum power output of units g (MW)
P_L^{max}	Largest power infeed (MW)
$\text{RoCoF}_{\text{max}}$	Maximum admissible RoCoF (Hz/s)

Δf_{\max}	Maximum admissible frequency deviation (Hz)
p^D	Total demand besides urban domestic customers with PVC (MW)
p^{WN}	Total available wind generation (MW)
p_{\min}^{PVC}	Lower bound for p^{PVC} (MW)
p_{\max}^{PVC}	Upper bound for p^{PVC} (MW)
T_g	Delivery time of PFR (s)
T_e	Delivery time of EFR (s)
\bar{P}_s	Maximum discharge rate for battery storage

Decision Variables

$C_g(n)$	Operating cost of generator g in node n
$N_g^{sg}(n)$	Number of units g that start generating in node n
N_g^{up}	Number of online generating units of type g
H	Total system inertia (MW · s)
P_g	Power produced by generating units g (MW)
p^{LS}	Load shed (MW)
P_g	Power produced by generating units g (MW)
P_s	Power provided by storage units s (MW)
p^{PVC}	Power consumed by urban domestic customers with PVC (MW)
p^{WC}	Wind curtailment (MW)
$R_{\mathcal{G}}$	Total PFR from all generators (MW)
$R_{\mathcal{E}}$	EFR from battery storage units and PVC (MW)
EFR_s	EFR from battery storage units (MW)

PVC-related Variables

DR_{VCS}	DR capability using VCS
------------	-------------------------

DR_{PVC}	DR capability using PVC
EFR_{VCS}	EFR capability using VCS
EFR_{PVC}	EFR capability using PVC
I_l	CDC current
N_c, N_h	Number of CDCs/Number of domestic customers within a CDC
n_p, n_q	Aggregate active/reactive power-voltage sensitivity per CDC
n_{ph}	Aggregate active power-voltage sensitivity per domestic customer
m_{SL}	Droop gain of SL
P_d	Active power per appliance
P_h	Aggregate active power per domestic customer
P_l^*, Q_l^*	Nominal aggregate active/reactive power per CDC
P_l, Q_l	Aggregate active/reactive power per CDC
P_{LC}	Power loss incurred in the PEC
ΔP_{LL}	Change in network power loss after PVC
P_T	Total DPD at nominal voltage
pf'	Power factor after PVC
R_T	Total feeder resistance
S_c	Apparent power processed by the PEC
V_c	Voltage injected by the PEC
V_l	Load-side voltage
V_p, V'_p	Feeder-side voltage before/after PVC/VCS
V_s	Substation voltage
Z_p, I_p, P_p	ZIP load model coefficients for appliances

Acronyms / Abbreviations

BESS	Battery storage energy system
CDC	Cluster of domestic customers
CDG	Converter-interfaced distributed generator
DPD	Diversified peak demand
DR	Demand reduction
DSR	Demand side response
EFR	Enhanced Frequency Response
ES	Electric Springs
EV	Electric vehicle
GB	Great Britain
GnW	Great World
HP	Heat pump
IMG	Isolated (or Islanded/Autonomous) microgrid
LPF	Low-pass filter
LSSM	Linearised state space model
LV	Low voltage
MV	Medium voltage
ND	Net demand
PEC	Power electronic compensators
PF	Participation factor
PFR	Primary Frequency Response
PoC	Point of coupling
PP	Payback period
PVC	Point-of-load voltage control

PVC-Q	Point-of-load voltage control with reactive power compensation only
PVC-B2B	Point-of-load voltage control with back-to-back configuration
SeC	Series converter of PVC-B2B
ShC	Shunt converter of PVC-B2B
SL	Smart load
SwP	Slow Progression
SUC	Stochastic unit commitment
UB, LB	Upper, Lower boundary
VCS	Voltage control at the substation

Chapter 1

Introduction

1.1 Motivation

Climate change due to greenhouse gas emissions has become a major concern in human society. As reported by the Intergovernmental Panel on Climate Change (IPCC) [2], human activities are estimated to have caused about 1.0° of global warming above pre-industrial levels. This number is expected to reach 1.5° between year 2030 and 2052 if the current rate of increase continues.

According to the UK's Clean Growth Strategy, the fifth carbon budget (2028–2032) targets a 57% average reduction in greenhouse gas emissions compared to the baseline of 1990 [3]. To achieve this goal, it would require integration of large amounts of intermittent renewable energy sources (e.g. wind and solar power) on the electricity supply side and significant level of electrification in transportation and heating sectors on the consumption side. As a result, the level of distributed generators (DGs) penetration in distribution networks (especially roof-top photovoltaic (PV)) and the number of electric vehicles (EVs) have gained a remarkable increase. As reported by Department for Business, Energy & Industrial Strategy, overall UK solar PV capacity has stood at 13,356 MW across 1,025,044 installations by the end of December 2019 [4]. More than 72,700 electric cars have been sold during 2019, increased by over 20% compared to the figure of 2018 [5].

Both high penetration of the renewables and growing numbers of EVs could bring in many challenges in the stable operation of the power grid such as balancing the supply and demand, over or under voltage problems etc. due to the intermittencies and uncertainties. Besides, renewable energy sources (RESs) would also lead to a drastic decrease in system inertia as

they are interfaced through non-synchronous power electronic compensators (PECs).

To deal with those challenges, PECs such as Electric Springs (ESs) [6], soft open points [7], mid feeder compensation [8] which can provide active and reactive power control as well as voltage regulation have been proposed and seem quite promising in future distribution network operation. ESs are newly invented electronics equipment that can be connected in series with a single load or a cluster of customers, presenting a new approach for demand side response (DSR) through point-of-load voltage control (PVC). Applications of ESs, such as smoothing fluctuations [9], providing voltage and frequency support [10–21], reducing energy storage [22] as well as improving power quality [20, 21, 23–26] have been widely proposed and demonstrated in previous literature.

However, present studies are mostly ‘proof of concept’ using simple impedance-type load models and ignores the diurnal and seasonal loading variations. Thereby, the capabilities and value of PVC still require further investigation for practical application. On the other hand, unexpected stability issues could arise with an increasing penetration of PECs interfaced applications. The small signal stability of multiple loads equipped with PVC in a distribution network/isolated microgrid should be systematically evaluated before they can be fully put into practice.

1.2 Background and Literature Review

This section presents summary of several research topics associated with the study of this thesis, including state of the art in DSR, PVC via PECs and possible instabilities induced by PVC through PECs in distribution networks/isolated microgrids.

1.2.1 Demand Side Response

Demand side response (DSR) is about intelligent use of energy, including all kinds of intentional modifications to the electricity consumption patterns from the timing, level of instantaneous demand to the total electricity consumption [27]. Office of Gas and Electricity Markets (Ofgem) foresees aggregated DSR from domestic sector to be capable of providing significant level of flexibility to the system in future [28]. Depending on the attribute of the control signal, DSR can be broadly distinguished into: (a) price signal based and (b) physical signal based.

Price Signal Based

Price signal based DSR, including time-of-use pricing (ToUP), critical peak pricing (CPP) and real-time pricing (RTP) etc., is commonly associated with energy arbitrage or peak shaving. The fundamental idea of ToUP is to let demand follow the diurnal and seasonal variations of electricity provision cost. Typical structure of a ToUP comprises a peak rate, an off-peak rate and possibly a shoulder-peak rate for predefined periods of time [29, 30]. The price signal would be sent to the customers and the change in demand can be realised manually (decided by the customer) or automatically as pre-programmed. CPP is also a tiered rate scheme but designed for critical periods for power system, such as extreme weather conditions or low availability of reserves. Customers would be informed of the high price in advance when the system meets certain criteria triggering the CPP [31, 32].

Compared to ToUP and CPP, RTP scheme updates the price information in a very short notice, say hourly or less, which reflects the variations in the cost of electricity production over time in a more effective and accurate way [33]. The popularity of smart meters in recent years makes it possible for RTP implementation. In an example of RTP program led by Midcontinent ISO (MISO), customers are directly charged according to the day-ahead market price [34].

A more comprehensive summary of price based DSR schemes is given in Table 1.1 [1], many of which have already been implemented or trialled. It is to be noted that implementation of these price based schemes relies on infrastructure like smart metering. Although all households will be offered a smart meter by 2020 according to the Smart Metering Implementation Programme (SMIP) [35], the smart meter roll-out is still an important constraint for domestic DSR engagement, as pointed out by [36]. The capability of DSR provision also depends on the usage patterns of appliances and this is expected to be much higher in the future with increasing electrification in transportation [37] and heating sectors [38] as well as prevalence of smart appliances [39].

Physical Signal Based

Physical signal based DSR is usually related with contributing to grid operation enhancement such as voltage problem mitigation, congestion management and emergency control. DSR approaches like interruptible loads [40] and direct load control (DLC) [41] can fall into this category, in which cases the utilities pay for the right to control the demand consumption

Table 1.1 Categories of Price based DSR schemes [1]

Price based schemes	Description
Static time-of-use (sToUP)	Prices vary by time-of-use between fixed price levels and over fixed periods. May also vary by season
Critical Peak Pricing (CPP)	Prices increase by a known amount during specified system operating or market conditions. This applies during a narrowly defined period and is usually applied only during a limited number of days in the year
Time-of-use critical peak pricing (ToU-CPP)	Critical peak pricing overlaid onto time-of-use pricing
Variable Peak Pricing (VPP)	Similar to time-of-use, but the peak period price varies daily based on system and/or market conditions rather than being fixed
Dynamic time-of-use (dToUP)	Prices vary between fixed price levels, but the timing of different prices is not fixed
Real-time-pricing (RTP), including DA-RTP (day ahead real time pricing) and RT-RTP (real time real time pricing)	Price can differ on a daily basis and change each hour of the day (or more frequently) based on system or market conditions. DA-RTP provides the 24 hour price schedule a day in advance; RT-RTP notifies the price in real time. If the response is automated, RTP can create short term responses for system balancing

directly when necessary.

In [42], a method for real time voltage regulation under emergencies and renewable fluctuations was proposed, which was realised by a combination control of tap changer condition and load curtailment. Through a two-step multi-objective optimisation, aggregated heat pumps (HPs) were managed as dispatchable grid-side resource with constraints for customer comfort to achieve control required to maintain voltage stability [43]. Besides, DSR programmes have also been demonstrated effective in congestion management on both transmission [44] and distribution levels [45].

Management of demand consumption includes direct on/off control, duty cycle control for thermostatic loads (e.g. fridges, air-conditioners etc.) and utilisation of the voltage dependence of loads. A distributed random controller was developed in [46] for thermostatic control of domestic refrigerators in response to sudden plant outages. Stochasticity helps in desynchronisation of each refrigerator while keeping overall power consumption under control. Using this Dynamic Demand (DD) concept, the value of enabling refrigerators' participation in primary frequency regulation was quantified [47]. However, DSR through thermostatic loads could be insufficient as they only account for a limited share of the total

load.

Another way to harness demand flexibility is to utilise the voltage dependence of loads for peak demand reduction by decreasing the operating voltage of the distribution feeders, well-known as the Conservation Voltage Reduction (CVR) [48]. Electricity North West Limited in Great Britain has conducted field trials to manage the load power consumption through transformer tap changer control at the substation with appropriate line drop compensation (LDC) [49]. CVR with LDC or to be more straightforward, voltage control at substations (VCS) can result in considerable energy savings without adverse effect on the consumers' side. The Smart Transformer [50] which can provide frequency response by shaping the load consumption accurately through an online load sensitivity identification-based control as well as frequency support in an isolated microgrid via a voltage-based frequency controller within the voltage regulator of generators [51] can both be classified as VCS.

However, during high loading conditions, the depth of allowable voltage reduction could be limited due to large voltage drop across the feeders so that the voltages at the far end can be maintained within the stipulated limits. Shunt reactive compensation would have limited effect on flattening the voltage profile in low-voltage (LV) feeders. Besides, parallel feeders with different loading (i.e. voltage drop) could seriously limit the overall capability of VCS.

This issue can be eased by PECs injecting a controllable series voltage between feeder segments (mid-feeder compensation, MFC) [8, 52] or even between feeder and each load connected (PVC). A comparison between CVR with LDC/VCS, MFC and PVC under high loading condition for demand reduction is shown in Fig. 1.1. For illustration purpose, uniform loading (which corresponds to each arrow), equal distance of separation between the loads and a linear voltage profile across the feeder are assumed. The substation voltage is assumed to be maintained at the maximum stipulated voltage (V_{\max}).

It is obvious that the extent of voltage reduction using VCS is limited compared to that of PVC, as denoted by the shaded area in Fig. 1.1. A detailed quantified comparison is given later in Chapter 2. Compared to VCS, MFC could also allow more flexibility but not as much as PVC in which case the voltage dependence of all the loads could be 'fully' exploited [53].

1.2.2 Point-of-load Voltage Control

PVC can be realised through PECs say the Electric Spring (ES) [6] connected in series between the feeder and the load with a limited rating. Based on the hardware topology and

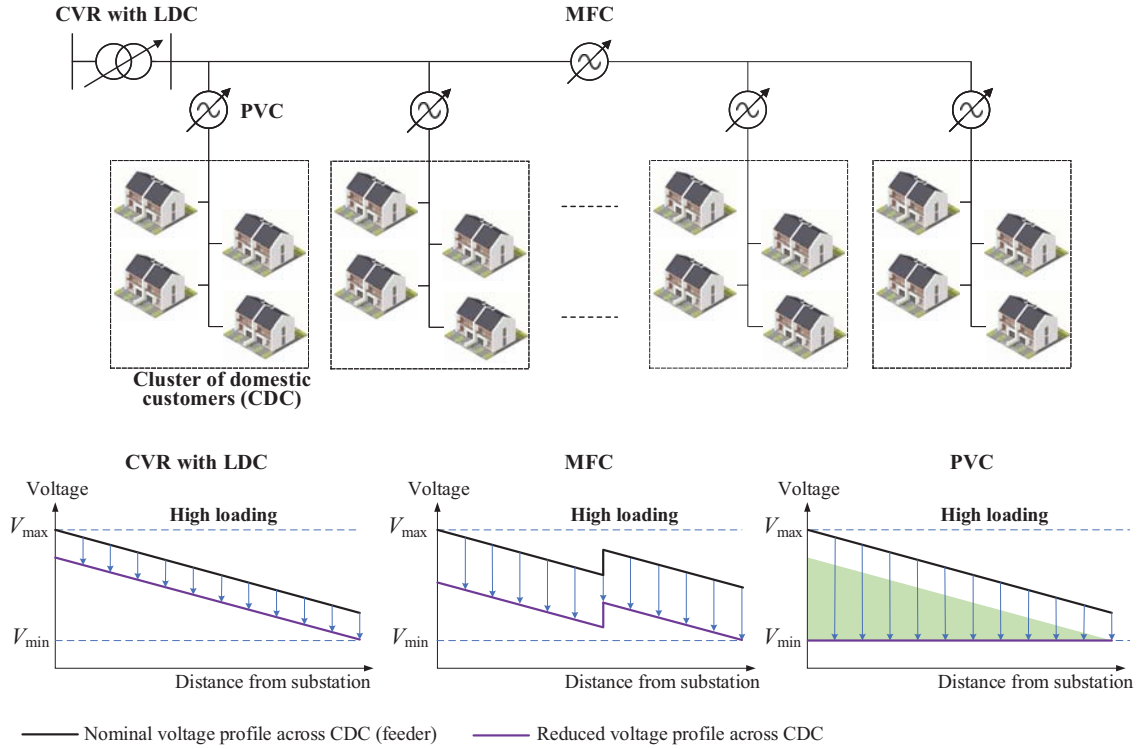


Fig. 1.1 Comparison between conservation voltage reduction (CVR) with line drop compensation (LDC), mid-feeder compensation (MFC) and point-of-load voltage control (PVC)

control objective, PVC through ESs can be categorised into 1) PVC with reactive power compensation only, referred to as PVC-Q; and 2) PVC with back to back configuration which can provide both active and reactive power compensation, referred to as PVC-B2B.

PVC-Q

The concept of ES was firstly proposed and demonstrated through a hardware prototype in [6]. Initially, non-critical loads, i.e. loads that can operate under certain degree of voltage variations, were equipped with ESs to support the voltage of critical loads, i.e. loads require well-regulated mains voltages, in the presence of intermittent renewables. As shown in Fig. 1.2 (a), the PEC is a single voltage source converter with a capacitor on the DC-side and is set to inject a voltage in quadrature with the load current, which means, it can provide reactive power compensation only. With reactive power provided by the ESs, the power consumption of the non-critical loads would also be altered as their voltages would be varied due to the injected voltages by ESs, which could compensate the active power fluctuations of renewable sources [18, 54]. Following the same philosophy, ESs could also contribute to

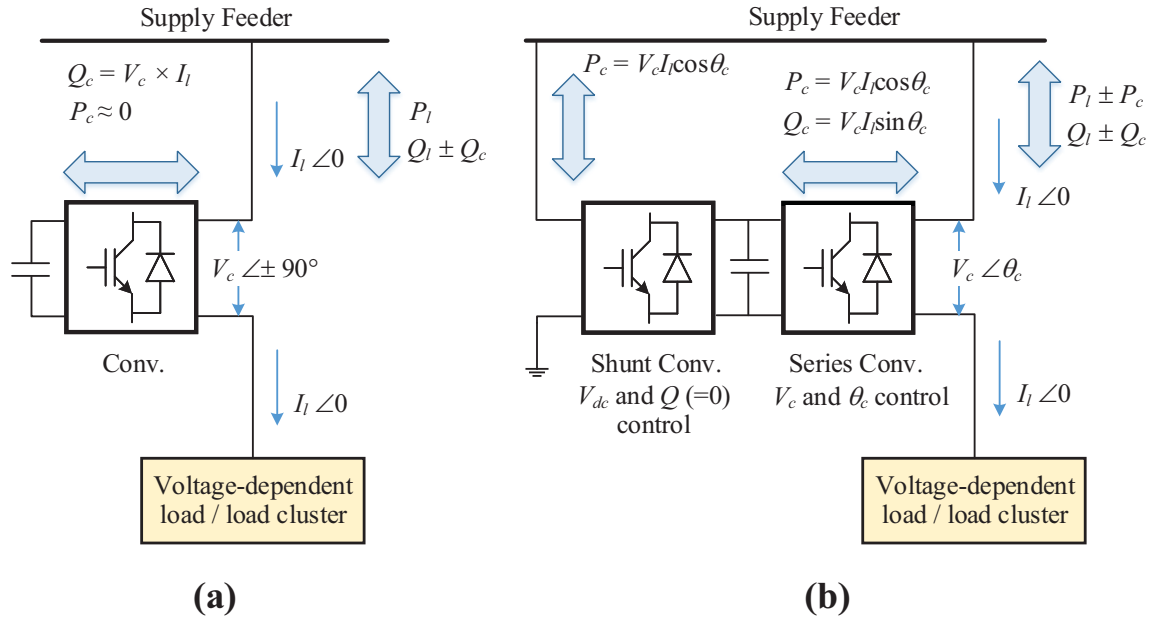


Fig. 1.2 (a) PVC with reactive power compensation only (PVC-Q) (b) PVC with back-to-back configuration (PVC-B2B)

reduction in energy storage required [22]. In [19], ESs are utilised to contribute to voltage or frequency regulation in a microgrid using droop control.

It was shown in [10] that multiple distributed controlled ESs could achieve better voltage regulation with relatively less power capacity, compared with the case of a single STATic COMPensator (STATCOM). A general comparative analysis of ESs and STATCOM can be also found in [17]. Similar to generator governor control, the operation of multiple ESs in a distribution network could also be coordinated through droop control scheme [55].

By regulating the input feeder-side voltage, the ES allows output load-side voltage to fluctuate dynamically. This type of ‘input-feedback and input-voltage control’ makes PVC-Q differing from existing approaches for PVC such as the dynamic voltage restorer (DVR) [56]. DVR also decouples the load from the feeder. However, DVR adopts an ‘output-feedback and output-voltage control’ strategy and is applied to critical customers with the intention for sub-cycle regulation of the customer’s voltage. The study presented in Chapter 5 is based on PVC with this type of configuration.

Theoretically, the injected voltage could be in any arbitrary angle with respect to the load current if the capacitor on the DC-side is replaced by a battery/energy storage. This enables

ESs to provide both active and reactive power compensation, as analysed and demonstrated by [16, 57]. The effectiveness of loads equipped with such ESs in mitigating voltage and frequency fluctuations in a microgrid was shown in [9]. [14] proposes ES aggregators which consist of a large number of ES-embedded loads in sub-transmission networks to provide transmission network level compensation.

Besides, the battery/energy storage on the DC-side allows the ESs to realise other functions such as phase imbalance mitigation [23], neutral current mitigation [26], harmonic suppression [25] and power factor correction [20, 21, 24]. It has been shown in [23] that the load currents can be redistributed through a three-phase ES. A genetic algorithm (GA) based controller was adopted to generate three optimal independent SPWM switching pulses. A novel δ control is proposed in [20] to achieve active/reactive power/power factor compensation while maintaining the feeder-side voltage regulated. In [24], it has been proved that with energy storage embedded ESs, the power quality can be improved through line current regulation.

PVC-B2B

Independent control of active and reactive power compensation can be also achieved with a back-to-back configuration, as shown in Fig. 1.2 (b) [58]. This series-parallel converter arrangement is similar to a Unified Power Quality Conditioner (UPQC) [59] to some extent. The series converter is set to control the magnitude (V_c) and angle (θ_c) of the injected voltage while the shunt converter maintains DC-link voltage (V_{dc}) and thereby, exchanges the active power processed by the series converter (P_c) with the supply feeder. As a result, the total active power consumed by the load together with this ES would be equal to the load consumption itself (P_l) neglecting the filter and converter losses. To reduce the total required apparent rating, the shunt converter can be operated at unity power factor.

This PVC-B2B topology is adopted for flexible demand in the rest chapters besides Chapter 5. Unlike the Power Perfector [60], a commercial equipment designed for energy savings and power quality improvement for the customers, demand reduction (DR) achieved from PVC-B2B is more utilised for DSR provision from the utility perspective.

In general, the PEC rating required to provide flexible demand could be double as the demand reduction from PVC using this back-to-back configuration. This is similar to the case when using battery storage to provide equivalent flexibility, in which case a DC-DC and DC-AC setup would be adopted. So it would generally be more cost-effective using PVC-B2B for

flexible demand as battery itself requires extra cost. However, it should be noted that the duration of this service from PVC could be limited as reducing the voltages for thermostatic controlled loads (say refrigerators, freezers etc.) would result in longer operation periods.

Although this newly developed technology seems promising in future power system with high penetration level of renewables, literature listed earlier in this section are mostly ‘proof of concept’ and only considered impedance-type load which is an ideal and over-simplified representation of the real world. References [11, 61, 62] tried to compare the capabilities of PVC with different hardware configuration in voltage and frequency regulation. However, system level analysis is yet to be reported and one important factor in capability evaluation, i.e. the power-voltage sensitivity was not taken into account. In [12], different types of loads were used without considering the time-varying incidence of various loads throughout a day. A methodology for estimating the hourly variation of available reserve with PVC was reported in [63] using load disaggregation at the bulk supply point but without considering the distribution network explicitly.

Chapter 2 fills in these gaps by using a high-resolution domestic demand and power-voltage dependence profile along with generic and benchmark network models to provide available reserve from PVC over a given time horizon (e.g. 24 hours) so that the network operators can schedule the conventional operating reserve accordingly. Chapter 3 further scales up the estimation to Great Britain national level and evaluates the benefits against the cost.

1.2.3 System Stability with Point-of-load Voltage Control for Voltage Regulation

Previously, stability problem at MV/LV level did not draw much attention due to its relatively simple configuration and the lack of the possibility to exert a side effect in a wide range. However, with an increasing penetration of PECs interfaced applications, unexpected stability issues can arise due to interaction among control loops of such PECs as well as with the power grid, just as the case of microgrids and transmission network. An example of stability analysis in collection grids of remote offshore DC connected wind farms at the medium voltage level (33 kV) shows that the parameters of the voltage source controller can have significant influence on medium frequency oscillation modes [64]. Hence, there is a concern that large penetration of PEC interfaced PVC, often in close electric proximity, could affect the small signal stability of the distribution networks.

Besides, the research focus for feeder-side voltage control has mainly been on various distributed control approaches (e.g. agent-based [65], consensus control [66] and more traditional volt-var techniques [67]) with less attention to stability analysis which motivates the work presented in this thesis.

A dynamic model of PVC-Q was developed in [68] to be incorporated in large-scale power system simulation studies. Based on the work done in [68], a linearised state space model was built up to investigate the impact of controller parameters on stability performance [69]. However, the frequency domain model was not based on vector control and hence not compatible with the standard stability model for other elements such as DG inverters etc. Besides, the effect of change in distribution network parameters on the overall stability was not reported in [69] either. To identify the root cause of the stability issue, modal analysis through a linearised state space model of a distribution network with vector controlled PVC-Q is presented in Chapter 5.

There are unique challenges in developing vector control of PVC-Q due to two important factors: 1) it has a series configuration and 2) only reactive power exchange is allowed. These two factors impose a quadrature constraint between the load current, filter capacitor current and the inverter current due to which it is not appropriate to align the d -axis with the point of coupling voltage (which is commonly done for shunt converters). This concern is addressed in Section 5.1.1.

1.2.4 System Stability with Point-of-load Voltage Control for Flexible Demand

It is well known that low frequency oscillations are inherent in isolated/islanded microgrids (IMGs) comprising of converter-interfaced distributed generators (CDGs) in grid-forming mode and passive [70–74] and active loads [75]. Unlike passive or active loads, PVC regulates the voltage and/or frequency at its point of connection typically using droop control. Thus, the low frequency oscillations in IMGs are expected to be affected with the presence of loads with PVC.

The benefits of ESs in IMGs have been demonstrated in [9, 76, 77]. However, in these papers, the synchronous (diesel) generators are mainly responsible for the voltage and frequency regulation in the IMG allowing the renewable energy resources to operate at their maximum power point. In Chapter 6, the loads with PVC-B2B are considered in an IMG with only

CDGs such as wind, solar PV and battery energy storage etc. Stability of such system has been investigated in [78] with voltage and frequency droop control on both CDGs and loads with PVC-B2B. However, the converters were simply represented as controllable voltage sources with first order lag, ignoring the dynamics of the control loops and the DC link. Such a simplified model of PVC-B2B cannot fully capture its impact on the low frequency dynamics of an IMG as demonstrated later in Chapter 6.

It is to be noted that the stability analysis in Chapter 5 & 6 utilises averaged models and does not consider unbalance situations. The harmonic frequency coupling between DC and AC side caused by switching behaviour in transient process is neglected as in such case, a different modelling approach say the harmonic state space (HSS) [79, 80] would be required.

1.3 Outline and Contributions

Following the introduction, distributed point-of-load voltage control (PVC) can be achieved through Electric Springs (ESs) and thereby present a new approach for demand side response (DSR). This thesis tries to further push this promising technology into practical application by answering the following questions:

- 1) In practical, how much demand reduction (DR)/operating reserve can be achieved from PVC for different time of the day and how is the techno-economic feasibility of this technology in future Great Britain (GB) power system?
- 2) How the overall small signal stability would be affected if multiple loads with PVC are implemented in a distribution network or an isolated microgrid (IMG) with converter-interfaced distributed generators (CDGs) in grid forming mode?

To address the above questions, the thesis is organised as below:

Chapter 2 quantifies the DR capability from PVC-B2B in domestic sector upon different time of the day using a high-resolution stochastic demand model and the aggregate power-voltage sensitivity of individual customers. This is compared against a conventional approach i.e. voltage control at substations (VCS). The rating of the voltage compensators required for PVC is evaluated to weigh the benefits against the required investment. First, the results are shown on a generic low-voltage network with random distribution of clusters of domestic customers at various buses and random length of feeder segments to draw general conclusions.

Then, the CIGRE benchmark medium- and low-voltage networks are used to substantiate the findings.

Chapter 3 investigates the techno-economic feasibility of PVC in future GB power system. The approach introduced in Chapter 2 is extended here to estimate DR provision from PVC-B2B in the urban domestic sector across GB. The DR is utilised to provide enhanced frequency response (EFR), which requires the response to be delivered within one second, for the value assessment. The economic and environmental benefits of using PVC are quantified in terms of savings in system operating cost, reduction in wind curtailment and CO₂ emission using a stochastic unit commitment (SUC) model with constraints for secure post-fault frequency evolution. Two future energy scenarios in the backdrop of 2030 with smart and non-smart control of electric vehicles (EVs) and heat pumps (HPs), under different levels of penetration of battery energy storage system (BESS) are considered to assess the value of PVC, as well as the associated payback period for the investment in deploying the power electronic compensators (PECs).

Chapter 4 utilises the fast DR provided from PVC-B2B to contribute to both primary frequency control and rate of change of frequency regulation. The equivalent virtual inertia and load damping effects from PVC are firstly derived. Then, the available virtual inertia from PVC for different time of the day in terms of inertia constants is presented based on the CIGRE benchmark microgrid. Finally, time domain simulation verifies and demonstrates the capability of PVC in frequency regulation.

Chapter 5 presents small signal stability analysis of distribution networks with PVC-Q. Vector control of a PVC-Q is reported to ensure compatibility with the standard stability models of other components such as the CDGs. A linearised state space model of the distribution network with multiple PVC-Qs is developed which is extendible to include CDGs, energy storage, active loads etc. The impact of distance of a PVC-Q from the substation, proximity between adjacent PVC-Qs and the R/X ratio of the network on the small signal stability of the system is analysed and compared against the case with equivalent DG inverters.

Chapter 6 investigates the low frequency (< 30 Hz) oscillations in IMGs with PVC-B2B alongside CDGs fuelled by renewable energy resources (e.g. wind, solar) with battery energy storage. In an IMG with normal loads (active or passive), such oscillations are typically associated with the droop control of the CDGs operating in grid forming mode. This chapter shows that loads with PVC-B2B have marginal influence on these low frequency oscillations

but introduce a new oscillatory mode at a slightly higher frequency (>20 Hz). First, the linearised state-space model of an IMG is extended to include the dynamics of a PVC-B2B. Impact of such loads on low frequency oscillations in IMGs is then demonstrated through modal analysis and time domain simulation.

Chapter 7 summarises the contributions of the thesis and presents an outline of future research opportunities.

1.4 List of Publications

The work presented in this thesis is based on the following publications:

- **J. Guo**, L. Badesa, F. Teng, B. Chaudhuri, S.Y.R. Hui, G. Strbac, "Value of Point-of-Load Voltage Control for Enhanced Frequency Response in Future GB Power System", *IEEE Transactions on Smart Grid*, 2020, in Early Access.
- **J. Guo**, T. Chen, B. Chaudhuri, S.Y.R. Hui, "Stability of Isolated Microgrids with Renewable Generation and Smart Loads", *IEEE Transactions on Sustainable Energy*, 2020, in Early Access.
- **J. Guo**, B. Chaudhuri, S.Y.R. Hui, "Flexible Demand through Point-of-load Voltage Control in Domestic Sector", *IEEE Transactions on Smart Grid*, vol. 10, no. 4, pp. 4662-4672, 2019.
- T. Chen, **J. Guo**, B. Chaudhuri, S.Y.R. Hui, "Virtual Inertia from Smart Loads", *IEEE Transactions on Smart Grid*, 2020, in Early Access.
- D. Chakravorty, **J. Guo**, B. Chaudhuri, S.Y.R. Hui, "Small Signal Stability Analysis of Distribution Networks with Electric Springs", *IEEE Transactions on Smart Grid*, vol. 10, no. 2, pp. 1543-1552, 2019.

Chapter 2

Flexible Demand from Point-of-load Voltage Control

As discussed in Section 1.2, flexibility in demand can be realised through voltage control at the points of connection of individual loads e.g. supply point of a cluster of domestic customers (CDC). Compared to voltage control at substations (VCS), this offers more flexibility for demand reduction (and increase, if required) through voltage especially, under high loading conditions as shown in Fig. 1.1.

For PVC, a CDC in close electric proximity (e.g. residential units in a building, houses along a street) could be decoupled from the low voltage (LV) feeder using a power electronic compensator (PEC). A CDC approach is adopted as a trade-off between exploiting the load diversity with not much sacrifice on granularity. The configuration and size (i.e. number of customers) of each CDC would vary depending on the connection arrangement in a particular feeder. However, the electric proximity should be such that the voltage drop within a CDC is negligible (e.g. less than 1%) compared to that along the LV feeder. As the PEC is connected in series between the feeder and a CDC, it can be rated at only a fraction (typically 5-10%) of the diversified peak demand (DPD) of the CDC. Also, the diversity in demand within each CDC limits the required rating of the PEC.

Previous work on quantification of voltage driven DR capability with VCS employed aggregate load models at the medium voltage (MV) level which includes the influence of medium- and low-voltage (MV/LV) network components [49]. These models are not suitable for analysis of DR with PVC as the power-voltage dependence of a CDC in a LV network is typically lower than that of the aggregated models [81].

In this chapter, a quantitative comparison between the DR capabilities of PVC against VCS for different time of the day is reported. Moreover, the rated capacity (and hence, the physical size and capital investment) of the voltage compensators to be deployed is evaluated to weigh the benefits against the cost. The scope of this chapter is limited to domestic sector only as the necessary high time-resolution demand models for industrial and commercial customers is not readily available.

2.1 Demand Reduction

The aggregate power-voltage dependence of the i^{th} CDC at a given time instant t can be expressed in exponential form [82] as:

$$P_{li}(t) = P_{li}^*(t) V_{li}(t)^{n_{pi}(t)}, \quad Q_{li}(t) = Q_{li}^*(t) V_{li}(t)^{n_{qi}(t)} \quad (2.1)$$

where, $P_{li}^*(t)/Q_{li}^*(t)$ is the nominal active/reactive power consumption at 1.0 p.u. voltage and $n_{pi}(t)/n_{qi}(t)$ is the aggregate active/reactive power-voltage sensitivity at time t .

As in (2.1), all the terms in the equations henceforth are time-varying unless otherwise specified. However, to avoid the equations overflowing due to lack of space, the time varying quantities such as $P_{li}^*(t), n_{pi}(t)$ would be simply denoted as P_{li}^*, n_{pi} .

In a radial distribution feeder, the voltage at i^{th} bus (CDC) could be expressed in terms of the adjacent bus voltage as (2.2) [83]. A detailed derivation is given in Appendix A.

$$V_{pi}^2 = \left[\left(P'_{li} R_i + Q'_{li} X_i - 0.5 V_{pi-1}^2 \right)^2 - \left(R_i^2 + X_i^2 \right) \left(P_{li}'^2 + Q_{li}'^2 \right) \right]^{\frac{1}{2}} - \left(P'_{li} R_i + Q'_{li} X_i - 0.5 V_{pi-1}^2 \right) \quad (2.2)$$

where

$$P'_{li} = P_i + \sum_{j=i+1}^{N_c} \left(P_j + P_{LLj} \right), \quad Q'_{li} = Q_i + \sum_{j=i+1}^{N_c} \left(Q_j + Q_{LLj} \right) \quad (2.3)$$

where, P'_{li}/Q'_{li} sum of the active/reactive power loads at bus i and beyond till the end of the feeder plus sum of the active/reactive power losses (P_{LLj}/Q_{LLj}) in all feeder segments beyond bus i . R_i/X_i is the resistance/reactance of the feeder segment between bus i and

$i - 1$ and N_c is the number of CDC. With a specified substation voltage V_{p0} the rest of the bus (i.e. CDC) voltages could be worked out for a particular loading condition.

The total active power demand reduction (DR_{PVC}) possible by reducing the voltage of all the CDC to the minimum stipulated limit V_{\min} is given by:

$$DR_{PVC} = \sum_{i=1}^{N_c} P_{li}^* \left[V_{pi}^{n_{pi}} - V_{\min}^{n_{pi}} \right] - \Delta P_{LL} - \sum_{i=1}^{N_c} P_{LCi} \quad (2.4)$$

where, N_c is the total number of CDC in the system, ΔP_{LL} represents the change in network power loss as a result of reducing each CDC's voltage to V_{\min} and P_{LCi} is the total losses (conduction and switching) incurred in the PEC at CDC i . Typically, network power loss would be less (i.e. ΔP_{LL} is negative) with reduced CDC voltage (and hence, power) except when all or most of the power-voltage sensitivities of CDCs are less than 1. The loss in the PEC would depend on the power processed by it (see Section 2.2) and its rated capacity. Everything except V_{\min} in (2.4) varies according to the time of the day. For the studies reported subsequently, V_{\min} is assumed to be 0.95 p.u. [84] to keep the reduced voltages within acceptable limits which is what the utilities are obliged to ensure. It is to be noted that critical (or sensitive) customers requiring tighter voltage tolerance would not be part of PVC. Such critical customers are generally present in the industrial/commercial sector which is not within the scope of the current study.

For DR through VCS, the total possible active power demand reduction (DR_{VCS}) is calculated by:

$$DR_{VCS} = \sum_{i=1}^{N_c} P_{li}^* \left[V_{pi}^{n_{pi}} - V_{pi}'^{n_{pi}} \right] - \Delta P_{LL} \quad (2.5)$$

where, $V_{pi}'^{n_{pi}}$ is the reduced feeder-side voltage after VCS, ΔP_{LL} is the change in network power loss as a result of reduced (to V_{pi}') supply voltage to each CDC.

The DR capabilities of PVC and VCS are compared in terms of an index, ΔDR defined in (2.6).

$$\Delta DR(\%) = \frac{DR_{VCS} - DR_{PVC}}{DR_{PVC}} \times 100\% \quad (2.6)$$

In order to obtain a closed form analytical expression for ΔDR , the following simplifying assumptions are made. Note that this is just to give an initial view of the issue and all these

simplified assumptions will be removed for a fuller analysis later in Section 2.3 and 2.4. Removing these assumptions would make the derivation of the analytical expression much more complicated without altering the general conclusions.

- A radial distribution network with N_c uniformly spaced constant current (CI) loads having unity power factor.
- Purely resistive feeder with a total resistance of R_T (p.u.).
- The total loading P_T at nominal voltage is uniformly distributed resulting in a current flow $I = P_T/N_c$ through each CI load.
- PEC losses neglected.

With the substation voltage held at V_s , the voltages of the first three loads are given as:

$$V_{p1} = V_s - N_c I \frac{R_T}{N_c} = V_s - \frac{P_T R_T}{N_c} \quad (2.7)$$

$$V_{p2} = V_{p1} - (N_c - 1) I \frac{R_T}{N_c} = V_s - \frac{P_T R_T}{N_c} \left(\frac{2N_c - 1}{N_c} \right) \quad (2.8)$$

$$V_{p3} = V_{p2} - (N_c - 2) I \frac{R_T}{N_c} = V_s - \frac{P_T R_T}{N_c} \left(\frac{3N_c - 3}{N_c} \right) \quad (2.9)$$

Following this trend, the voltage at i^{th} load can be expressed as (2.10).

$$V_{pi} = V_s - \frac{P_T R_T}{N_c^2} i [N_c - 0.5i + 0.5] \quad (2.10)$$

DR through PVC can then be expressed (2.11).

$$\begin{aligned} DR_{PVC} &= \sum_{i=1}^{N_c} \frac{P_T}{N_c} [V_{pi} - V_{\min}] \\ &= P_T (V_s - V_{\min}) - \frac{P_T^2 R_T}{6N_c^2} (2N_c + 1)(N_c + 1) \end{aligned} \quad (2.11)$$

It is to be noted that there would be no change in network power losses as all the loads are assumed to be constant current type.

For determining DR through VCS, the minimum possible voltage at the substation V'_s is obtained such that the voltage at the far end of the feeder is at the minimum limit. The

voltages at each node are then recalculated using (2.10) with V'_s . DR through VCS is given as (2.12).

$$\begin{aligned} DR_{VCS} &= \sum_{i=1}^{N_c} \frac{P_T}{N_c} [V_{pi} - V'_{pi}] \\ &= P_T(V_s - V_{\min}) - \frac{P_T^2 R_T}{2N_c}(N_c + 1) \end{aligned} \quad (2.12)$$

Without loss of generality, N_c is assumed to be 20, V_s maintained at the upper limit 1.05 p.u., and the lower limit V_{\min} to be 0.95 p.u. The total feeder resistance R_T is calculated considering violation of the low voltage limit (at the far end of the feeder) beyond a certain amount of overloading (say, 1.2 p.u. loading).

With the above-mentioned assumptions, the variation of ΔDR with respect to loading is shown in Fig. 2.1 (a). It should be noted that a negative value of ΔDR denotes DR capability of VCS is less than that of PVC according to (2.6). The advantage of PVC over VCS increases with the loading level. The losses incurred within the PEC have been included numerically as mentioned in Section 2.2. PVC provides less DR than VCS at very low loading as the power losses incurred in the PECs become dominant. The traces with $N_c = 5$ and 50 confirm that the impact of varying load density is limited.

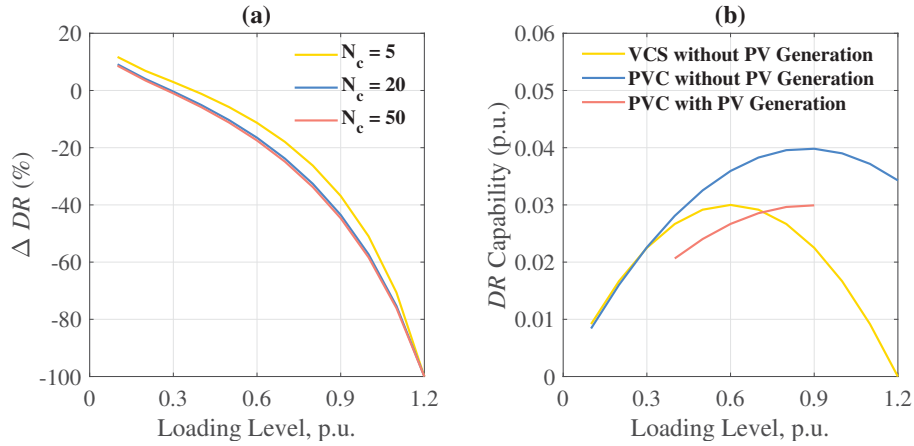


Fig. 2.1 Variation of ΔDR and DR capability with loading level

The absolute values of DR through VCS and PVC are shown in Fig. 2.1 (b). For a given load type, the DR capability depends of the demand (i.e. loading) itself and is expected to increase (decrease) at higher (lower) loading. However, at higher loading there is less room for voltage (i.e. demand) reduction due to larger voltage drop across the feeder. Due to these

opposing trends, the DR capability peaks at a certain loading which is lower for VCS than PVC. This is due to the fact that the room for voltage reduction using VCS becomes lesser than that using PVC with increase in loading level.

The DR capability using PVC under reverse power flow due to photovoltaic (PV) generation is shown in Fig. 2.1 (b). During reverse power flow, the substation voltage is generally maintained at the minimum limit (0.95 p.u.) to avoid over voltage problem at the far end. It is difficult to continuously adjust the substation voltage with varying PV output which leaves no room for DR through VCS.

With PV generation, the range of loading level is limited to 0.4-0.9 p.u. considering the typical variations (shown in Figs 2.6 & 2.13) during the daylight hours. The DR capability of PVC is lower in presence of PV generation across different loading levels. This is due to the fact that the substation voltage is generally set at the lower limit 0.95 p.u. to prevent over-voltage at the far end of the feeder which leaves less room for voltage (i.e. demand) reduction compared to the case without PV penetration.

Although the analysis presented above assumes purely resistive feeder and constant current loads only, it provides a theoretical basis for the ΔDR figures obtained later in Sections 2.3 & 2.4 using realistic network parameters and high-resolution domestic demand models.

2.2 Power Electronic Compensator

A PEC with back-to-back configuration [57], referred to as PVC-B2B in Section 1.2.2, is used to inject a controllable series voltage between the CDC and the LV feeder. The configuration is reshown in Fig. 2.2 (a).

For PVC, the magnitude of the injected voltage V_c can be controlled according to the demand reduction (or increase) requirement and the phase angle ϕ is set to be either in or out (to increase demand, if required) of phase with the feeder-side (V_p) or CDC (V_l) voltage (as shown in the phasor diagrams in Fig. 2.2 (b) and (c)) to exercise maximum change in CDC voltage with minimum apparent power rating. As a result, the PEC exchanges both active and reactive power.

For demand reduction, the injected voltage would be in phase with V_p resulting in the series converter absorbing active power and the shunt converter injecting this power back into the

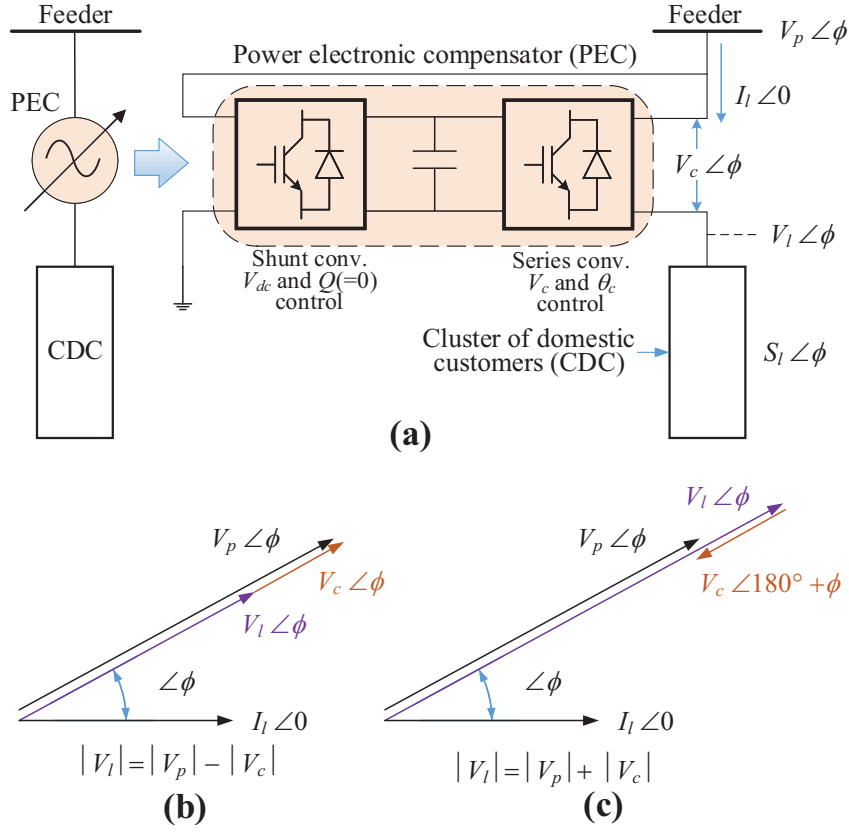


Fig. 2.2 Power electronic compensator (PEC) for point-of-load voltage control (PVC)

feeder. Neglecting the converter losses, the total demand reduction would be equal to the reduction in power consumption of the CDC [61]. Under normal condition, the PEC injects zero voltage ($V_c = 0$) which makes the feeder-side and CDC voltages the same ($V_p = V_l$) neglecting the small voltage drop across the series element of the converter interface filter (not shown explicitly in the figure).

The apparent power processed by the PEC at i^{th} CDC can be expressed as:

$$\begin{aligned}
 S_{ci} &= V_{ci} I_{li} (1 + pf_i') \\
 &= (V_{pi}' - V_{\min}) \sqrt{P_{li}^{*2} V_{\min}^{2(n_{pi}-1)} + Q_{li}^{*2} V_{\min}^{2(n_{qi}-1)}} (1 + pf_i')
 \end{aligned} \tag{2.13}$$

where, V_{pi}' , pf_i' are the modified feeder-side voltage (recalculated from power flow) and power factor, respectively as a result of reduction in voltage of the i^{th} CDC to V_{\min} . Apart from the series voltage (V_{ci}) inserted by the PEC and the CDC current I_{li} (which is the same as PEC current), the term $(1 + pf_i')$ accounts for the fact that the shunt converter operates at

unity power factor while balancing the active power exchanged by the series converter. For the following studies, the conduction loss is considered to be 3.75% of the power processed by the PEC while the switching loss is 0.25% of its rated capacity [85]. To avoid additional power loss, the PEC would be bypassed when DR is not exercised. Typically, V'_{pi} would be slightly larger than V_{pi} due to decreased feeder voltage drop following CDC voltage (and hence power) reduction unless power of all or most of the CDCs are less responsive to voltage variations.

For a given power consumption $S_{li} = \sqrt{P_{li}^2 + Q_{li}^2}$ by a CDC, the apparent power processed by the PEC (S_{ci}) is larger when the power-voltage exponents n_{pi}/n_{qi} are smaller. Fortunately, there is a correlation between the actual power consumption of a CDC and the values of the power-voltage exponents with both becoming low/high around similar time of the day (say during evening hours and late nights of summer). Hence, the power processed by the PEC is always limited. The rating of the PEC to be installed at each CDC would be dictated by the maximum possible S_{ci} over the 24-hour period and across different seasons (winter/summer) and days (weekdays/weekends).

The total demand reduction possible through PVC at a given time and the rated capacity of the PEC depends on the aggregate demand and power-voltage dependence of each CDC and the voltage across a CDC, all of which vary depending on the time of the day. The voltage also depends on the location of a particular CDC on the feeder. In the subsequent chapters, a high resolution domestic demand model is used to quantify the demand reduction with PVC and the PEC rating required. This is first done with a random distribution of CDC mimicking a generic LV feeder (Section 2.3) and then with the CIGRE benchmark MV/LV network (Section 2.4).

2.3 Generic Low Voltage Feeder

The DR capability of PVC depends on the feeder configuration and the loading profile. In this section, the DR of PVC is compared against that of VCS using a generic LV feeder with random separation between adjacent CDCs and random distribution of loads among the CDCs. A stochastic demand model for domestic customers in Great Britain is considered.

2.3.1 Domestic Demand Model

The 24-hour demand profile for each domestic customer is generated using a domestic demand model developed by the Centre for Renewable Energy Systems Technology (CREST) [86]. The model provides household level electricity consumption with one minute resolution by allocating the usage of 35 typical household appliances according to daily activity and active occupancy pattern for a given number of residents, day of the week and month of the year. It is to be mentioned that electric vehicles and heat pumps are not included here and embedded generation (e.g. roof-top photovoltaic) are not considered in this study. A set of 24-hour total demand profiles for each appliance (P_d) and individual domestic customers (P_h) are obtained by running the demand model repeatedly. Combining these demand profiles with the ZIP load model coefficients (Z_p , I_p , P_p) of the 35 appliances [87] (listed in Table 2.1 on the next page), the aggregate active power-voltage sensitivity (n_{ph}) for each domestic customer is calculated by (2.14). This can be obtained by using Taylor Expansion and neglecting high order terms given that operating voltages would be around 1.0 p.u.

$$n_{ph} \approx \frac{\sum_{i=1}^{35} P_{di}(2 \times Z_{pi} + 1 \times I_{pi} + 0 \times P_{pi})}{\sum_{i=1}^{35} P_{di}(Z_{pi} + I_{pi} + P_{pi})} \quad (2.14)$$

The incidence of appliances within a household over a typical winter and summer weekday is shown in Fig. 2.3. The thick blue trace is the total active power consumption of all appliances within the household. It can be seen that with storage heater, the maximum demand consumption can be up to about 12 kW during winter late night. Compared with Fig. 2.6, the aggregation effect of a CDC can be also observed.

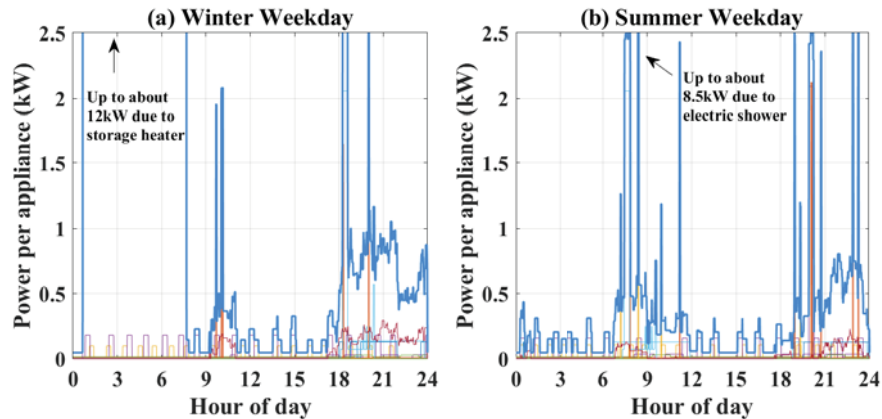


Fig. 2.3 Incidence of appliances within a household over a typical (a) winter weekday; (b) summer weekday

Table 2.1 ZIP Load Model Coefficients

Appliance Type	Zp	Ip	Pp	Zq	Iq	Pq	pf
Chest freezer	1.17	-1.83	1.66	7.07	-10.94	4.87	0.92
Fridge freezer	1.17	-1.83	1.66	7.07	-10.94	4.87	0.92
Refrigerator	1.17	-1.83	1.66	7.07	-10.94	4.87	0.92
Upright freezer	1.17	-1.83	1.66	7.07	-10.94	4.87	0.92
Answer machine	0	0	1	3.63	-9.88	7.25	-0.99
Cassette / CD Player	0	0	1	3.63	-9.88	7.25	-0.99
Clock	0	0	1	3.63	-9.88	7.25	-0.99
Cordless telephone	0	0	1	3.63	-9.88	7.25	-0.99
Hi-Fi	0	0	1	0.45	-1.44	1.99	0.97
Iron	1	0	0	0	0	1	1
Vacuum	1.18	-0.38	0.2	4.1	-5.87	2.77	0.97
Fax	0	0	1	3.63	-9.88	7.25	-0.99
Personal computer	0	0	1	0.45	-1.44	1.99	0.97
Printer	0	0	1	0	0	1	1
TV1	0	0	1	0.45	-1.44	1.99	0.997
TV2	0.16	-0.15	0.99	0.45	-1.44	1.99	0.97
TV3	0	0	1	0	0	1	0.997
VCR / DCD	0	0	1	3.63	-9.88	7.25	-0.99
TV Receiver box	0	0	1	3.63	-9.88	7.25	-0.99
Hob	1	0	0	0	0	1	1
Oven	1	0	0	0	0	1	1
Microwave	1.39	-1.96	1.57	50.07	-93.55	44.48	0.95
Kettle	1	0	0	0	0	1	1
Small cooking (group)	1	0	0	0	0	1	1
Dish washer	1	0	0	0	0	0	1
Tumble dryer	0.96	0.05	-0.01	0	0	1	1
Washing machine	0.1	0.1	0.8	1.54	-1.43	0.89	0.995
Washer dryer	0.1	0.1	0.8	1.54	-1.43	0.89	-0.91
DESWH	1	0	0	0	0	1	1
E-INST	1	0	0	0	0	1	1
Electric shower	1	0	0	0	0	1	1
Storage heaters	1	0	0	0	0	1	1
Other electric space heating	1	0	0	0	0	1	1
Lighting GIS	0.47	0.63	-0.1	1.48	-1.29	0.81	0.995
Lighting CFL	-0.01	0.96	0.05	-0.1	0.73	0.37	-0.91

Then the aggregate active power-voltage sensitivity at the i^{th} CDC, which is used to determine the DR capability, is obtained by (2.15) in which N_h is the number of domestic customers within a CDC.

$$n_{pi} \approx \frac{\sum_{k=1}^{N_h} P_{hk} \times n_{phk}}{\sum_{k=1}^{N_h} P_{hk}} \quad (2.15)$$

To validate the approximation of power voltage sensitivities aggregation, a numerical comparison of the power consumption of 50 customers at V_{\min} is given in Fig. 2.4. The blue trace represents the actual power consumption calculated by the summation of each appliance while the red trace is the approximation using (2.14) and (2.15). The marginal difference between the two traces confirms the effectiveness of the approximation.

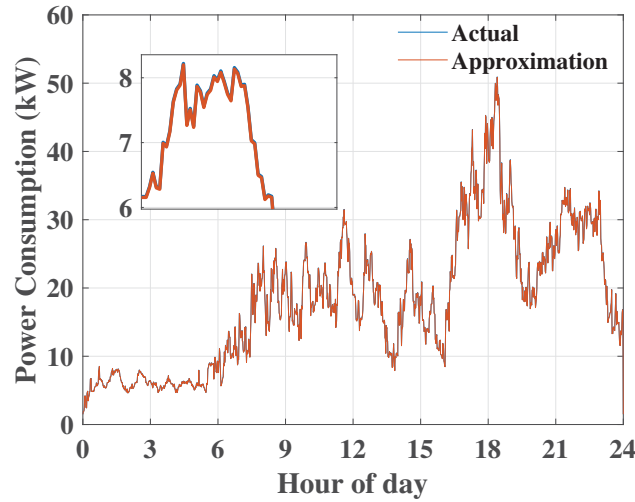


Fig. 2.4 Numerical comparison of the power consumption of 50 customers at V_{\min}

2.3.2 Demand Reduction Capability

To compare the DR capability of PVC and VCS, a generic radial LV feeder with random distribution of loads among CDC and random length of feeder sections is considered to obtain a general range of possible ΔDR under various network configurations. A fixed length (Z_f) and typical line parameters [88] of the LV feeder are considered while the number of CDC is varied between 5 and 20 [88]. The loading of each CDC and the length of each feeder segment (between adjacent CDCs) are varied randomly between $\pm 50\%$ of their values corresponding to an uniform distribution. The total DPD of the feeder is also varied between $\pm 50\%$ of the nominal value. These are summarised in Table 2.2.

Table 2.2 Parameter Range for Demand Reduction Calculation

Parameter	Range
Total diversified peak demand (P_T)	0.5 - 1.5 p.u.
Number of CDC (N_c)	5 - 20
Loading of each CDC	$0.5P_T/N_c - 1.5P_T/N_c$
Length of feeder segments	$0.5Z_f/N_c, 1.5Z_f/N_c$

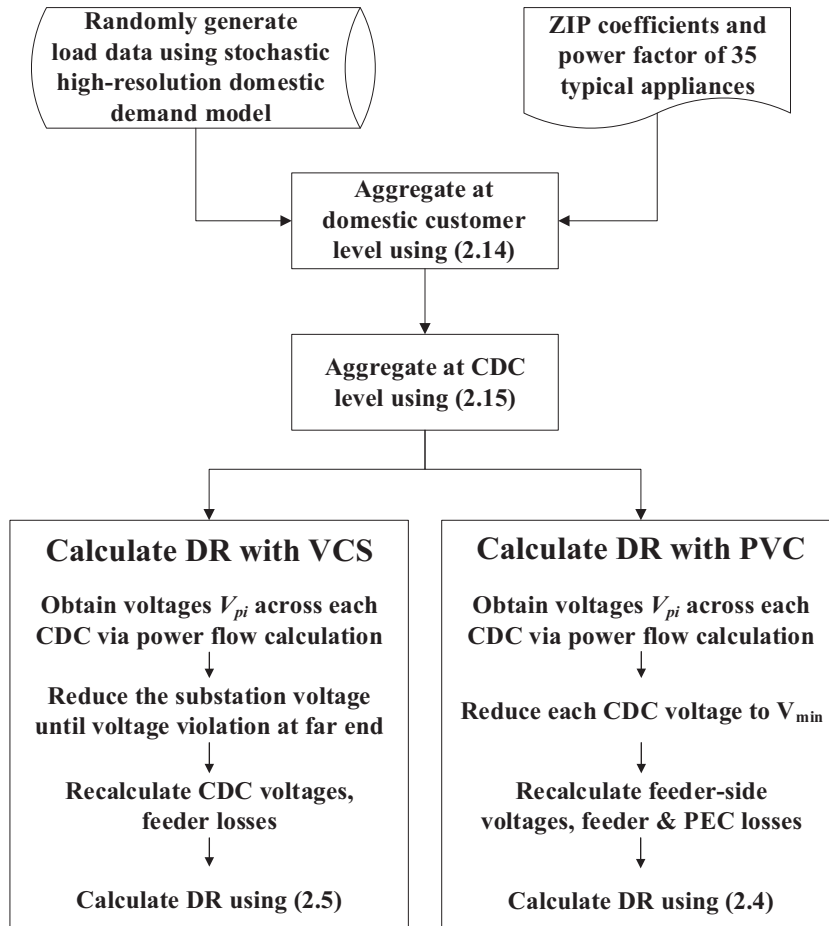
Loop 1: Set the total diversified peak demand (DPD)**Loop 2: Set the number of cluster of domestic customers (CDC)****Loop 3: Random distribution CDC loading and feeder segment length**

Fig. 2.5 Calculation of demand reduction capability

The DR capability is calculated by looping through the variation in the above parameters as shown in Fig. 2.5. Starting from the outer loop, Loop 1, 2 and 3 varies the total DPD of the entire feeder, the number of CDC and distribution of loading between them, respectively. This encompasses a wide range of LV feeder configurations including a dense urban or a sparse rural network. The upstream MV network is represented by its Thevenin equivalent.

The results shown in Figs. 2.6 to 2.9 correspond to typical winter and summer weekdays. A fixed total DPD (1.0 p.u.) and number of CDCs are considered to filter out the trends. Each figure consists of three traces representing the upper boundary (UB, 95 percentile), median value (50 percentile) and lower boundary (LB, 5 percentile) of the results considering the variations.

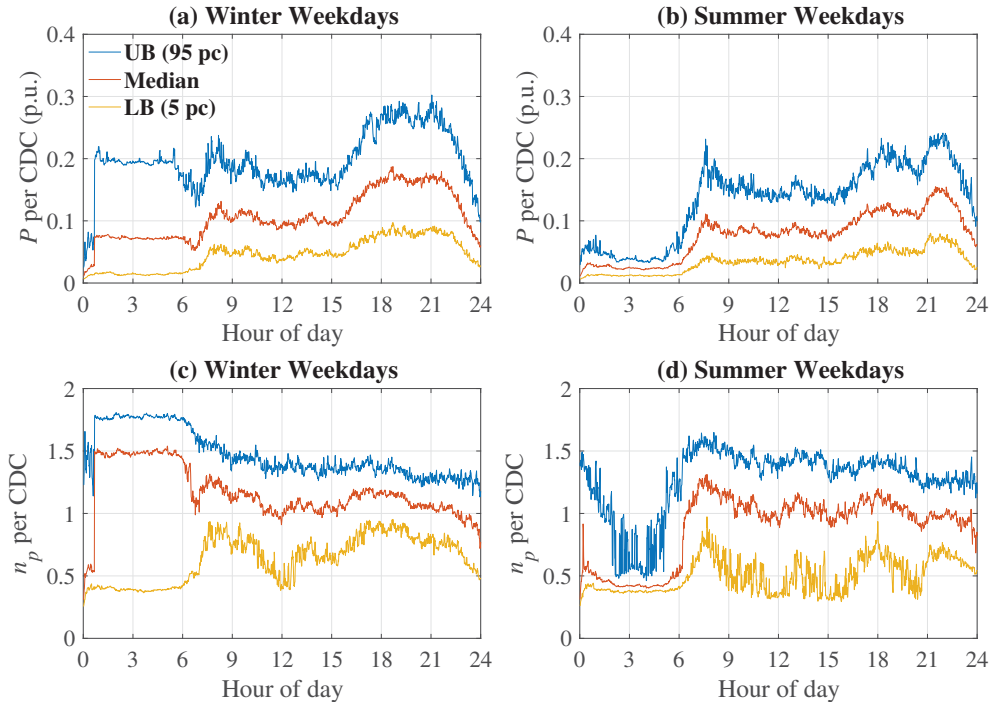


Fig. 2.6 Aggregate active power consumption and active power-voltage exponent at CDCs for winter and summer weekdays

Fig. 2.6 shows the 24-hour variation of active power consumption (P_l) and active power-voltage exponent (n_p) aggregated at the CDC level. The three traces show the variability in P_l , n_p between different CDCs. The UB of P is nearly 3 times the LB which corresponds to the range set in Table 2.2. The DPD across the day is larger for winter weekdays than summer with a prominent effect of electric heating (higher P_l and n_p) during the winter nights. According to a survey conducted by UK Department for Business, Energy and

Industrial Strategy [89], 8% of the domestic customers use electric heating including 3% storage, 4% non-storage and 1% portable heaters. Similar percentages are reflected if the CREST model is run sufficiently large number of times.

The time variation of voltage across the CDCs, shown in Fig. 2.7, is consistent with the loading of CDC in Fig. 2.6. The three traces in CDC voltage profiles represent the variability due to different electric proximity to the substation. The MV/LV transformer secondary tap position is maintained at 1.05 p.u. to avoid under-voltage at the far end of the feeder.

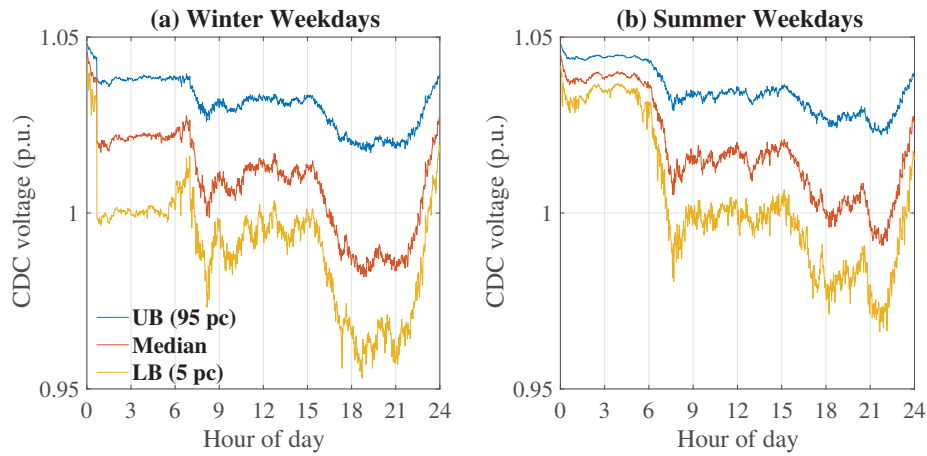


Fig. 2.7 Voltage across CDCs for winter and summer weekdays

Fig. 2.8 shows the DR capability of PVC and ΔDR for typical winter and summer weekdays. As mentioned before, a negative value of ΔDR denotes DR capability of VCS is less than that of PVC according to (2.6). During the winter weekdays, DR capability of PVC varies between 2% to 7% of the DPD across the 24-hour period. The DR capability of VCS is 40% to 55% less during most part (around 22:00-17:00 hours) of the day. During peak demand hours (around 17:00 - 22:00), the DR capability of VCS is much less with ΔDR touching -100% in some cases. This denotes that VCS totally loses its DR capability as the voltage at the far end of the feeder is below the lowest stipulated limit. Without electric heating, the DR capability of PVC would be less during the winter nights but the comparison against VCS (ΔDR) would still be similar.

For summer weekdays, the maximum capability of PVC is around 6% while the minimum can be as low as around 0.5% due to the very light loading during the late night and early hours of the day. The capability of VCS for other time of the day is still around 40% to 55%

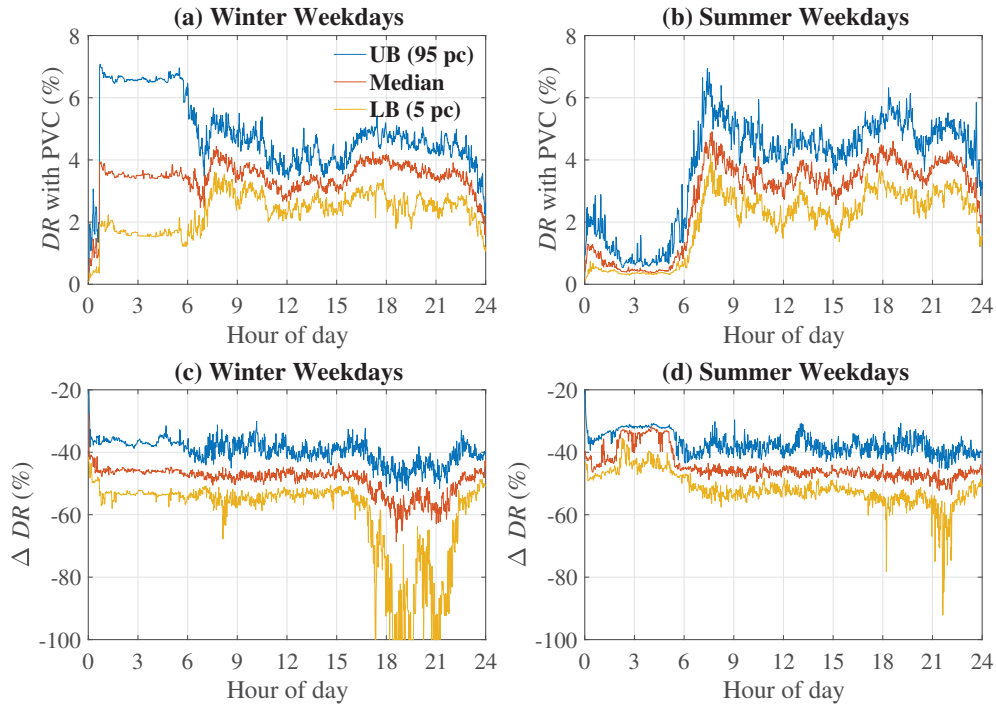


Fig. 2.8 Demand reduction (DR) capability of PVC and comparison with that of VCS (ΔDR) for winter and summer weekdays

less except some instances during the late evening peak where DR with VCS could be up to about 80% less.

2.3.3 Power Electronic Compensator Power

Improved DR capability of PVC comes at the expense of requirement of PECs at each CDC. Fig. 2.9 shows the variations in the total apparent power processed by the PECs to achieve the DR shown in Fig. 2.6. This is expressed as a percentage of the diversified peak apparent power demand of the feeder. Overall, about 2-12% of the power is processed by the PECs although the power through a particular PEC would depend on the loading level and active power-voltage exponent. It is interesting to note that during winter night hours, PVC offers higher DR capability with less power through PEC. This is due to relatively less loading (i.e. higher CDC voltages) and higher power-voltage exponent as discussed earlier in Section 2.2. The data points close to the upper bound (UB) trace correspond to the CDCs located close to the MV/LV transformer while those near the lower bound (LB) trace are CDCs at the far end of the feeder. The rating of each PEC is decided based on their individual maximum power processed over a range of winter and summer days as clarified further in Section 2.4.

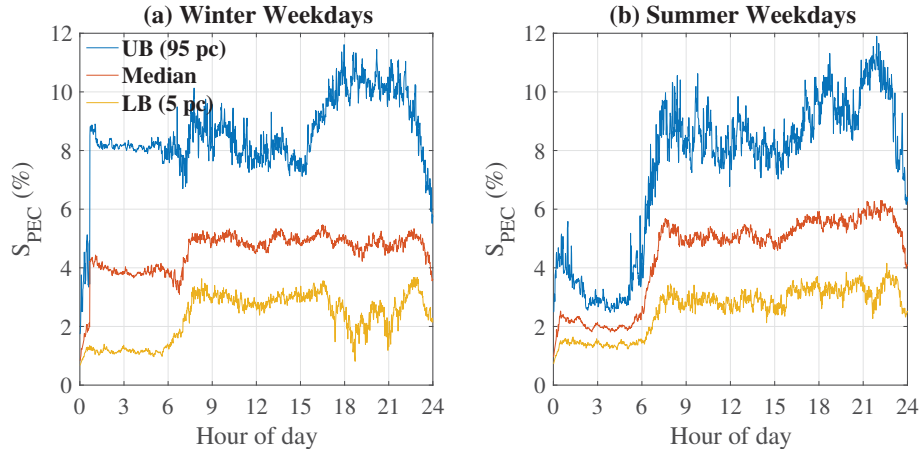


Fig. 2.9 Total apparent power processed by the power electronic compensators (PECs) for winter and summer weekdays

2.3.4 Sensitivity Analysis

The impact of varying loading and different number of CDCs connected to the feeder is considered here.

Loading Condition

The total DPD of the feeder is varied between $\pm 50\%$ of the nominal value to capture the impact of loading on DR capability of PVC.

Fig. 2.10 shows the results for peak (17:00-22:00) and off-peak (22:00-17:00) demand hours for winter weekdays. Although the DR capability of PVC reduces with higher loading, its effectiveness over VCS (ΔDR) actually increases. In fact, VCS would totally lose its DR capability for most part of the peak hours when the loading is high.

The sum of the maximum power processed by individual PECs connected at various CDCs are shown in Fig. 2.10 for peak and off-peak demand hours separately. The PEC power is less for higher loading due to the reasons mentioned above.

Number of CDC

The number of CDCs served by the LV feeder is varied between 5 to 20 keeping the total DPD fixed at 1.0 p.u. For a fixed loading, the voltage drop across the feeder is expected to be less for higher number of CDCs resulting in reduced difference between the DR capability of PVC and VCS. This trend could be observed in Fig. 2.11. For 15 or 20 CDCs, in some

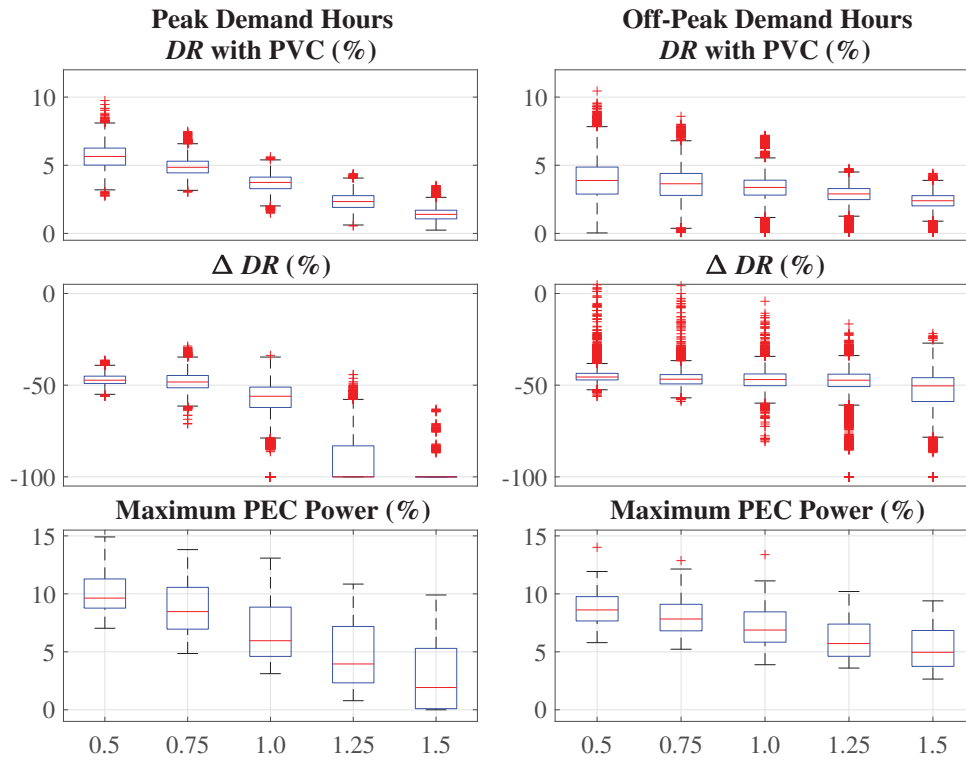


Fig. 2.10 Impact of loading level on demand reduction (DR) capability and PEC rating required

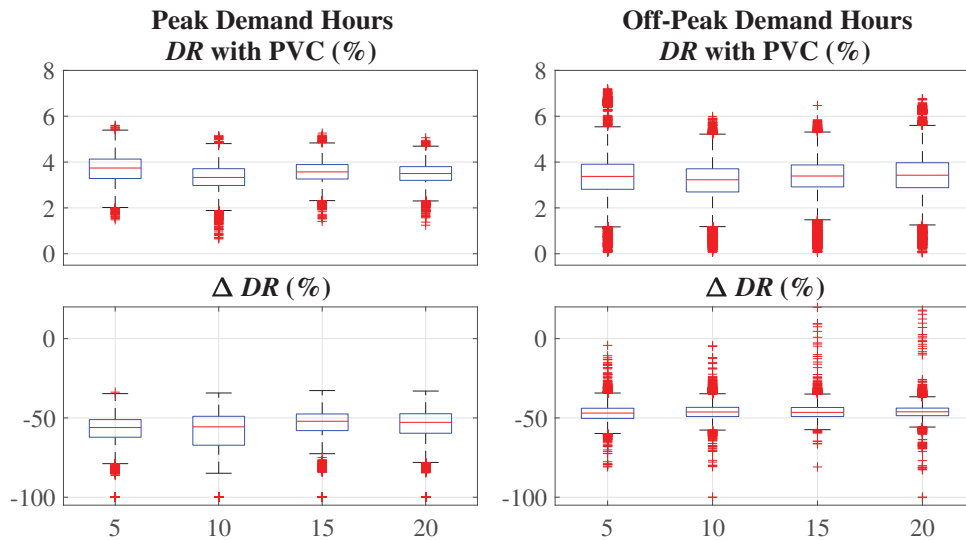


Fig. 2.11 Impact of number of CDCs on demand reduction (DR) capability

instances (as shown by the outliers) VCS offers similar (or even higher) DR capability as PVC during the off-peak demand hours. However, the impact of varying the number of

CDCs numbers is not as significant as changing the loading level which is consistent with the analysis provided in Section 2.1.

2.4 CIGRE Benchmark MV/LV Network

2.4.1 Network Description

The CIGRE European benchmark medium- and low-voltage (MV/LV) network [90] shown in Fig. 2.12 is considered in this section to further validate the general range of ΔDR achieved from the generic LV feeder in Section 2.3. The aggregated load at each MV bus is split into commercial/industrial loads and multiple parallel CIGRE benchmark LV feeders each containing 5 cluster of domestic customers (CDCs). The number of domestic customers connected at R11, R15-R18 are 14, 47, 50, 32, 42, respectively based on the DPD in [90]. The total DPD is 5.5 MVA with 70% domestic loads connected to the LV feeders and 30% commercial/industrial loads at the MV level [90]. As a high-resolution demand model (such as in [86]) for commercial and industrial customers is not readily available, the power-voltage dependence of only the domestic customers is considered for this study to ensure a fair comparison between PVC and VCS.

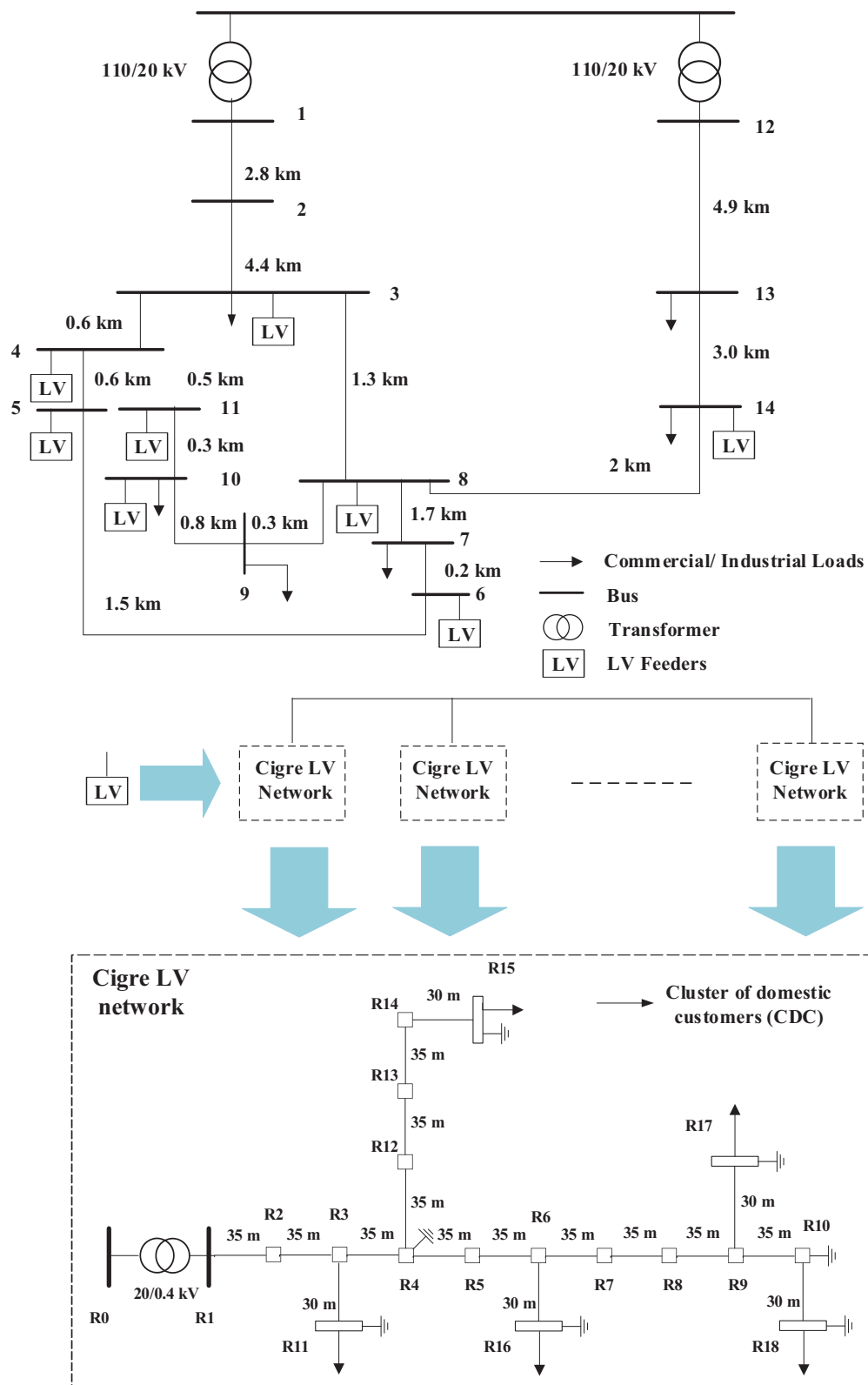


Fig. 2.12 CIGRE LV/MV benchmark network

The aggregated active power consumption (P) and the corresponding active power-voltage exponent (n_p) of the CDCs for winter and summer weekdays are shown in Fig. 2.13. As in Section 2.3, these are obtained from the high-resolution domestic demand model [86]. The traces denote the upper boundary (UB, 95 percentile), median value (50 percentile) and lower boundary (LB, 5 percentile) of the results.

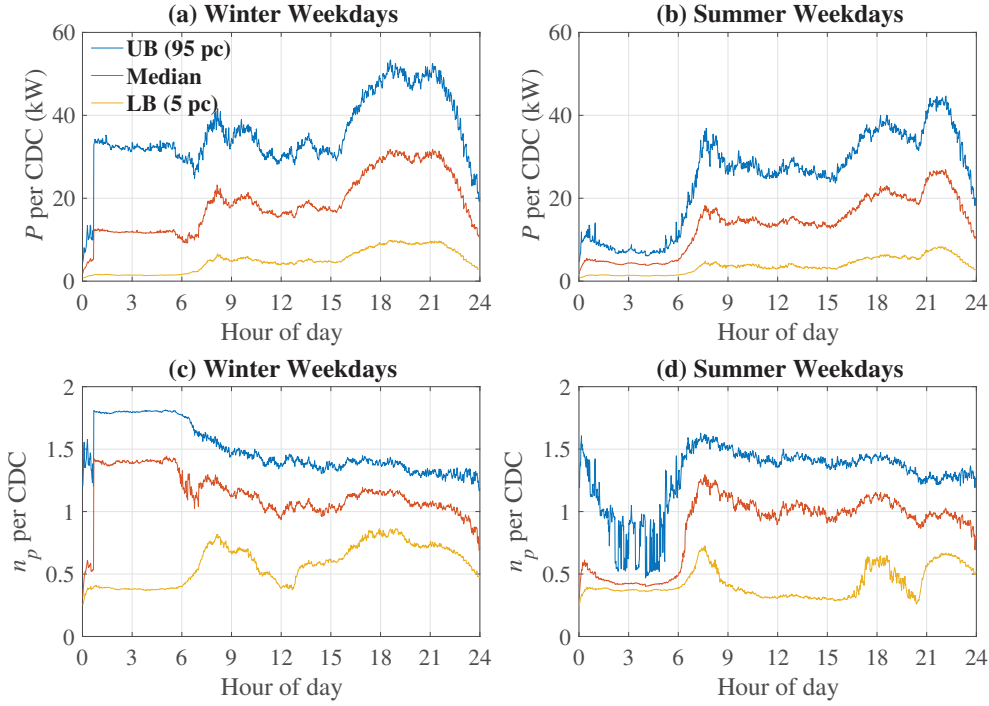


Fig. 2.13 Aggregate active power consumption and active power-voltage exponent at CDCs for winter and summer weekdays

The voltages across CDCs, shown in Fig. 2.14, are relatively low compared to the case study with a generic LV feeder in Section 2.3. This is evident during 1) winter peak hours (17:00 - 22:00) (in some cases below 0.95 p.u.) due to a higher loading condition and 2) daytime (around 8:00 - 15:00) due to the presence of commercial/industrial loads at the MV level.

2.4.2 Demand Reduction Capability

The DR capability of PVC and VCS are compared in Fig. 2.15. PVC can provide a DR of 100 kW to 180 kW (out of about 4.5 MW, DPD of the domestic sector) depending on the time of the day for both winter and summer weekdays. Variation of DR capability throughout a day is similar to that in Section 2.3 but with a smaller difference between UB and LB due to a fixed network configuration here unlike the generic LV feeder in Section 2.3. In practice, the system operators could rely on the LB of the DR capability

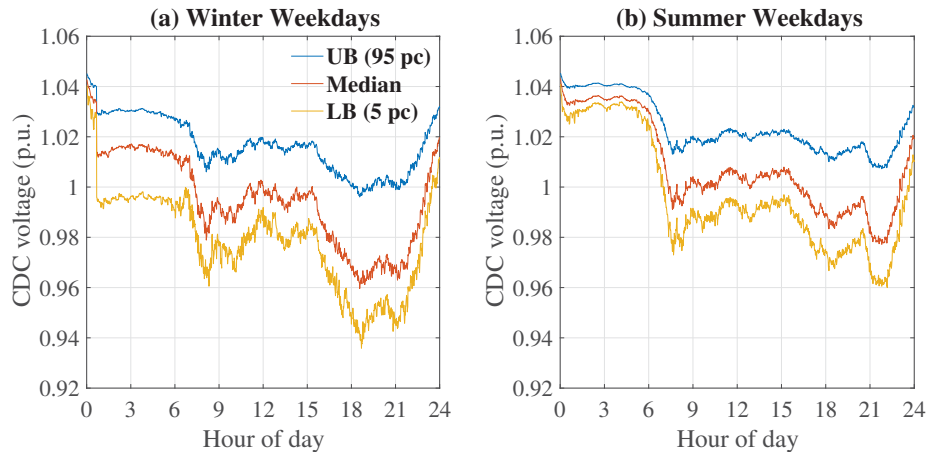
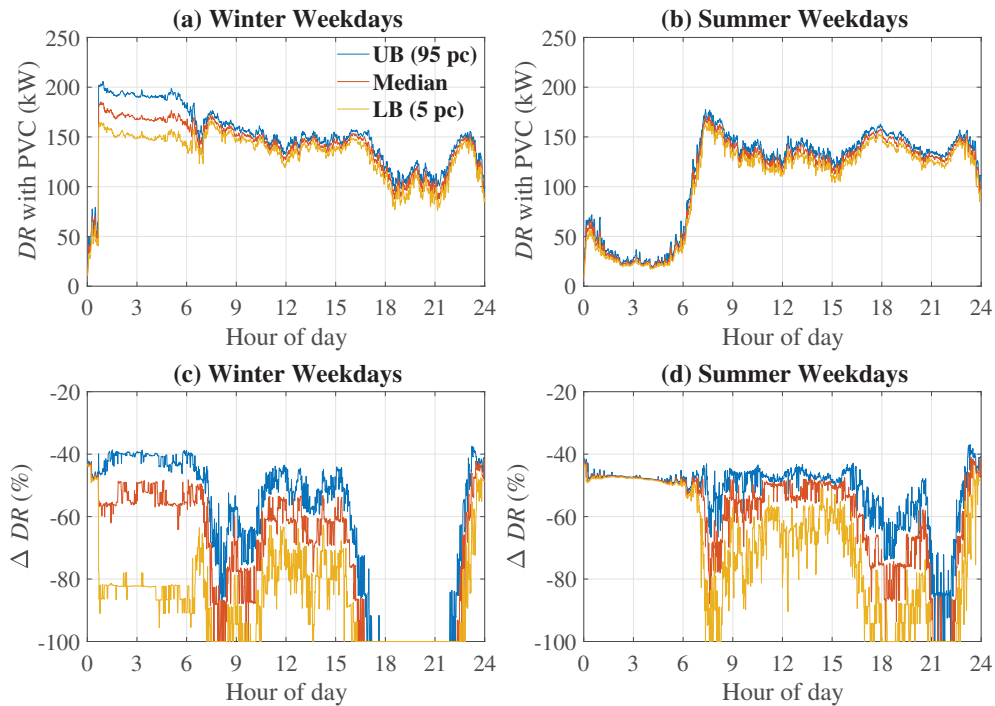


Fig. 2.14 Voltage across CDCs for winter and summer weekdays

Fig. 2.15 Demand reduction (DR) capability of PVC and comparison with that of VCS (ΔDR) for winter and summer weekdays

as this amount of DR is ‘very likely’ to be available even after considering all the variabilities.

The DR capability of VCS is significantly less (lower negative values of ΔDR) for the CIGRE benchmark MV/LV network compared to the generic LV feeder which is mainly due to relatively low CDC voltage as a result of higher loading. During the peak demand hours, VCS cannot produce any DR as the voltage at the far end of certain LV feeder(s) violates

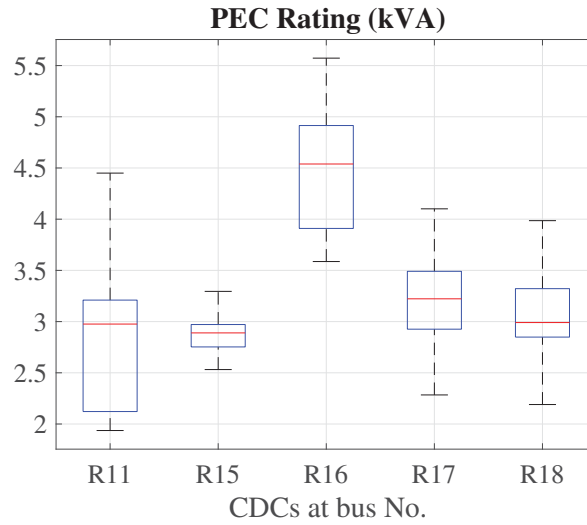


Fig. 2.16 Rating of power electronic compensators (PECs) at different buses across all the LV feeders with 155 clusters of domestic customers (CDCs)

the stipulated lower limit. During other times of the day, the DR capability of VCS is also limited due to large voltage drops caused by the commercial/industrial loads. For instance, when the commercial/industrial loads peak between 8-9 am [90], the DR capability of VCS is virtually zero. The LV feeders are connected to the MV network (bus 3-6, 8, 10-11 and 14) at different electrical distances from the primary (110/20 kV) substation. This leads to a much wider range of ΔDR as compared to the previous section where a fixed equivalent impedance was used to represent the MV network.

2.4.3 Power Electronic Compensator Rating

The rated capacity of the PEC required at each CDC is determined by the maximum power processed. These are shown in Fig. 2.16 separately for each bus (R11, R15-R18) considering all the 31 LV feeders with a total of 155 CDCs. The CDCs at R16 of all the LV feeders require a larger PEC rating due to high DPD and relatively small electrical distance from the MV/LV transformer. The rating of the PECs at different CDCs vary between 2-5 kVA which is less than 10% of the DPD of the respective CDC.

The total rated capacity of the PECs required for the CIGRE MV/LV network is around 500 kVA. Considering a conservative figure of \$150/kVA [91] for a typical low voltage single phase converter, the investment in deploying the PECs would be around \$75K. This could be recovered by utilising the DR capability of PVC to reduce the conventional operating reserve (OR) requirement and thus, decrease the OR availability (or holding) fees and OR utilisation

fees paid to conventional OR providers. The saving in OR utilisation fees depends on the actual balancing requirements of the system which varies with the proportion of intermittent renewable generation, available storage capacity etc. Summing up the hourly average of lower bound of DR capability of PVC (shown in Fig. 2.15 (b) and (c)) for various days (summer, winter, weekdays, weekends), the total yearly DR capability turns out to be 1030 MWh. Considering an OR holding fee of £6/MW/h [92] (although this varies depending on market condition) the payback period for the investment in PECs would be around 8-9 years using the current exchange rate of £1=\$1.4. Note that this is based on the saving in OR holding fee only. A more realistic estimation of the payback period is given in Chapter 3 in which the economic benefits come from the savings in system operation cost as the DR from PVC can be utilised to provide enhanced frequency response which reduces or eliminates the need for such a service from other sources such as battery energy storage.

2.5 Conclusion

Recent trials in Great Britain have shown that up to about 3 GW of system wide demand reduction (DR) is possible through voltage control at (primary) substation (VCS) alone [49]. This chapter confirms that such a large DR using VCS might not be possible under high loading. The DR capability of VCS is found to be 40-60% lower than that of point-of-load voltage control (PVC) for most part of the day and even less (up to 100% less) during the peak demand hours. Higher DR with PVC is achieved with power electronic compensators (PEC) rated at only about 10% of the diversified peak demand resulting in a reasonable payback time on investment. A high resolution domestic demand model, a generic LV feeder and a CIGRE benchmark network are considered to generalise and substantiate the above findings. In Chapter 3, the approach proposed in this chapter is extended and applied to estimate the DR provision from PVC in urban domestic sector across the Great Britain.

In future, loading of distribution networks would increase drastically during certain times of the day due to rise in distributed generation (e.g. roof-top solar) and electrification of heat and transport. During these periods, DR capability of VCS would be seriously limited (even becoming zero) necessitating PVC as demonstrated in this chapter. Use of PVC would reduce the need for operating reserve from various sources (e.g. energy storage etc.) and thereby, facilitate large-scale integration of intermittent renewable energy sources such as wind and solar power.

Chapter 3

Value of Point-of-load Voltage Control in Great Britain Power System

A significant amount of demand reduction (DR) can be achieved from point-of-load voltage control (PVC) as presented in Chapter 2. This chapter aims to further substantiate the benefits of PVC by looking ahead at the Great Britain (GB) power system in 2030: 1) extending the approach presented in Chapter 2 to estimate DR provision from PVC in the urban domestic sector of the Great Britain; and 2) quantifying the economic value in terms of reduced system operation cost and the payback period for the upfront investment in deploying PVC. A stochastic unit commitment (SUC) model with constraints for secure post-fault frequency evolution [93] is used for the above analysis.

Enhanced Frequency Response (EFR) was introduced by National Grid GB in 2017 [94] which is predominantly aimed at energy storage assets to provide frequency response within 1 second. PVC with PECs allows much shorter response time, making it an ideal option for providing EFR. Thereby, the value of PVC is evaluated through providing EFR service in this chapter. The effectiveness of increasing the demand for higher EFR provision or reducing it for energy saving when less (or zero) EFR is required to complement the role of battery energy storage system (BESS) is also demonstrated. The SUC model was developed by my colleague Mr Luis Badesa as part of a collaboration.

3.1.1 Approach

An outline for estimating the EFR provided by PVC in the urban domestic sector in the future GB system is given in Fig. 3.1. The estimation is mainly based on three items: 1) the overall demand profiles, including the base demand along with electric vehicle (EV) and heat pump (HP) profiles, obtained from the Future Energy Scenarios published by National Grid [95]; 2) high-resolution domestic demand models [86]; and 3) generic MV and LV networks for the GB developed by Centre for Sustainable Electricity and Distributed Generation [96] and CIGRE [88], respectively. It should be noted that no embedded generation is considered in the scenarios for simplicity. A detailed description of the process is as follows:

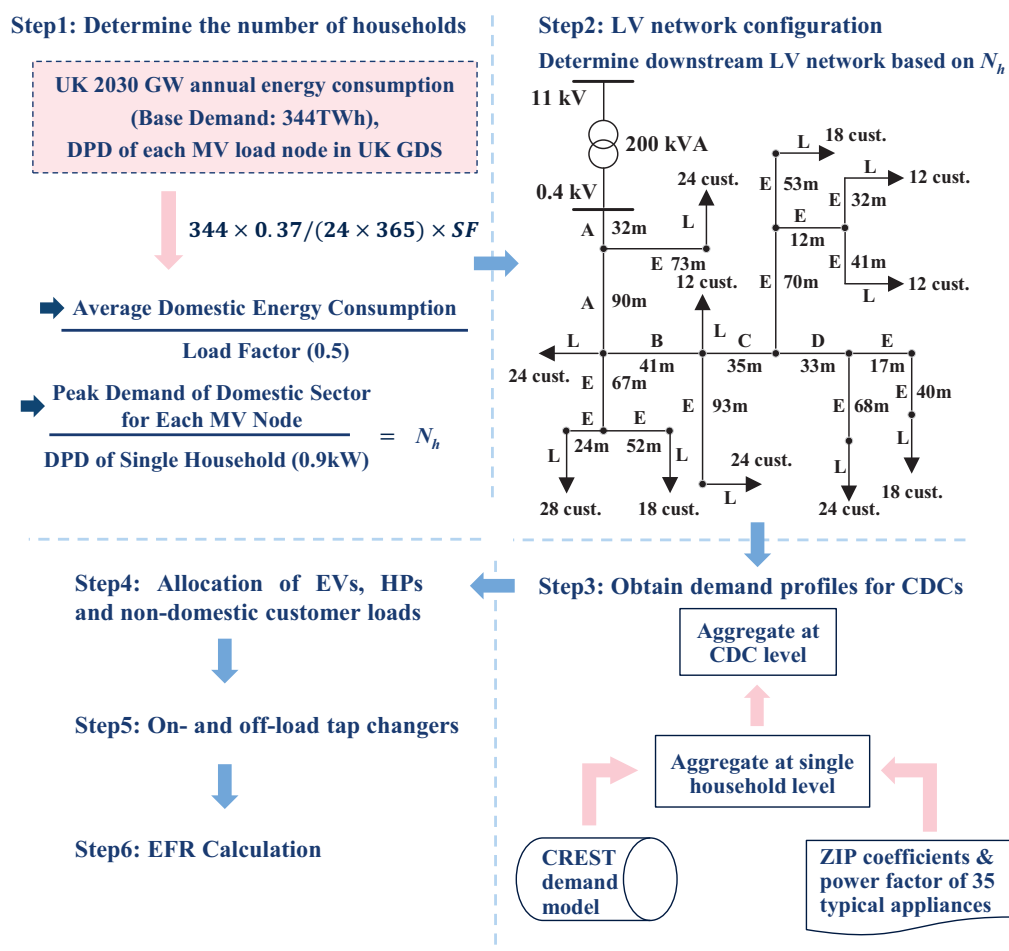


Fig. 3.1 An outline for estimating EFR from PVC in the urban domestic sector across GB

Step 1: This part is to determine the number of domestic customers (N_h) for each MV node within the GB generic urban distribution network. The MV network model representing a typical UK urban underground distribution system [96] shown in Fig. 3.2 is used here. This is an 11 kV urban network fed from a 33 kV supply point. Downstream LV networks are connected at the ‘green dots’ shown in the figure. The average domestic energy consumption for each MV node is obtained by scaling down from the total base demand across GB by a factor (denoted by SF) which is the ratio between the diversified peak demand (DPD) of individual MV node and that of the peak demand of GB (excluding EV and HP). The peak demand of domestic sector for each MV node is then calculated using the average domestic energy consumption (assuming 37% of the total coming from domestic sector [97]) and a load factor of 0.5 [98]. The number of domestic customers for a particular node is obtained by dividing peak domestic demand at that node by the average DPD of a single household (0.9 kW) [99].

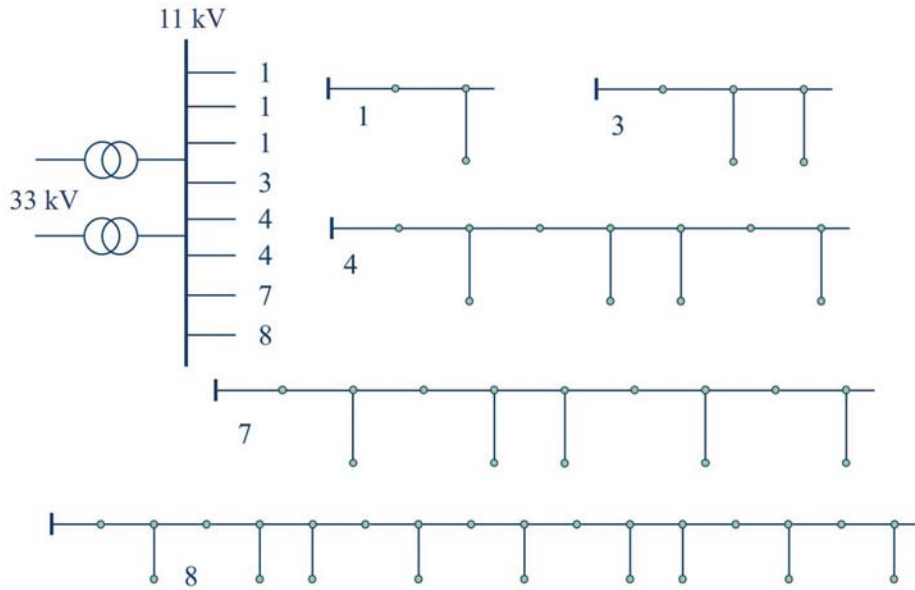


Fig. 3.2 GB generic urban distribution network MV model

Step 2: The downstream LV network configuration is then designed based on the calculated N_h . To be more specific, the generic ‘highly urban network’ and ‘urban network’ from [88] are adjusted by taking a subset of the whole network to fit in the determined N_h . An example of an LV network is shown in Fig. 3.1. Each CDC is then formed by 12 to 48 domestic customers [88] at every single LV node.

Step 3: By running the stochastic demand model by the Centre for Renewable Energy Systems Technology repeatedly [86], the demand profile can be generated, including the

detailed consumption of 35 typical household appliances for each domestic customer considering daily and seasonal variations. Combined with the ZIP load model coefficients of the 35 appliances [87], the demand and power-voltage sensitivity profiles are aggregated from appliance level to single domestic customer level, and then to CDC level.

Step 4: Taking the domestic demand profiles out of the scaled-down base demand of each MV node, the rest are assumed to be industrial and commercial customers, all located at the 11 kV side. The EV and HP loads are also scaled down according to the number of domestic customers at each LV node. The original EV and HP profiles are almost in line with the demand profile of a CDC, referred to as the ‘Non-Smart Case’. Another scenario, called the ‘Smart Case’ in which the EV and HP consumption are optimised for peak shaving [100], is also considered as a more likely situation for the future and is shown in Fig. 3.3. It should be mentioned that all industrial and commercial demand are assumed to be non-responsive to voltage change due to lack of power-voltage sensitivity data while EV and HP typically have negligible voltage dependence.

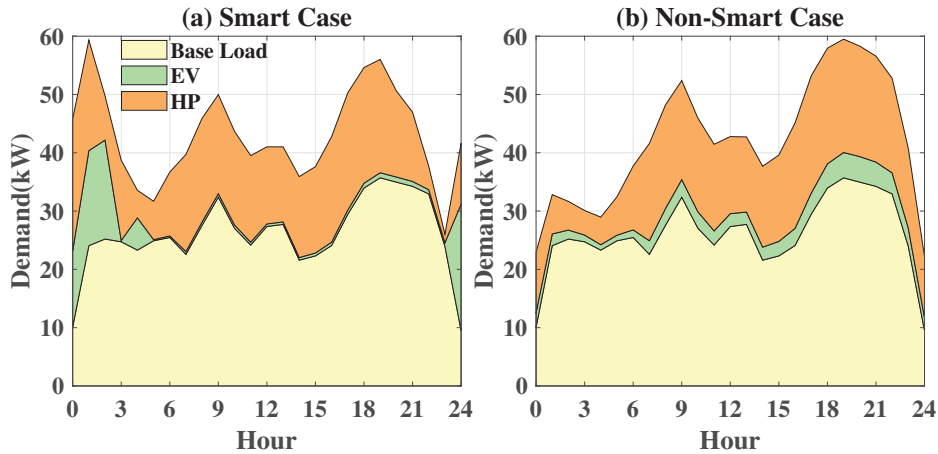


Fig. 3.3 Demand profiles of a CDC as well as EV and HP loads for a typical winter day (a) Smart Case; (b) Non-Smart Case

Step 5: An on-load tap change scheme is applied to the primary substation to control the secondary voltage within target voltage with a deadband of 1.5%. The target voltage is designed based on a load drop compensation scheme [101] as in Table 3.1. Primary voltages are taken from [87] to avoid a detailed modelling of the upstream (> 33 kV) network. For secondary substations, a seasonal off-load tap change scheme is adopted, in which the tap position is +5% for winter and +2.5% for the rest of the year.

Table 3.1 Target voltage boost considering load drop compensation, where nominal target voltage is 1.0 p.u.

Loading (kVA)	0-10	10-15	15-20	>20
Boost (%)	0%	1%	1.5%	2%

Step 6: Based on all the above assumptions and configurations, the EFR (which is the same as DR in Chapter 2) provided by PVC (denoted by EFR_{PVC}) for the urban network is calculated by (2.4) in Chapter 2 and scaled up across GB using the ratio between DPD of the MV network (24.274 MW) and peak of base GB demand (excluding EV and HP) which is 59.146 GW. A conservative correction factor is applied to the final results to account for urban domestic demand only. This factor (74.55%) is determined by population distribution (about 83% urban vs. 17% rural) [102] and extreme cases for energy consumption per head (1.5 MWh for urban vs. 2.5 MWh for rural) [103]. Note that the exact EFR available from PVC could be smaller during a contingency such as generation outage when the voltages in electric vicinity of the outage are generally lower than normal. However, such voltage reduction is typically confined within a small region and therefore, will only have marginal impact on the overall EFR available from PVC across GB.

3.1.2 Enhanced Frequency Response Capability with Point-of-load Voltage Control

In this section, the EFR capability of PVC in the urban domestic sector for the ‘Smart Case’ of 2030 Green World (GnW) scenario is presented and analysed. The characteristics of this 2030 GnW scenario are discussed in Section 3.2.2.

The voltage profiles across all CDCs for the 2030 GnW ‘Smart Case’ are given in Fig. 3.4, while the comparison between EFR provision with PVC and that with voltage control at substation (VCS) is as shown in Fig. 3.5. The three traces in each subplot represent the upper boundary (UB, 95 percentile), median value and lower boundary (LB, 5 percentile) of the results considering daily variations within that season.

The voltages for all CDCs across the year are well within the stipulated range of 0.94 to 1.1 p.u., as defined in standard BS EN 50160 [84]. Note that the lower limit for voltage reduction is 0.95 p.u. to allow for a further 0.01 p.u. voltage drop within a CDC. The three traces in Fig. 3.4 reflect the electric proximity to the substations. The width between upper and lower boundaries of winter and spring is larger than that of summer and autumn due to different

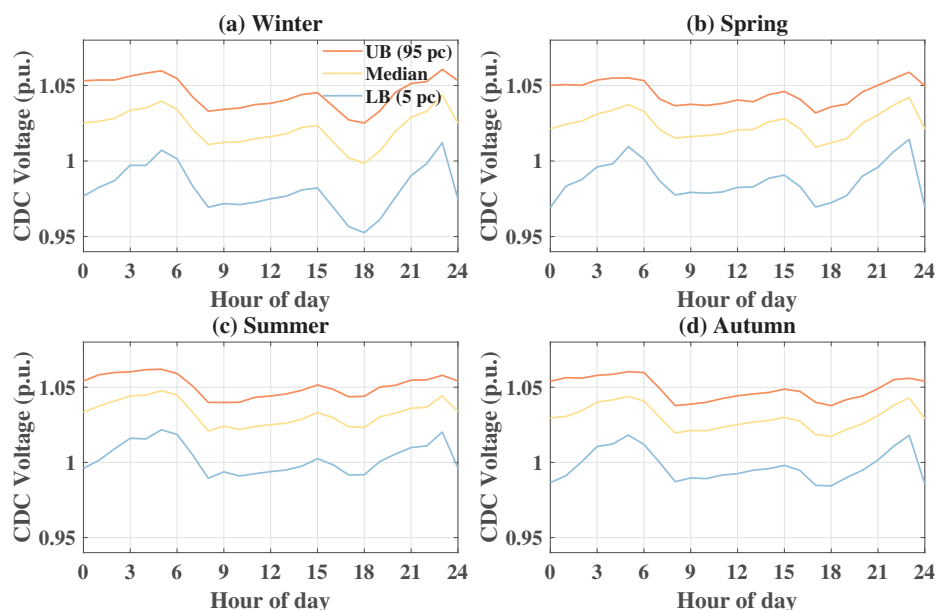


Fig. 3.4 Voltage across CDCs for the 2030 GnW 'Smart Case'

loading levels.

Fig. 3.5 shows that EFR capability provided by PVC ranges from about 0.1 to 1.9GW throughout the year, accounting for 0.5% to 9.4% of the domestic DPD of the corresponding day. Available EFR peaks during 18:00 to 22:00 for all seasons mainly due to high loading levels along with voltage-reduction room for a considerable number of CDCs. In winter and some days of spring and autumn, there is a significant amount of EFR available between midnight and early morning (6 am) due to the presence of electric space heating and also a relatively large room for voltage reduction. However, the number of households which has got the space heating turned on during this time varies a lot between the days of a particular season which causes the variability (the difference between UB and LB) in EFR even during 12 am - 6 am. This variability would be less if the results are shown for individual month instead of seasons.

In contrast to PVC, available EFR through VCS varies from 0 to about 0.85GW. An index 'ΔEFR' as defined in (3.1) further quantifies this comparison. As shown in Fig. 3.5, the EFR availability from VCS is at least 50% lower than that from PVC throughout the year. In some instances, ΔEFR reaches -100%, indicating that VCS completely loses its capability of providing EFR as the voltage at the far end of the feeder is below the allowable limit.

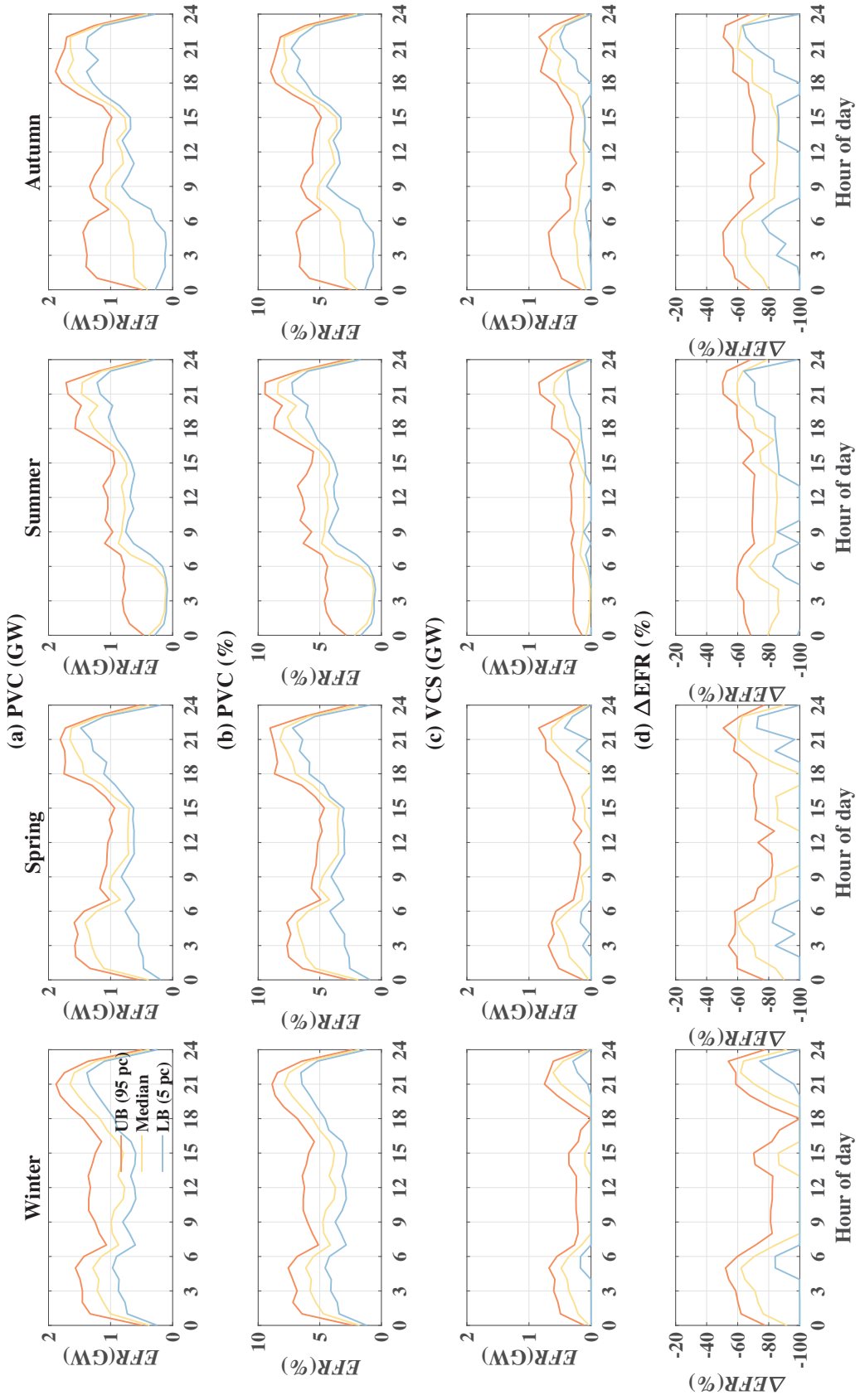


Fig. 3.5 Comparison between EFR with PVC and EFR with VCS for the 2030 GnW 'Smart Case'

$$\Delta \text{EFR}(\%) = \frac{\text{EFR}_{\text{VCS}} - \text{EFR}_{\text{PVC}}}{\text{EFR}_{\text{PVC}}} \times 100\% \quad (3.1)$$

Besides the lower EFR capability aspect, another two disadvantages of implementing EFR via VCS are: 1) parallel feeders with different loading (i.e. voltage drop) could further seriously limit the overall capability of VCS; and 2) the delivery time of EFR should be within one second, which means the VCS would require a large PEC at the substation whose limited fault current capability weakens the feeders.

3.1.3 Investment in Power Electronic Compensators

The rating of the PEC required at the i^{th} CDC is determined by rounding up the maximum power processed by the PEC (as calculated by (2.13) in Chapter 2) to a whole number. For the 2030 GnW ‘Smart Case’, the required PEC rating ranges from 4 to 14 kVA for each CDC, accounting for 6% to 17% of the DPD of respective CDC. This percentage is higher compared to that presented in Chapter 2 as schemes like on-load tap change and load drop compensation etc. are considered. The total required rating would be about 6.6 GVA across the GB if all urban domestic customers are equipped with PECs for PVC.

According to [91], the typical price of single-phase converters is \$140/kW but could vary from \$60/kW to \$220/kW while the maintenance cost is about \$10/kW per year. The variability in the converter cost (including maintenance cost) is considered to determine the range of payback period in Section 3.2.3 with an exchange rate of £1=\$1.25. Note that the customers under PVC do not have to be compensated as the supply voltages will be maintained within the stipulated limits. In fact, the PECs used for PVC can help optimise the supply voltage to maximise customer benefit (e.g. PowerPerfector deployed in the commercial sector) when system services (e.g. EFR) are not necessary.

3.2 Value of Enhanced Frequency Response from Point-of-load Voltage Control

In this section, the benefits of PVC in providing EFR under both normal mode and fully controllable mode are quantified, considering daily and seasonal capability variations obtained from Section 3.1.2. In the normal mode, the capability of EFR delivery depends on the original demand consumption and would not be activated unless there is a need for EFR provision. The fully controllable mode is referred to the case in which the urban

domestic demand is adjusted hourly to consume more/less (within stipulated voltage range) as necessary to offer more/less EFR.

3.2.1 Methodology

The frequency-constrained SUC model proposed in [93] is applied here for assessing the value of implementing PVC in the urban domestic sector. The model simultaneously optimises energy production as well as provision of primary frequency response (PFR) and EFR in the light of wind generation uncertainties.

Uncertainties are modelled using a scenario tree, which represents user-defined quantiles of the distribution of the stochastic variable as described in [104]. A rolling scheduling is applied here: for each time step ($\Delta\tau(n) = 1\text{h}$ in our case), a scenario tree covering a 24-hour horizon is built and the SUC optimisation over all nodes in the scenario tree is computed correspondingly. Only the here-and-now decisions in the current-time node are preserved with all future decisions discarded. This process is repeated for each time step. A schematic diagram of a scenario tree is shown in Fig. 3.6.

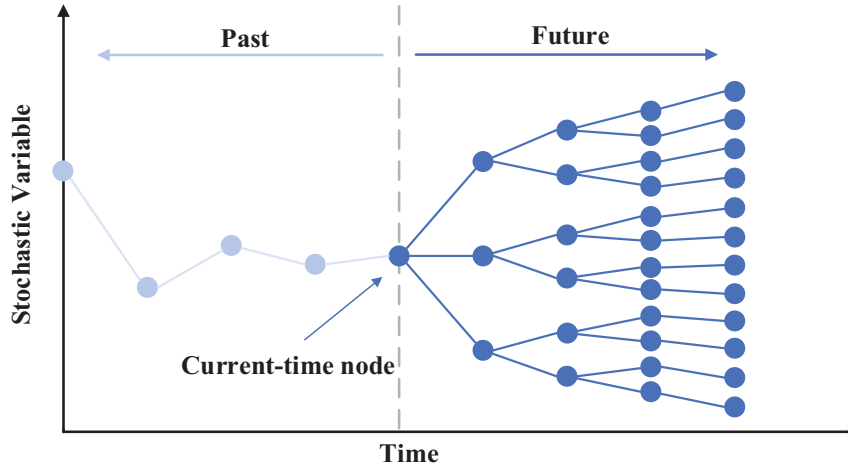


Fig. 3.6 Example of a scenario tree used in the SUC model

The objective is to minimise the expected operation cost:

$$\sum_{n \in \mathcal{N}} \pi(n) \left(\sum_{g \in \mathcal{G}} C_g(n) + \Delta\tau(n) \left[c^{\text{ls}} P^{\text{LS}}(n) \right] \right) \quad (3.2)$$

in which the operating cost of generator g in node n ($C_g(n)$) is given by (3.3) and the latter term represents the load shed penalty. Note that the variables in (3.2) to (3.8) in italics

represent decision variables while the others denote constants and parameters. $\pi(n)$ and $\Delta\tau(n)$ are the probability of reaching node n and the time-step corresponding to node n . c_g^{ls} , c_g^{st} , c_g^{nl} and c_g^{m} stand for load shed penalty, startup, no-load and marginal cost of generating units g while P^{LS} , P_g , N_g^{sg} and N_g^{up} denote load shed, power produced by unit g and the number of units start generating and online in node n respectively.

$$C_g(n) = c_g^{\text{st}} N_g^{\text{sg}}(n) + \Delta\tau(n) \left[c_g^{\text{nl}} N_g^{\text{up}}(n) + c_g^{\text{m}} P_g(n) \right] \quad (3.3)$$

The objective function is subject to a series of constraints. Only the load-balance and frequency-security constraints are listed here as they are directly associated with the introduction of PVC. For all other operating constraints of thermal plants and storage, readers are advised to refer to the Appendix of [105]. Index n is omitted in following equations for simplicity.

The load-balance constraint is given by:

$$\sum_{g \in \mathcal{G}} P_g + \sum_{s \in \mathcal{S}} P_s + P^{\text{WN}} - P^{\text{WC}} = P^{\text{D}} + P^{\text{PVC}} - P^{\text{LS}} \quad (3.4)$$

where P^{D} denotes all demand in the system except the urban domestic customers with PVC; P^{WN} , P^{WC} and P_s are total available wind power, wind curtailment and power provided by storage unit s . In the normal mode, P^{PVC} is the demand equipped with PVC and it is a constant for each node while in the fully controllable mode, the demand becomes a decision variable (P^{PVC}) within boundaries of $[P_{\min}^{\text{PVC}}, P_{\max}^{\text{PVC}}]$.

Frequency security constraints that guarantee RoCoF, quasi-steady-state and nadir requirements are given by equations (3.5) to (3.7), in which P_L^{\max} and H_L are the largest power infeed and the corresponding inertia constant, as deduced in [93]:

$$H = \sum_{g \in \mathcal{G}} H_g \cdot P_g^{\max} \cdot N_g^{\text{up}} - P_L^{\max} \cdot H_L \geq \left| \frac{P_L^{\max} \cdot f_0}{2 \text{RoCoF}_{\max}} \right| \quad (3.5)$$

$$R_{\mathcal{G}} + R_{\mathcal{E}} \geq P_L^{\max} \quad (3.6)$$

$$\left(\frac{H}{f_0} - \frac{R_{\mathcal{E}} \cdot T_e}{4 \cdot \Delta f_{\max}} \right) \cdot R_{\mathcal{G}} \geq \frac{\left(P_L^{\max} - R_{\mathcal{E}} \right)^2 \cdot T_g}{4 \cdot \Delta f_{\max}} \quad (3.7)$$

where:

$$R_{\mathcal{E}} = EFR_{PVC} + EFR_S \quad (3.8)$$

$$EFR_S \leq \bar{P}_s - P_s \quad (3.9)$$

Note that virtual inertia from wind is not considered and the expression in (3.7) neglects load damping for simplicity. $R_{\mathcal{E}}$ corresponds to total PFR from all generators while EFR ($R_{\mathcal{E}}$) is provided by both storage units and urban domestic demand with PVC, as in (3.8), where the maximum value of EFR_{PVC} is obtained by (2.4) as described in Section 3.1 and EFR_S is limited by the difference between maximum discharge rate (\bar{P}_s) and actual discharge rate/power output (P_s). For example, a BESS with 0.5GW capacity can provide up to 1GW of EFR if it is fully charging (i.e. $P_s = -0.5\text{GW}$), and 0GW if it is fully discharging. Due to the non-linearity of (3.7), a linearisation method is required to be implemented in a Mixed-Integer Linear Program. Readers are advised to refer to [93] for further details.

With the above methodology, the value and the corresponding payback of PVC is quantified by computing the reduction in system operating cost. The benefits in CO₂ emission and wind curtailment reduction are also presented.

3.2.2 Scenarios

Two future scenarios for GB's generation and demand, i.e. 2030 Slow Progression (SwP) and 2030 Green World (GnW), are considered here. These two scenarios are taken from a report on conflicts and synergies of demand side response [106], in which the GnW is aligned with a Department of Energy and Climate Change (DECC) scenario while the SwP is a world developed by [106] based on today's trajectory. The peak demand for the 2030 GnW 'Non-Smart Case' and 'Smart Case' are respectively of 78.6 and 76.2GW, while for the 2030 SwP scenario the numbers become 66.5 and 65.5GW. The installed wind capacity is of 72.8 and 41.8GW for 2030 GnW and SwP, respectively. The configuration and characteristics of the main thermal plants are summarised in Table 3.2. A biomass plant of 1.75GW-rating is also present in both scenarios, while five additional coal units with Carbon Capture and Storage capabilities are also included in the 2030 GnW case, with a rating of 0.7GW each. It is to be noted that there are more Coal and OCGT units in GnW than that in SwP as the installed wind capacity is much higher in GnW which would require more frequency response services from conventional plants. Also, no specific prices for frequency services (PFR, EFR) are considered in the SUC model as the idea is to understand the real value of

different services, not considering the particular characteristics of a market.

Table 3.2 Characteristic of Main Thermal Plants

	Nuclear	CCGT	OCGT	Coal
Number of Units (2030 SwP)	5	94	33	0
Number of Units (2030 GnW)	6	70	75	4
Rated Power (MW)	1800	467	205	836
Min Stable Generation (MW)	1800	233.5	82	292
No-Load Cost (£/h)	391	2641	11328	4474
Marginal Cost (£/MWh)	4.82	68.75	195.12	86.6
Startup Cost (£)	49362.5	32000	0	21000
Startup Time (h)	N/A	4	0	4
Min Up Time (h)	N/A	4	1	4
Min Down Time (h)	N/A	0	1	0
Inertia Constant (s)	5	5	5	5
Max PFR deliverable (MW)	0	233.5	40	300
Emissions (kgCO ₂ /MWh)	0	394	557	925

Besides, a pumped storage unit with 10GWh capacity, 2.6GW rating and 75% efficiency is also present in both scenarios, corresponding to the Dinorwig unit in GB. Along with PVC in the urban domestic sector, Battery Energy Storage Systems (BESS) with a 2.5GWh tank, 0.5GW rating and 90% round-trip efficiency also serves to provide EFR. The delivery time of EFR (T_e) and PFR (T_g) are 0.5s and 10s respectively. The largest infeed power loss (P_L^{\max}) is 1.8GW and the load shed penalty (c^{ls}) is £50k/MWh. Dynamic frequency requirements are: $\Delta f_{\max} = 0.8\text{Hz}$, $\Delta f_{\max}^{ss} = 0.5\text{Hz}$ and $\text{RoCoF}_{\max} = 0.5\text{Hz/s}$. The optimisation problem was solved with FICO Xpress 8.0, linked to a C++ application via the BCL interface [107].

3.2.3 Point-of-load Voltage Control in Normal Mode

Under the normal mode, PVC would not be utilised (or activated) i.e. voltage (and hence, actual power consumption) of the CDCs would not actually be reduced to the minimum stipulated limit. The maximum capability of providing EFR is determined by reducing all CDCs' voltages to the minimum stipulated value, as obtained in Section 3.1.2. In this subsection, the benefits of PVC are shown for different percentages of urban domestic loads under PVC for all scenarios.

System Operation Cost

The operation costs (in £b) for the Non-Smart and Smart cases in the 2030 GnW and SwP scenarios with 0%, 30%, 60% and 100% of urban domestic customers under PVC are presented in Fig. 3.7. With 100% of urban domestic loads with PVC, the maximum operation cost saving can be as high as £0.72b in the 2030 GnW ‘Non-Smart Case’ while the minimum number is about £0.23b in the 2030 SwP ‘Smart Case’. The cost reduction is due to PVC’s displacement of conventional thermal generators for providing frequency response to a certain extent. The higher cost saving observed in the GnW scenario and ‘Non-Smart Case’ can be explained as, in these circumstances, there would be larger variations in differences between wind generation and the demand, which increases the need for (and value of) EFR.

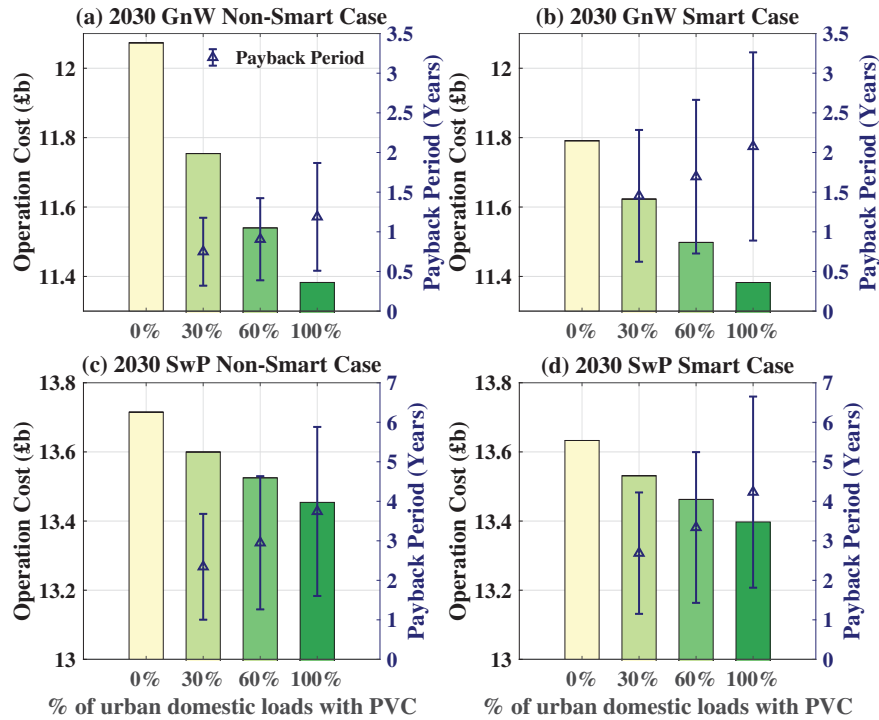


Fig. 3.7 Operation cost and payback period for (a) 2030 GnW Non-Smart Case; (b) 2030 GnW Smart Case; (c) 2030 SwP Non-Smart Case; (d) 2030 SwP Smart Case

Along with the operation cost, the payback period (PP) is shown as well, considering the investment in PVC as calculated in Section 3.1.3. Depending on the percentage of loads with PVC, the payback period ranges from 0.3 to 3.3 years for 2030 GnW and 1 to 6.7 years for 2030 SwP, respectively considering a range of converter price. The increase in payback period with increasing percentage of loads with PVC points to a saturation effect, i.e. the first megawatts of EFR from PVC generate the highest economic value for the system. It is

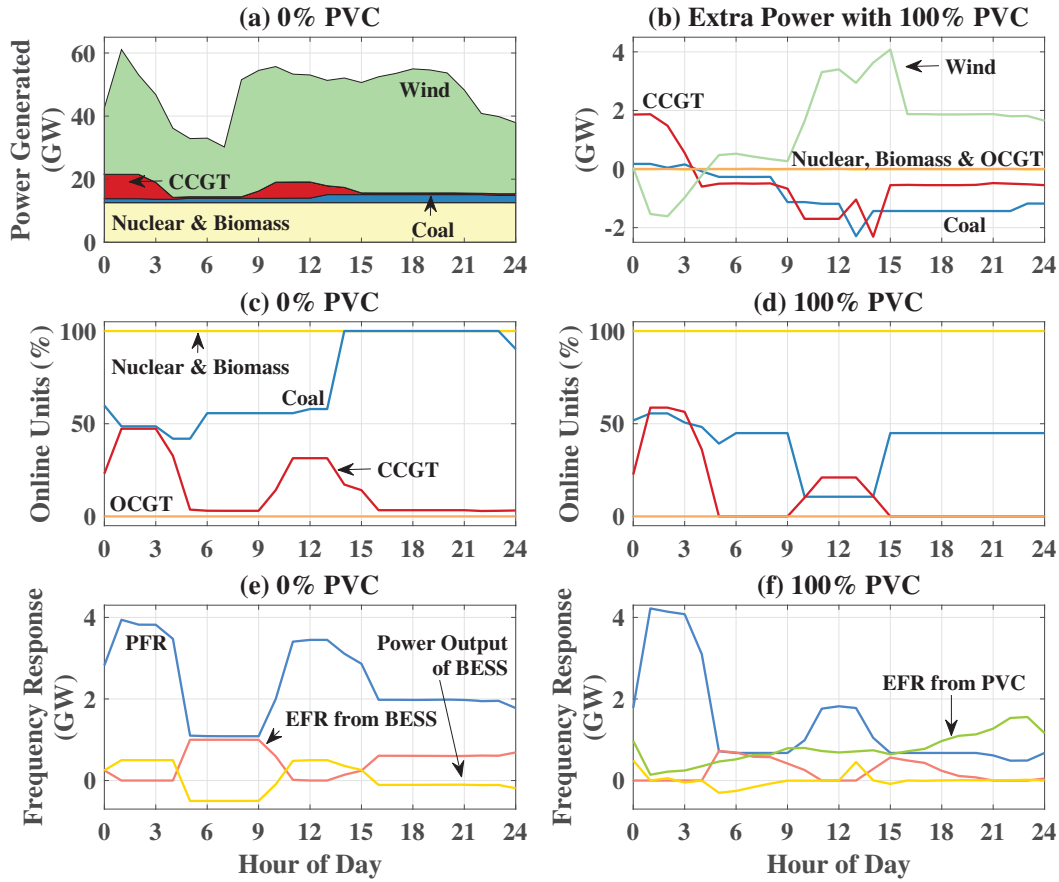


Fig. 3.8 24-hour dispatch profile for different types of generation and frequency response for a day with low net-demand in 2030 GnW SC

to be noted that the calculated payback periods are still conservative as the cost savings do not include carbon price, for example. Moreover, only single-phase PECs are considered which have higher price in \$/kW compared to three-phase PECs (as outlined in [91]) which makes the payback period even more pessimistic.

To further get useful insight into the cost savings realized through PVC, the dispatch profiles for two days with low and high net-demand (demand minus wind accommodated) are shown in Figs. 3.8 and 3.9. It is to be noted that subplots 3.8 (b) and 3.9 (b) represent the extra power generated by each type of generation with 100% PVC compared to the case without PVC. Following observations can be made from Figs. 3.8 and 3.9:

a) During low net-demand periods in Fig. 3.8, the benefit of using PVC for EFR provision is very high as it reduces the number of online part-loaded coal and CCGT units that are otherwise required to provide PFR to accommodate more wind generation. As shown in Fig.

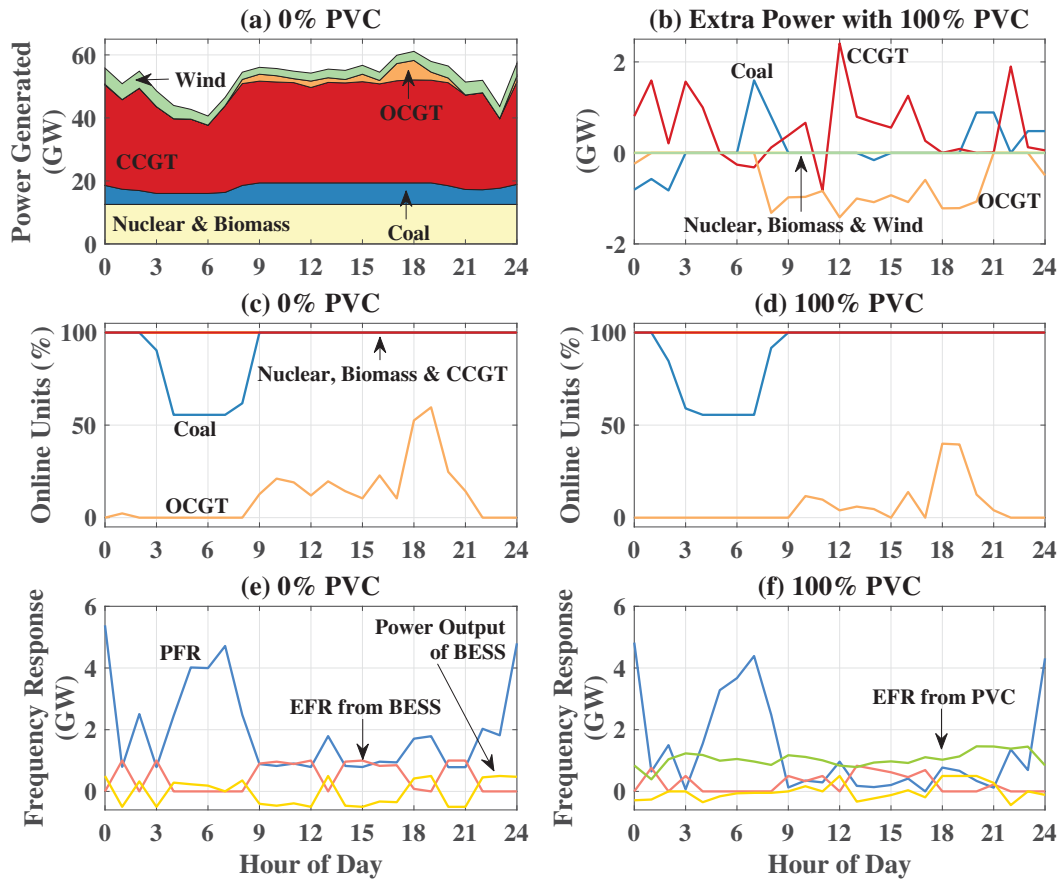


Fig. 3.9 24-hour dispatch profile for different types of generation and frequency response for a day with high net-demand in 2030 GnW SC

3.8, both number of online coal and CCGT units and their power output are significantly reduced while more wind is accommodated. b) During high net-demand periods in Fig. 3.9, the reduction in operation cost from implementing PVC is moderate but still noticeable. The cost saving in this case mainly comes from relieving CCGTs from the PFR duty so that less generation from expensive OCGTs is required to supply the load. As shown in Fig. 3.9, the number of online OCGT units and their power output is much less between 8:00 and 22:00 when PVC provides EFR. c) The EFR scheduled from BESS is lower in presence of PVC for both high and low net-demand, referred to Figs. 3.8 (f) and 3.9 (f). This means that the BESS can be used more frequently for energy arbitrage instead of providing EFR, which is another key advantage of the PVC.

Wind Curtailment

Besides the economic value, the benefits of EFR from PVC to accommodate wind generation are shown in Fig. 3.10, in terms of average wind curtailment percentage with respect to the available wind power throughout the year. With 100% of urban domestic loads equipped with PVC, the wind accommodation capability can be increased by about 1.1% and 0.82%, for the 2030 GnW and SwP scenarios, respectively. Although this number may seem marginal, it could increase the wind energy capture up to around 3.3TWh per year for the 2030 GnW ‘Smart Case’.

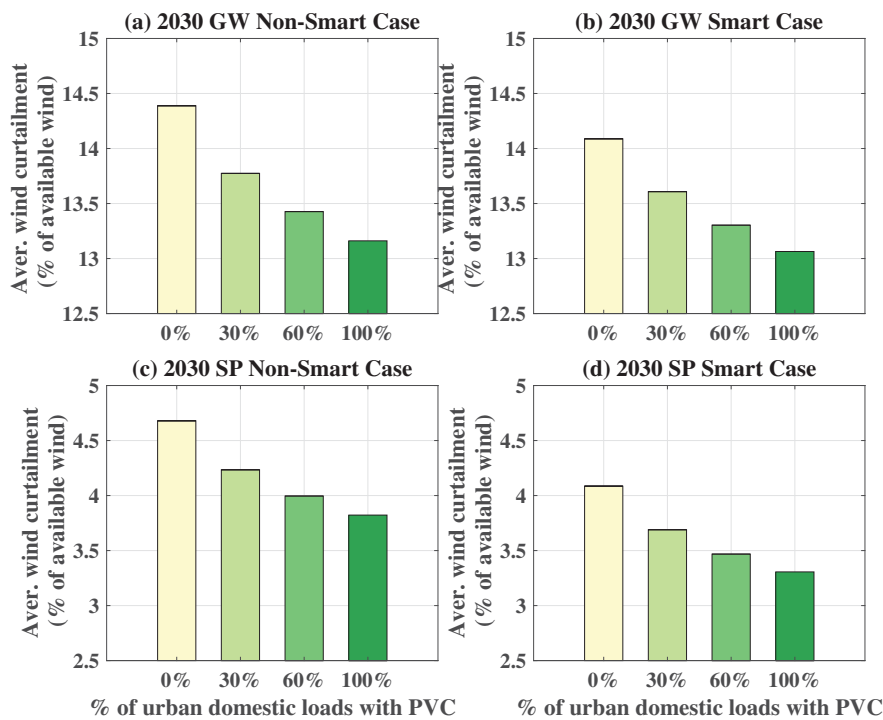


Fig. 3.10 Average wind curtailment (% of available wind) for (a) 2030 GnW Non-Smart Case; (b) 2030 GnW Smart Case; (c) 2030 SwP Non-Smart Case; (d) 2030 SwP Smart Case

CO₂ Emission

Additionally, the environmental benefits of EFR from PVC are also evaluated in terms of carbon emissions. The average system emission rate is calculated by the ratio between total system emissions and the overall demand. The emission rates for each type of generation, as given in Table 3.2, are considered to calculate this ratio, using the generation output for each thermal unit from the solution of the SUC. As can be seen in Fig. 3.11, the CO₂ emission reduction for the 2030 GnW scenario can be 2 to 3 times than that in the 2030 SwP scenario.

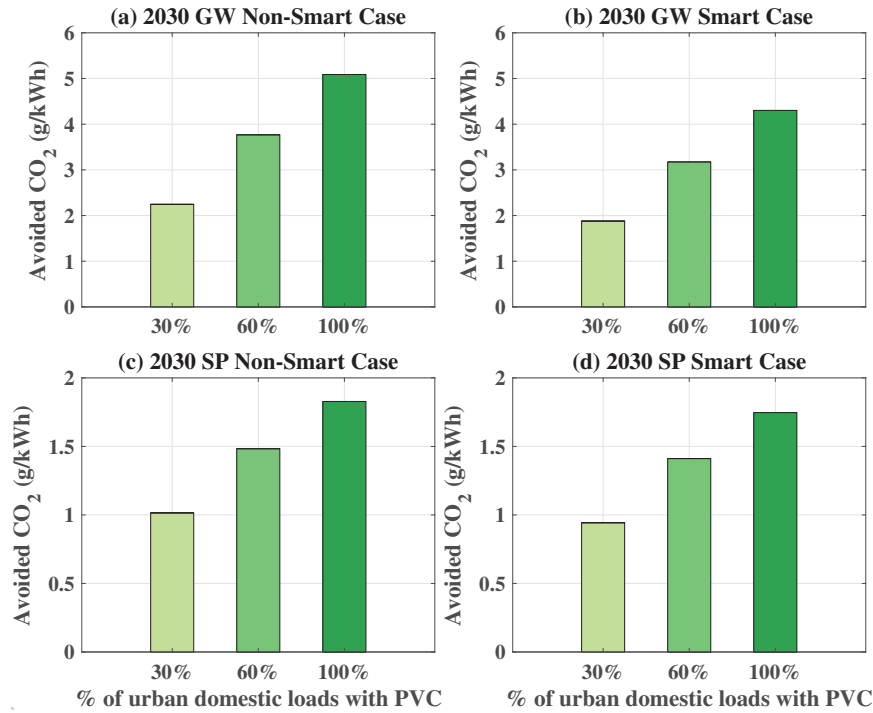


Fig. 3.11 Avoided CO₂ emissions (g/kWh) for (a) 2030 GnW Non-Smart Case; (b) 2030 GnW Smart Case; (c) 2030 SwP Non-Smart Case; (d) 2030 SwP Smart Case

This results can be explained by the fact that PVC in the domestic sector is displacing traditional thermal generators for providing frequency response, and the requirement for response increases for higher wind penetration levels.

3.2.4 Point-of-load Voltage Control in Fully Controllable Mode

The fully controllable mode allows to increase the load power consumption beforehand in order to provide more EFR, at the expense of more energy consumption during a certain period of time. Intuitively, the increase in demand will give rise to energy cost as well. However, if the increased consumption can be covered with extra wind generation that is accommodated, which is clean and has zero marginal cost, it can actually be cost-effective. This mode also enables demand with PVC to consume more flexibly, i.e. consume less when net demand (ND, demand minus wind accommodated) is high (less EFR required), which adds additional operation cost reduction by energy saving in this case compared with the normal mode. The above analysis is demonstrated in Fig. 3.12, where all ‘Case B’ show a further reduction in operation cost with a maximum of £0.19b under the 100% PVC equipped level. It’s interesting to point out that the operation cost of Case B with 60% urban domestic

demand with PVC is even less than that of Case A with 100% PVC equipped level.

A comparison between provision of EFR from PVC under the normal mode (referred to as ‘Case A’) and that under the fully controllable mode (referred to as ‘Case B’) in terms of economic value for the 2030 GnW ‘Smart Case’ is presented in Fig. 3.12.

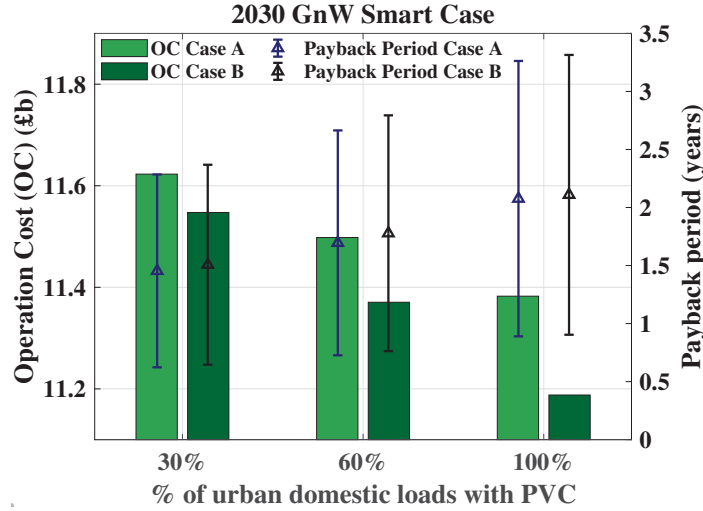


Fig. 3.12 Operation cost and payback period for 2030 GnW Smart Case under normal (Case A) and fully controllable cases (Case B)

Although the fully controllable mode could bring in extra economic value, it also requires an additional investment cost due to the increase of the required rating of PECs deployed at each CDC. The power processed by PECs when increasing the voltage to the maximum stipulated value is calculated by replacing V_{\min} in equation (2.13) with V_{\max} and considering maximum of these two cases, which leads to about 50% increase in rated capacity of the PECs. This leads to a slightly longer payback period than the normal case (Case A) as shown in Fig. 3.12.

To further investigate this fully controllable mode, an index (C_{PVC}) indicating the demand decision by the urban domestic sector is defined as in (3.10). P_{\min}^{PVC} and P_{\max}^{PVC} denote the minimum and maximum possible demand with PVC, which are calculated by the nominal demand, V_{\min} and V_{\max} along with the corresponding power-voltage sensitivities, neglecting the change in network and converter losses for simplicity. A value of C_{PVC} approaching 1 (0) implies the consumption decision approximating its maximum (minimum).

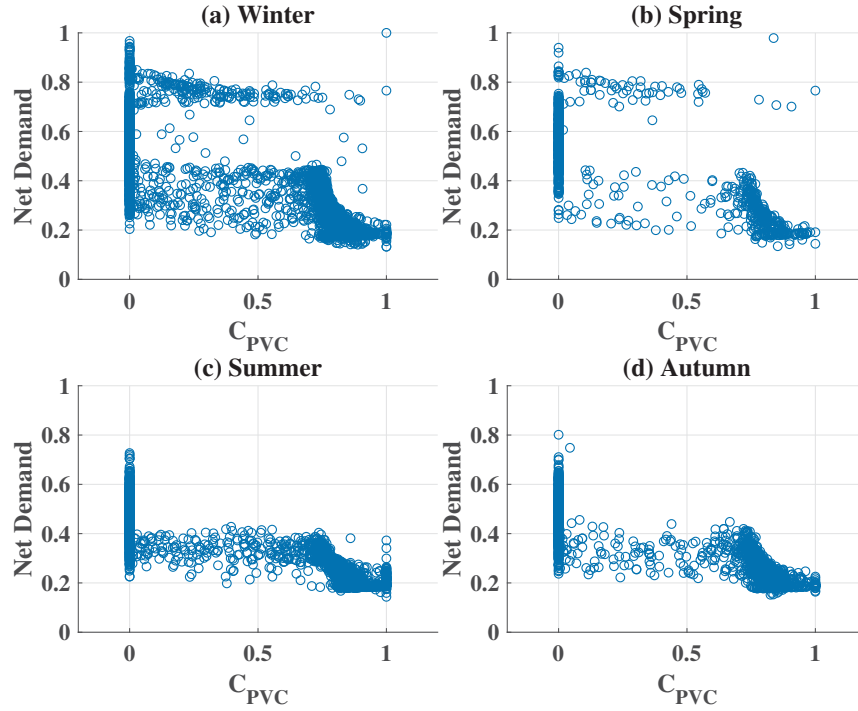


Fig. 3.13 Correlation between the urban domestic sector consumption and system net demand (with 0.5GW BESS, 100% of urban domestic loads with PVC) (a)winter; (b)spring; (c)summer; (d)autumn

$$C_{PVC} = \frac{P_{PVC} - P_{min}^{PVC}}{P_{max}^{PVC} - P_{min}^{PVC}} \quad (3.10)$$

A correlation between C_{PVC} and system ND (normalised with respect to the maximum of the year) for each hour of the case with 100% of urban domestic demand with PVC is presented in Fig. 3.13. It can be seen that for a majority of cases, domestic customers with PVC are chosen to consume more when the ND is low, while consume less when the ND is relatively substantial. This is reasonable and cost-effective as the ND actually represents the demand required to be served by conventional thermal plants. When the ND is high, it is more likely that there are more thermal plants online to cover that ND, thereby requiring less EFR and vice versa.

However, it should be mentioned that there are some instances when the above trend is not followed strictly. For example, PVC could control the demand to consume relatively more even under relatively high ND (about 0.8) as the wind availability could drop significantly in the next hour, which leaves the thermal generators much less capable of providing frequency

response services. As shown in Fig. 3.13, these cases happen much more frequently during winter and spring when the wind energy is more volatile [100].

Also, it is to be noted that $C_{PVC} = 0$ is chosen for every value of ND within the vertical line shown in each sub-figure of Fig. 3.13 in which the ND of some instances can be very low. The reason behind it is that in those cases, all the wind available has already been accommodated, which means increasing the consumption from PVC would also increase the cost of energy.

3.2.5 Impact of Battery Energy Storage System

Currently, the GB power system holds around 0.48 GW of battery storage providing EFR [108]. A scenario with 1 GW rating of BESS is presented in Fig. 3.14 to evaluate the impact of this competing option on the economic value of EFR provision from PVC. As expected, the operation cost savings from PVC utilisation are reduced substantially (by about 45% for all normal cases) when the BESS rating is doubled as shown in Fig. 3.14 (a).

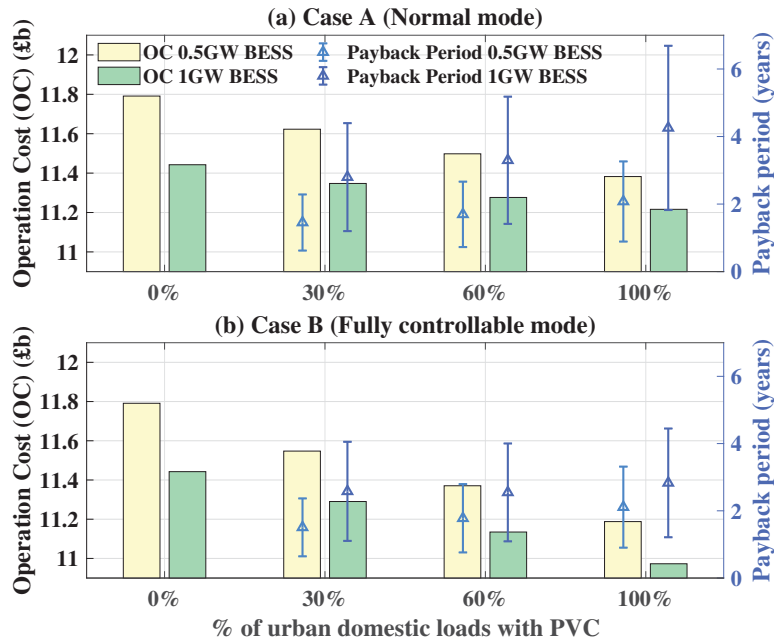


Fig. 3.14 Impact of BESS on the economic value of EFR provision from PVC, for two different ratings of the BESS: 0.5GW and 1GW

However, it's interesting to note that with 1GW BESS in the system, the fully controllable mode ('Case B') gains more economic value than that in case of 0.5GW BESS, which leads

to a significant decrease in payback period as shown in Fig. 3.14 (b). This is due to the fact that the extra BESS provides more flexibility to the system, allowing the PVC to reduce the number of hours when it has to increase consumption for high ND conditions. This trend can be easily be observed by comparing the correlation between C_{PVC} and system ND in both cases, with many fewer dots circled out in Fig. 3.15 compared to those in Fig. 3.13.

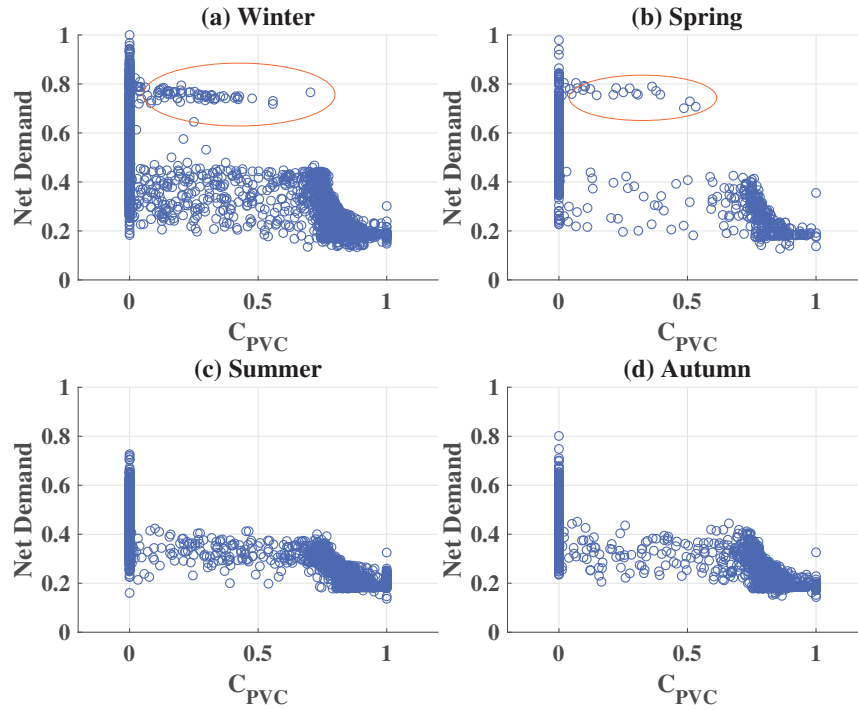


Fig. 3.15 Correlation between the urban domestic sector consumption and system net demand (with 1GW BESS, 100% of urban domestic loads with PVC) (a)winter; (b)spring; (c)summer; (d)autumn

3.3 Conclusion

This chapter extends the study in Chapter 2 in value assessment of point-of-load voltage control (PVC) demand response. The demand reduction from PVC is utilised to provide enhanced frequency response (EFR), which could result in considerable economic benefits in future low-carbon Great Britain (GB) system as it displaces conventional thermal generators for providing frequency response to a certain extent. The evaluation is analysed through a stochastic unit commitment (SUC) model with constraints for secure post-fault frequency evolution.

It is estimated that PVC in the urban domestic sector of GB can provide up to 1.9 GW of EFR depending on the time of the day and the season. This results in annual savings in system operation cost of £0.23b and £0.72b for 2030 Slow Progression (SwP) and 2030 Green World (GnW) scenarios, respectively. The payback period for the investment in installing the power electronic compensators (PECs) for PVC varies between 0.3 to 6.7 years. The payback period increases beyond 30% penetration of PVC within the GB urban domestic sector due to the diminishing value of EFR above a certain point. Increasing the demand for higher EFR provision or reducing it as necessary is shown to decrease the overall annual system operation cost by a further £0.19b for 2030 GnW scenario with only marginal increase in payback period. In this case, increasing the system-wide installed capacity of battery energy storage system (BESS) from 0.5GW to 1GW reduces the payback period further demonstrating the fact that PVC could effectively complement BESS towards EFR provision in future GB power system.

Chapter 4

Virtual Inertia from Point-of-load Voltage Control

The fast demand reduction (DR) capability of point-of-load voltage control (PVC) introduced in Chapter 2 can be utilised to contribute to virtual inertia. In this chapter, the equivalent virtual inertia and load damping effects from PVC are firstly verified. A case study based on the CIGRE microgrid benchmark is then included to demonstrate the increase in system inertia with PVC. The work presented in this chapter was done in collaboration with Mr Tong Chen from the University of Hong Kong. Mr Chen mainly contributed to the design of virtual inertia from PVC along with the comparison between virtual inertia from the supply-side and load-side (introduced in the resulting paper [109]) while I mainly focused on system level quantification and time domain verification.

4.1 Load-side Virtual Inertia

The inertia of future power system is expected to decrease with increasing penetration of converter-interfaced renewable energy resources (RESs). Sufficient inertia is required to avoid large frequency fluctuations and also limit the excessive rate of change of frequency (RoCoF). Although converter-interfaced RESs do not inherently contribute to system inertia, the power control loop of the converters can be modified to provide ‘virtual’ inertia without the need for any energy storage [110].

Several utilities (e.g. Hydro Quebec [111]) require the wind turbine generators to provide inertial response by reducing the turbine speed to release the stored kinetic energy. Although there is significant amount of kinetic energy stored in wind turbines [112, 113], their virtual inertia contribution is limited by several factors such as the recovery phase (depending on

the prevailing wind speed) to regain the turbine speed, the rated capacity of the grid interface power converters and the mechanical stress on the turbine components and the associated impact on lifetime.

For solar photovoltaic (PV), virtual inertia can be provided by operating below maximum available power (i.e. part-rated operation) [114] to keep a margin for increasing the power output when required. The economic implication of such part-rated operation needs to be carefully considered against alternative sources of virtual inertia [115]. This is where PVC could complement the existing solutions as an additional source of virtual inertia.

The energy reserved in the dc-link capacitors of grid-side-converter can be also exploited for virtual inertia emulation [116, 117]. However, the virtual inertia achieved in this way is rather limited in the real application unless larger capacitor or super-capacitor is used. It is reported that 17 times of the normal HVDC link capacitance is needed if one wants to achieve a considerable virtual inertial coefficient of $H = 2.5\text{s}$ by allowing 10% dc voltage deviation [118] in a HVDC link for an offshore wind farm. Similar drawbacks also exist for modified RESs.

Unlike the above methods of obtaining virtual inertia on the supply-side, this chapter aims at studying virtual inertia on the load-side, which can be achieved from the DR with PVC. Note that there are already published works regarding trials of virtual inertia provision from the demand-side [119, 120], however, this chapter is the first to quantify the capability based on high-resolution stochastic demand models. The equivalent virtual inertia and load damping effect from the demand side is analysed based on a very simple model: a generator supplying a load with PVC-B2B, as shown in Fig. 4.1. Note that the nominal load line-to-line RMS voltage and the nominal active power consumption (i.e. the demand active power consumption when injected voltage is zero) are taken as the base voltage and base power respectively. And \bar{x} represents variable x in the per-unit system. The frequency-dependent characteristic of the load is neglected for simplicity.

As described in Chapter 2, the series converter controls both the magnitude (V_c) and phase angle (ϕ) of the injected voltage while the shunt converter is controlled to maintain the DC link voltage supporting the active power exchanged by the series converter. For virtual inertia and load damping effect provision, the injected voltage is set to be in phase of the feeder-side voltage while the magnitude (V_c) depends on the proportional (K_1) and derivative gain (K_2),

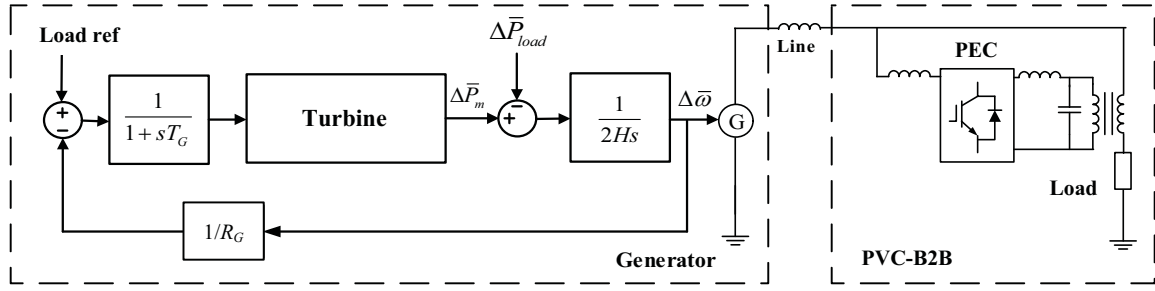


Fig. 4.1 Block diagram of a generator supplying a load with PVC-B2B

as in (4.1). A dynamic saturation limit would be implemented to ensure the voltage of the load is kept within allowable range.

$$\Delta V_l = -V_c = \frac{V_{l0}}{\omega_0} \left(K_1 \Delta \omega + K_2 \frac{d\omega}{dt} \right) \quad (4.1)$$

where ΔV_l denotes the incremental change in load-side voltage, V_{l0} and ω_0 are the nominal load-side voltage and angular velocity. The negative sign indicates that the load voltage would be reduced if an in-phase voltage is injected by the power electronic compensator (PEC). The incremental change in load power consumption can be expressed as (4.2), in which P_{L0} denotes the nominal active power consumption.

$$\Delta P_l = n_p P_{l0} \left(\frac{V_l}{V_{l0}} \right)^{n_p} \frac{\Delta V_l}{V_l} \quad (4.2)$$

The proportional (K_1) and derivative gain (K_2) are chosen as:

$$K_1 = \frac{\Delta V_{\max}}{V_{l0}} \frac{f_0}{\Delta f_{\max}} = \frac{\Delta V_{\max}}{V_{l0}} \frac{\omega_0}{\Delta \omega_{\max}} \quad (4.3)$$

$$K_2 = \frac{\Delta V_{\max}}{V_{l0}} \frac{f_0}{(df/dt)_{\max}} = \frac{\Delta V_{\max}}{V_{l0}} \frac{\omega_0}{(d\omega/dt)_{\max}} \quad (4.4)$$

where the ΔV_{\max} , Δf_{\max} and $(df/dt)_{\max}$ are the maximum allowable load voltage variation, system frequency and frequency change respectively. The control gains are designed according to the UK National Grid requirement ($\Delta f_{\max} = 0.8\text{Hz}$ [121] and $(df/dt)_{\max} = 1\text{Hz/s}$ [122]). In this study, $\Delta V_{\max}/V_{L0}$ is set at 5%. So the K_1 and K_2 values calculated by (4.3) and (4.4) are 3.125 and 2.5 respectively.

According to the kinetic theory of the generator (J is the rotational inertia of the generator) [82]:

$$\Delta P_m - \Delta P_l = J\omega \frac{d\omega}{dt} \quad (4.5)$$

From (4.2) and (4.5), (4.6) can be derived in the per-unit system:

$$\Delta \bar{P}_m - \left(\frac{V_l}{V_{l0}} \right)^{n_p-1} n_p K_1 \Delta \bar{\omega} = \left(2H + \left(\frac{V_l}{V_{l0}} \right)^{n_p-1} n_p K_2 \right) \frac{d\bar{\omega}}{dt} \quad (4.6)$$

$$H = J\omega^2 / 2P_{l0} \quad (4.7)$$

The relationship between the frequency and power fluctuations can be then expressed as:

$$\frac{\Delta \bar{\omega}}{\Delta \bar{P}_m} = \frac{1}{2 \left(H + \left(\frac{V_l}{V_{l0}} \right)^{n_p-1} \frac{n_p K_2}{2} \right) s + \left(\frac{V_l}{V_{l0}} \right)^{n_p-1} n_p K_1} \quad (4.8)$$

$$= \frac{1}{2(H + H_L)s + D_L} \quad (4.9)$$

Formula (4.9) can be expressed using the block diagram as shown in Fig. 4.2, in which the red blocks denote the equivalent effect from PVC. It is found that DR from PVC actually adds two terms in the frequency response block diagram: one is the virtual inertia term H_L and the another is the load damping term D_L . Assuming the allowable load voltage variation to be small, say $\pm 5\%$, the virtual inertia (H_L) and load damping effect (D_L) gained from PVC can be roughly given by:

$$H_L = n_p K_2 / 2 \quad (4.10)$$

$$D_L = n_p K_1 \quad (4.11)$$

According to (4.10), the inertia H_L from PVC could be at most around 2.5s (when $n_p = 2$) based on its power rating.

4.2 Test Case: CIGRE Benchmark Microgrid

To further substantiate and evaluate the inertia support from PVC, a case study is presented using an isolated microgrid scenario with CIGRE European benchmark medium- and low-voltage (MV/LV) network. The level of inertia contributed by PVC for different time periods

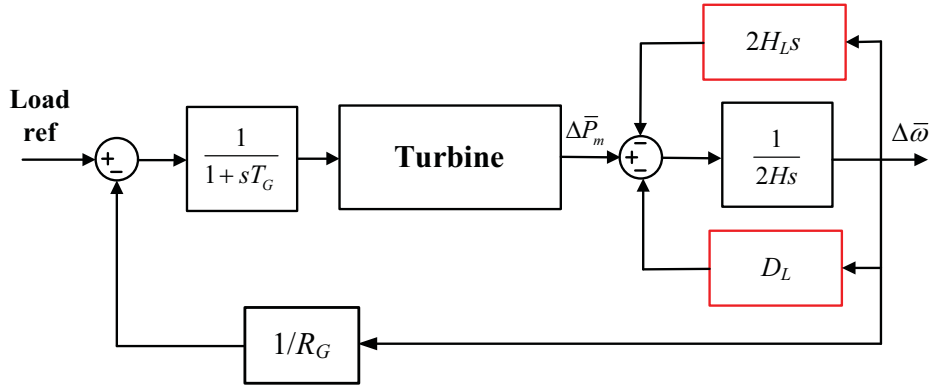


Fig. 4.2 Block diagram of system frequency with equivalent effect of PVC

of the day is firstly presented. Then the results of a time domain simulation are included to demonstrate the capability of virtual inertia and load damping effects from the demand side.

4.2.1 System Description

The network topology (as shown in Fig. 2.12) and loading situation for the scenario are exactly the same as the one described in Chapter 2.4. The CIGRE MV/LV benchmark model is modified into an isolated microgrid, which is served by two diesel generators at bus 1 & 12 with a capacity of 3.125MVA each and 1MW wind power generation connected at bus 7, operated under the maximum power point tracking mode with unity power factor at its point of coupling.

The diesel generators are represented using a third-order dynamic model with the parameters provided in [123]. The IEEE-DC1A type excitation system and governor (using first-order model) with 5% power frequency droop are used for both generators. More detailed information can be found in Appendix B. The dynamic model of the system was developed in Matlab Simulink using phasor quantities while the network topology was expressed using a matrix. The steady-state of the system can be initialised with power flow results. For more information regarding the modelling methodology, readers are advised to refer to [124]. For PVC, the proportional gain (K_1) and derivative gain (K_2) are the same as in Section 4.1. First order low-pass filters with a time constant of 0.1s are used for the differentiators.

4.2.2 Estimated Virtual Inertia from Point-of-load Voltage Control

The inertia contribution (H_L) from each cluster of domestic customers (CDC) can be estimated by using (4.10), for which the voltage profiles could be obtained through power

flow results. Readers can refer to Chapter 2 for load, power-voltage sensitivity (n_p) and voltage profiles for each CDC during winter and summer weekdays. The total virtual inertia coefficient (H_{TL}) from CDCs with PVC are calculated based on the load power rating as expressed in (4.12).

$$H_{TL} = \frac{\left(\sum_{i=1}^d S_{li} \cdot H_{Li} \right)}{\left(\sum_{i=1}^d S_{li} \right)} \quad (4.12)$$

The calculated inertia coefficients for winter/summer weekdays are shown in Fig. 4.3. Similar as in Chapter 2, three traces represent the upper boundary (95 pc), median value and lower boundary (5 pc) situation considering the variations from day to day. When K_2 is fixed, the variation of the total inertia in this case is determined by power-voltage sensitivity (n_p), voltage profiles and the ratio of domestic active power consumption. It can be seen that inertia value peaks during winter night hours due to the usage of electric heating while hits the bottom during similar sessions for summer when both the power consumption and power-voltage sensitivities for the domestic sector are low. It is shown in Fig. 4.3 that for most time of the day, an additional virtual inertia of around 1.3s can be provided. It should be mentioned that the inertia provided from PVC is lower than 2.5s due to the fact that active power-voltage sensitivities (n_p) of the domestic loads in the CIGRE network are mostly below 2 (ranging from 0.4 to 1.7).

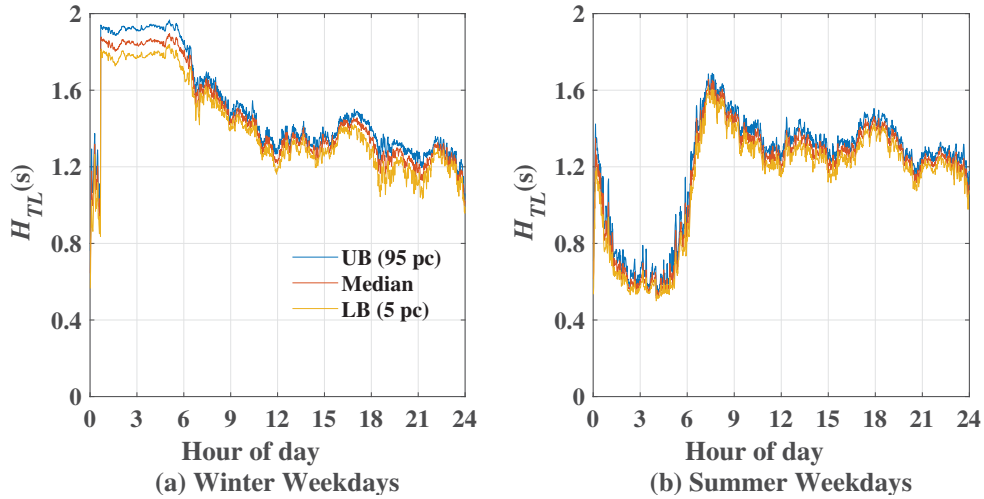


Fig. 4.3 Equivalent inertia for (a) winter weekdays and (b) summer weekdays

4.2.3 Time Domain Verification

At $t = 60$ s, 50% of the wind generation is suddenly disconnected to create a disturbance. The load demand and the power voltage sensitivity are based on the 7:30am data from winter weekdays and are assumed to be constant throughout the simulation. The frequency and load-side voltage response before and after the disturbance are given in Fig. 4.4. Compared to the case without any PVC (blue curve in Fig. 4.4 (a)), it can be seen that the RoCoF and frequency nadir of the case with PVC (red curve in Fig. 4.4 (a)) are both improved with acceptable load voltages (≥ 0.95 p.u.) as shown in Fig. 4.4 (b). The green trace denotes the case with PVC but setting K_2 to zero. Although the situation is much improved compared to the case without any PVC, it performs less well than the case with full design of PVC (red trace, $K_1 = 3.125$, $K_2 = 2.5$) which confirms the value of the differentiator.

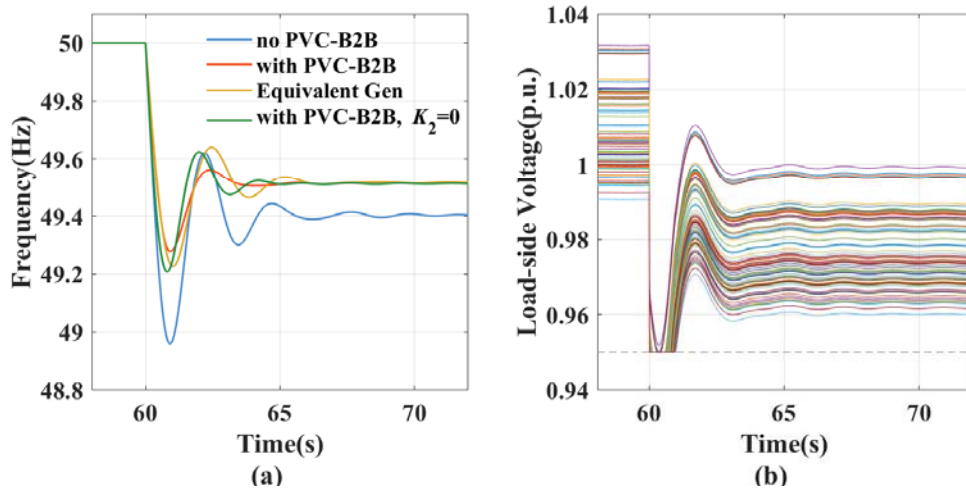


Fig. 4.4 (a) Frequency and (b) load-side voltage response before and after sudden disconnection of 50% of wind generation

To quantify the equivalent system inertia enhancement acquired from PVC, a case using generators with additional inertia of $\Delta H_{sys} = 0.53$ s and without using PVC is also provided in Fig. 4.4 (a) (marked in brown). It can be observed that during the dynamic process, the red trace (with PVC) and brown trace (equivalent generator with increased inertia) coincide at the very beginning, which indicates that the equivalent system inertia enhancement from PVC at the initial stage is around 0.53s. It should be mentioned that this $\Delta H_{sys} = 0.53$ s value is based on total generator rating. It would be around 1.4s if translated to the load power rating.

It should be noted that the equivalent system inertia increment of 1.4s is less than the estimated results as shown in Fig. 4.3 (a) at 7:30am (which is around 1.6s). This is due to the fact that some CDCs reach their lower voltage limit of 0.95 p.u. as shown in Fig. 4.4 (b). The saturation phenomenon lasts for around 0.9s as can be seen in Fig. 4.4 (b). Note that no inertia can be emulated from the demand side once its load voltage is saturated and fixed at 0.95 p.u. So during that 0.9s duration, the system total virtual inertia coefficient is lower than the estimation from (4.12) as some of the CDCs are saturated in voltage. In addition, the grid frequency settles to the steady-state value faster with PVC (red trace) in Fig. 4.4 (a) compared to the case with ‘Equivalent Gen’ (brown trace). The reason is that the virtual inertia contribution from PVC will recover to the estimated value once the load voltages are restored back within the voltage range. So the H_{TL} actually recovers back to be larger than 1.4s (‘Equivalent Gen case’) after the saturation, making the frequency settles quicker to the steady-state value.

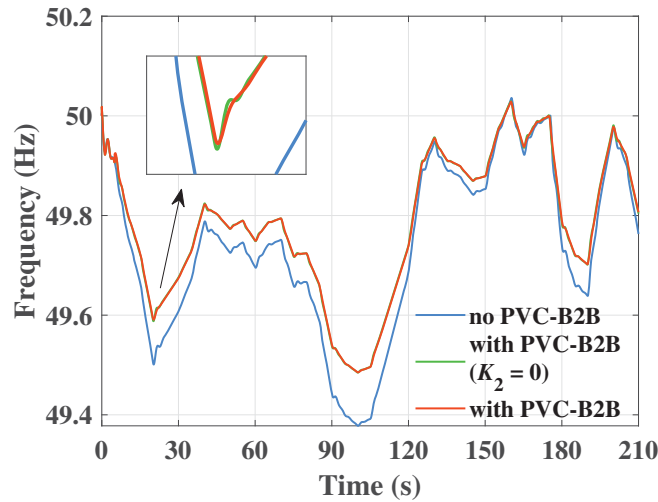


Fig. 4.5 Frequency response under wind fluctuations

The frequency response of the microgrid system under wind fluctuations is given in Fig. 4.5. The load damping effect from PVC (in proportion to frequency deviation Δf) can be easily observed, which contributes to the frequency excursion improvement by up to about 0.1Hz. It is to be pointed out that the case without virtual inertia support from PVC (green trace, $K_1 = 3.125, K_2 = 0$) almost coincides with the base case with PVC (red trace, $K_1 = 3.125, K_2 = 2.5$). This implies that only marginal virtual inertia can be achieved from PVC under wind power fluctuations as in such case, the RoCoF is not that significant compared with the case under sudden infeed power loss.

4.3 Conclusion

This chapter evaluates and quantifies virtual inertia from the demand side by using demand reduction (DR) from point-of-load voltage control (PVC). The virtual inertia and load damping coefficients of loads with PVC are derived. The effectiveness is verified through time domain simulation using a CIGRE benchmark micgrid system.

Under the control design following the UK National Grid frequency requirement, up to 2.5s of virtual inertia can be obtained from an impedance-type load with PVC ($n_p = 2$). The CIGRE benchmark microgrid with high-resolution domestic demand model demonstrates that PVC can provide around 1.3s of inertia (with respect to the load power rating) during most part of the day. The system equivalent inertia can be increased by $\Delta H_{sys} = 0.53s$ if all the loads within domestic sector in the system are equipped with PVC. The promising results indicate that the virtual inertia from PVC can play a significant role in complementing the declining inertial contribution from the supply side in future power grids.

Chapter 5

System Stability with Point-of-load Voltage Control for Voltage Regulation

As pointed out in Section 1.1, there is growing concern about the impact of increasing penetration of power electronic compensators (PECs) on the stability of power systems over a wide frequency range. Deployment of point-of-load voltage control (PVC) would drastically increase the penetration of PEC. It is therefore, crucial to analyse the stability implications of PVC which motivates this and the next chapter.

This chapter focuses on the stability analysis of a distribution network with multiple loads with PVC for voltage regulation. Unlike in the other chapters, PECs in this chapter provide reactive power compensation only and the configuration is a single voltage source converter connected in series with the loads with a capacitor on the DC-side (see Section 1.2.2). For simplicity, the loads equipped with PVC for reactive power compensation only is referred to as PVC-Q.

In this chapter, the vector control of PVC-Q is firstly reported which can be integrated in the stability model of distribution networks and microgrids with other DG inverters. (This work has been done by my colleague Dr Diptargha Chakravorty as part of a collaboration. He also contributed to the time domain models including the case with equivalent DG inverters.) Thereafter, linearised state-space model of the distribution network with vector controlled PVC-Q is developed using the Component Connection Method (CCM) [125] which can be easily scaled up to include more loads with PVC and DG inverters. Finally, the developed model is used to analyse the small signal stability of a distribution network with two PVC-Qs and compared against the stability with equivalent penetration of DG inverters. The analysis is presented for a range of scenarios covering low- to medium voltage (LV/MV) levels and

sparse rural to dense urban distribution networks. Although the test system considered for this study is simple, the framework can be extended for realistic systems.

It is to be noted that the work presented in this chapter is based on a single phase network and does not consider the switching model of the converters, voltage unbalance or harmonics and neglects the dynamics of the DC link of PVC-Q in state-space model.

5.1 Vector Control of an PVC-Q

The configuration of a PEC connected in series with a resistive-inductive (RL-type) load is shown in Fig. 5.1 [6]. The RL-type load is denoted by R_{nl} & L_{nl} and the corresponding voltage across it is given by V_{nl} . The injected series voltage V_c across the filter capacitance (C_f) is controlled to regulate the voltage (V_p) at the point of coupling (PoC). The equivalent inductance and resistance of rest of the network including other passive loads is denoted by L_1 and R_c , respectively. The source impedance is represented by the inductance L_g .

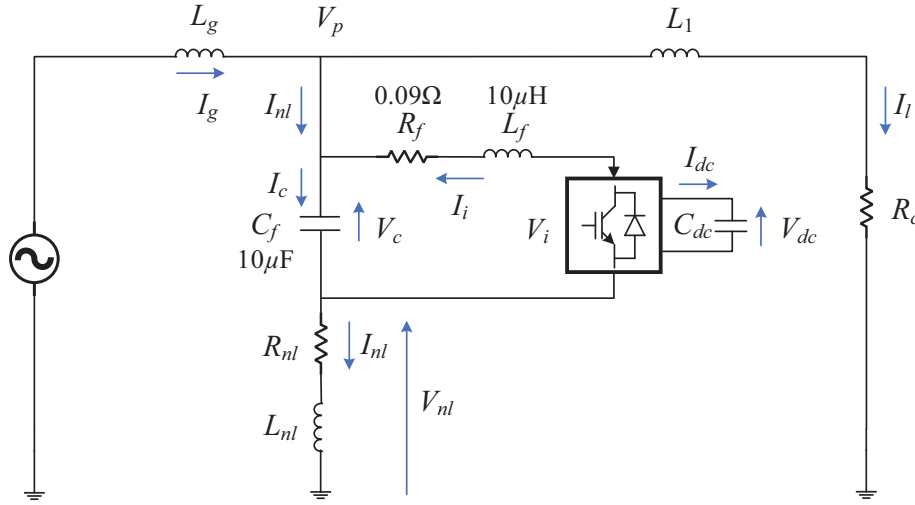


Fig. 5.1 PVC-Q configuration

5.1.1 Choice of Reference Frame (d -axis)

For regulating the point of coupling (PoC) voltage using vector control of the shunt connected inverters (such as DG inverter or STATCOM), the d -axis is normally aligned with the PoC voltage to achieve decoupled control. In this chapter, the focus is on PVC-Q which injects a voltage (V_c) across the filter capacitor in quadrature (lead or lag) with the load current (I_{nl}). In this case, aligning the d -axis with the PoC voltage (V_p) results in non-zero inverter

current (I_i) on both d and q axes as shown in Fig. 5.2.

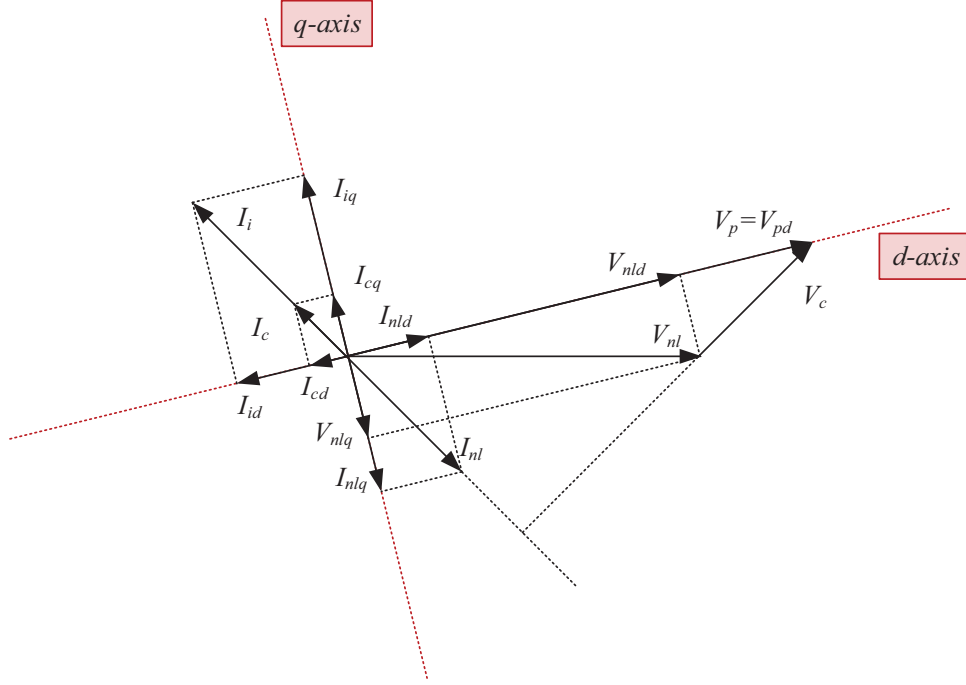


Fig. 5.2 Phasor diagram with d -axis aligned with PoC voltage

Thus, it is not possible to force the d -axis component of the inverter current to zero in order to ensure zero active power (neglecting filter and inverter losses) exchange in steady-state. To get around this problem, the d -axis could be aligned either with the filter capacitor voltage (V_c) or the load current (I_{nl}). The latter is ruled out due to the possible implementation challenges posed by high harmonic content in the load current. So the d -axis is aligned with the filter capacitor voltage (V_c) as shown Fig. 5.3.

This enables the d -axis control loop to maintain the DC link voltage V_{dc} while the q -axis loop can be used for regulating the PoC voltage (V_p) or the load voltage (V_{nl}). However, it is necessary to maintain a minimum filter capacitor voltage to allow satisfactory operation of PLL, as discussed later in Section 5.2.2. In Fig. 5.3, the filter capacitor voltage (V_c) leads the load current (I_{nl}) by 90° providing inductive compensation. The PVC can provide capacitive compensation if V_c is made to lag I_{nl} by 90° . The compensation mode depends on the polarity of V_c , unlike a STATCOM, where it is decided by the phase angle of the injected current with respect to the PoC voltage. For capacitive compensation, V_{cd} is aligned with -ve d -axis and I_{nlq} becomes slightly more than I_{iq} so that I_{cq} now aligns with -ve q -axis, thereby leading V_{cd} by 90° .

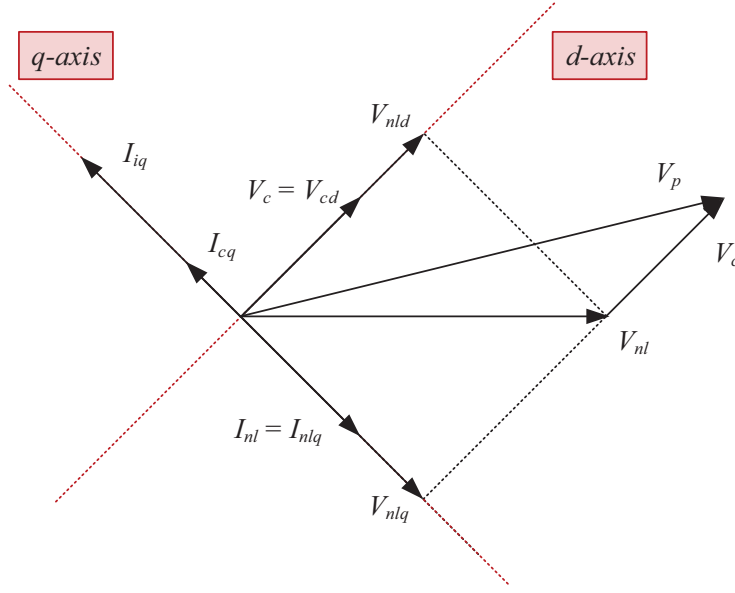


Fig. 5.3 Phasor diagram with d -axis aligned with filter capacitor voltage

5.1.2 Current Control Loop

The current control loop is designed based on the dynamics of the inverter current (I_i), filter capacitor voltage (V_c) and load current (I_{nl}) which can be represented in a synchronously rotating (dq) reference frame as follows [126]:

$$L_f \frac{dI_{id}}{dt} = V_{id} - V_{cd} - R_f I_{id} + \omega_0 L_f I_{iq} \quad (5.1)$$

$$L_f \frac{dI_{iq}}{dt} = V_{iq} - V_{cq} - R_f I_{iq} - \omega_0 L_f I_{id} \quad (5.2)$$

$$C_f \frac{dV_{cd}}{dt} = I_{nld} + I_{id} + \omega_0 C_f V_{cq} \quad (5.3)$$

$$C_f \frac{dV_{cq}}{dt} = I_{nlq} + I_{iq} - \omega_0 C_f V_{cd} \quad (5.4)$$

$$L_{nl} \frac{dI_{nld}}{dt} = V_{pd} - V_{cd} - R_{nl} I_{nld} + \omega_0 L_{nl} I_{nlq} \quad (5.5)$$

$$L_{nl} \frac{dI_{nlq}}{dt} = V_{pq} - V_{cq} - R_{nl} I_{nlq} - \omega_0 L_{nl} I_{nld} \quad (5.6)$$

The current flowing out of the inverter (I_i) is assumed to be positive. Considering I_{id} & I_{iq} as state variables, V_{id} & V_{iq} as control inputs and V_{cd} & V_{cq} are the disturbance inputs, the current control loop is designed following the standard method outlined in [126]. The closed loop time constant (τ) is chosen to be 0.1ms to achieve a fast enough response while

ensuring that the controller bandwidth ($\frac{1}{\tau}$) is at least 10 times smaller than the switching frequency. Note that MOSFETs are preferred in such single phase PVC application with high-frequency operation, wide load variations, low-voltage and lower output power.

5.1.3 Point of Coupling Voltage Control Loop

The inverter current references (I_{idref} & I_{iqref}) are obtained from the voltage control loop described here. An approximate small-signal model for PoC voltage dynamics is presented first based on Fig. 5.1. The feeder resistance is neglected for simplicity in tuning the PoC control loop. The d -axis component of the source current can be expressed as $I_{gd} \approx I_{ld}$ (as the d -axis load current component $I_{nld} \approx 0$) while the q -axis current is given by $I_{gq} = I_{lq} + I_{nlq}$. Assuming an ideal PLL, the PoC voltage along d -axis is given by (5.7), where the first two terms represent the *load effect* and the last term shows the *control effect*. As the current through the filter capacitor is negligibly small, an incremental change in load current is almost equal to a change in the inverter current, i.e. $\Delta I_{nlq} \approx -\Delta I_{iq}$. Hence, the second term is considered as *control effect*.

$$\Delta V_{pd} = L_g \frac{d\Delta I_{ld}}{dt} - L_g \omega_0 \Delta I_{lq} - L_g \omega_0 \Delta I_{nlq} \quad (5.7)$$

Similarly, the q -axis component of the PoC voltage can be given by (5.8) which shows that ΔV_{pq} depends on the rate of change of the load current.

$$\begin{aligned} \Delta V_{pq} &= L_g \frac{d\Delta I_{gq}}{dt} + L_g \omega_0 \Delta I_{gd} \\ &= L_g \frac{d\Delta I_{lq}}{dt} + L_g \omega_0 \Delta I_{ld} + L_g \frac{\Delta I_{nlq}}{dt} \end{aligned} \quad (5.8)$$

The voltage control loop is typically much slower than the current control loop. Hence the rate of change of small deviation in the load current ($\frac{d\Delta I_{nlq}}{dt}$) is quite small such that the effect of the small change in control variable ΔI_{iq} can be neglected in case of ΔV_{pq} . Therefore, the control loop for the PoC voltage regulation can be represented as in Fig. 5.4. The feeder voltage references are adjusted using droop if there are multiple PVC-Qs along the feeder. The current controller shown in Fig. 5.4 is a simple representation neglecting the feed forward and decoupling terms.

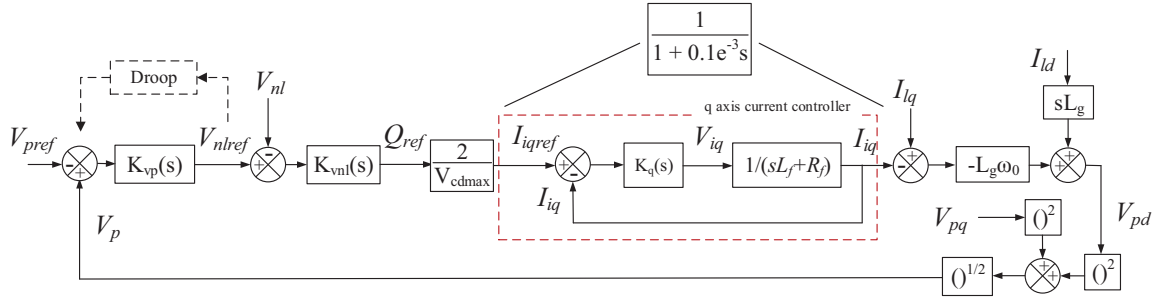


Fig. 5.4 PoC voltage control scheme

The compensator (K_{vp}) for the PoC voltage regulation is a proportional-integral (PI) controller with $k_{pvp} = 100$ and $k_{ivp} = 4$. The source inductance is $L_g = 0.0011\text{H}$ which includes the transformer leakage and network inductance. A conservative phase margin of 90° is kept to ensure robustness in the face of varying source impedance and account for the unmodelled dynamics of the filter, loads and PLL. The bode plot of the open loop of PoC voltage control is shown in Fig. 5.5 with the corresponding gain crossover frequency (ω_c) and the phase margin highlighted. A step response of the closed loop system is also given which indicates the settling time is about 0.22s.

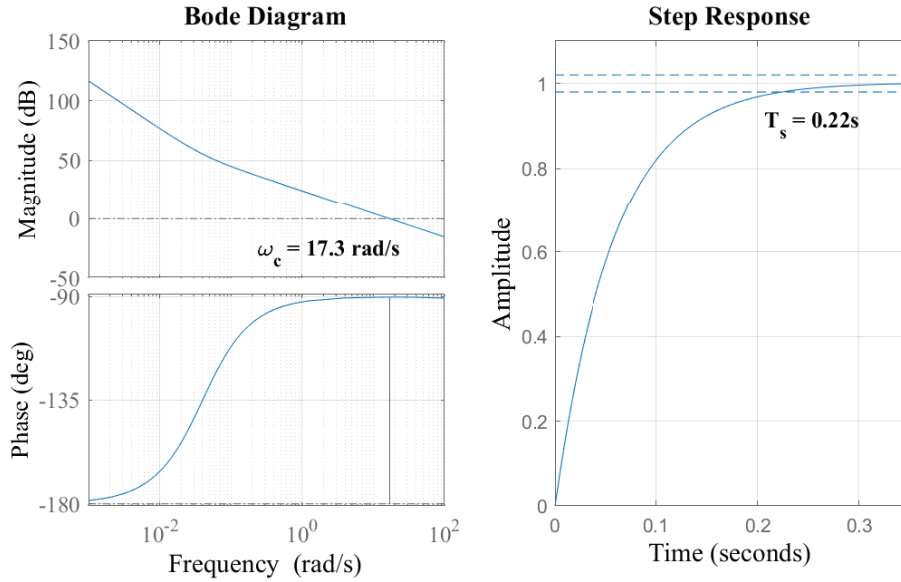


Fig. 5.5 Bode plot and step response of the PoC voltage control loop

5.1.4 Phase-Locked Loop

For the single-phase PLL considered here, an additional fictitious phase was created by introducing a phase delay of $\frac{1}{4}$ of a fundamental cycle. A range of different PLL configurations have been reported [127]. However, in stability studies, the dynamics of PLL is either completely neglected [128], or simplified by a proportional-integral (PI) controller [129], [130]. For a PI representation of a PLL, the tuning of k_p and k_i has little effect on the overall phase margin in the low frequency range which prompted us to adopt PI based PLL in this study. The compensator gains are chosen as $k_p = 0.3$ and $k_i = 0.5$ to allow adequate gain and phase margins at low frequencies.

5.1.5 DC Link Control Loop

The DC link control loop is designed following the standard procedure [126]. A proportional-integral compensator is used with gains $k_{pdc} = -2C_{dc}\zeta\omega$ and $k_{idc} = -C_{dc}\omega^2$, where the DC link capacitor $C_{dc} = 1.5\text{mF}$, $\zeta = 0.707$ and $\omega = 24.16\text{rad/s}$.

5.1.6 Performance Validation

The performance of the voltage control loop is tested using the system shown in Fig. 5.6, modelled in Matlab Simulink. The simulation model uses an average model for the converter based on a controlled voltage source on the AC side and a controlled current source on the DC side. Switching action within the converter is not modelled explicitly. The dynamics of the AC and the DC side are coupled through the ideal power balance equation i.e. $P_{ac} = P_{dc}$. A 1.8 kVA resistive load R_{new} is inserted to reduce the PoC voltage by approximately 5 V. The transformer and the feeder parameters taken from [88] correspond to typical figures for distribution networks in the UK. The R/X ratio of the lines is 4.26 (line type D in [88]) and the transformer is rated at 200 kVA.

PVC with reactive compensation does not exchange any active power between the ac and the dc side of the converter (except for supplying filter losses). To ensure this condition, the filter voltage (V_c) and the load current (I_{nl}) always maintains a quadrature relationship. The choice of mode of operation depends on the system requirement. In case of under voltage disturbance, the PVC switches from inductive to capacitive mode to provide voltage support. From the phasor diagram in Fig. 5.3, it is evident that in the inductive mode of operation V_{cd} is aligned with the $+d$ -axis and the load current I_{nlq} is aligned with the $-q$ -axis. In order to switch to the capacitive mode, V_{cd} needs to realign with the $-d$ -axis. To enable this

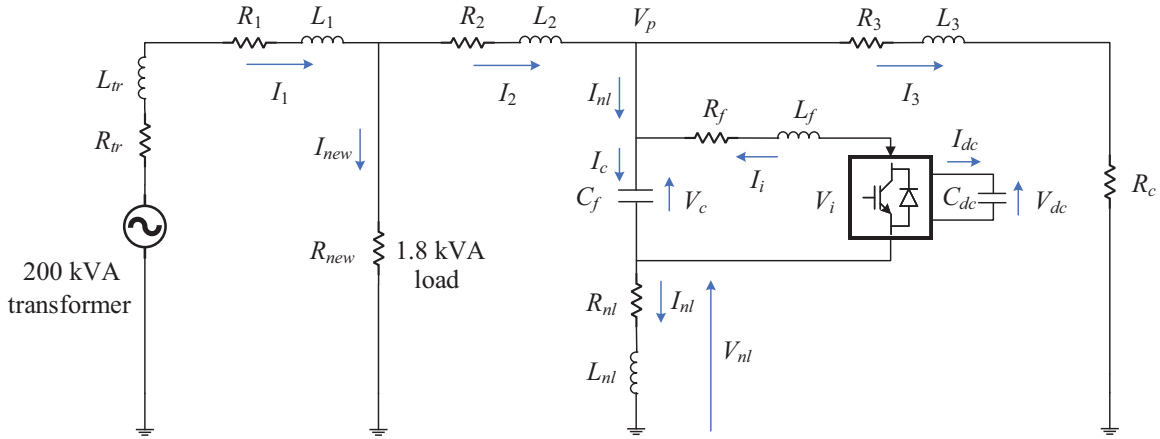


Fig. 5.6 Test system for validation of PoC voltage controller

transition process, the PEC outputs a zero voltage for 3 cycles after a disturbance.

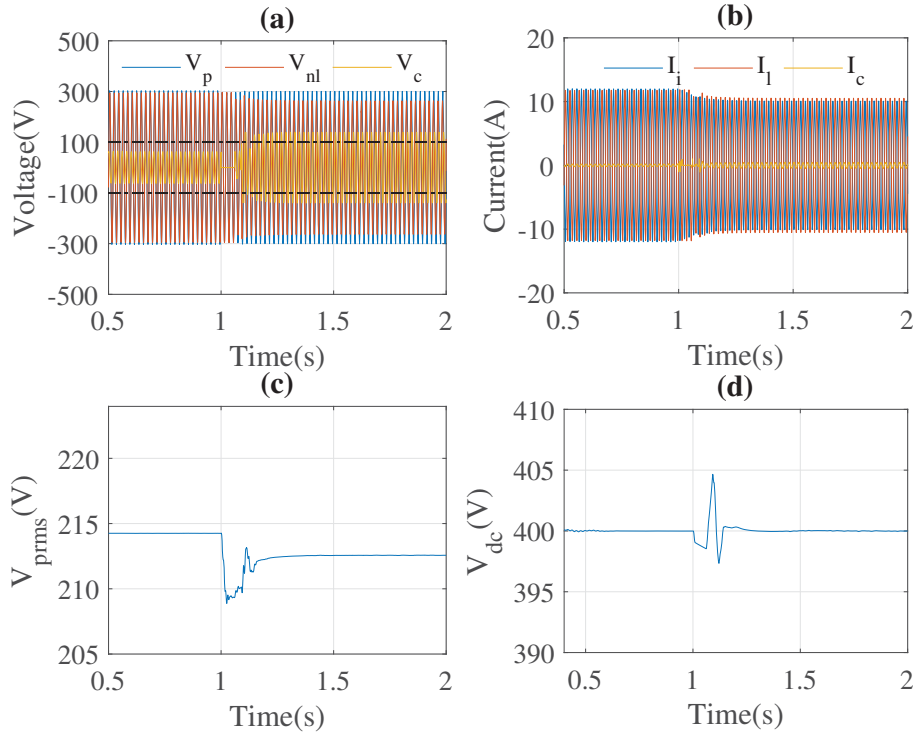


Fig. 5.7 Dynamic response of (a) PoC, load and injected voltages; (b) inverter, load and filter capacitor current; (c) RMS value of PoC voltage and (d) DC link voltage

Fig. 5.7 shows the dynamic response following reduction in PoC voltage at $t = 1$ s. The compensator switches from inductive mode (I_{nl} lagging V_c by 90°) to capacitive mode (I_{nl} leading V_c by 90°) by making the inverter current (I_i) slightly less than the load current (I_{nl})

such that the filter capacitor current (I_c) now aligns with the negative q -axis. This operation can be better understood from the phasor diagram in Fig. 5.3.

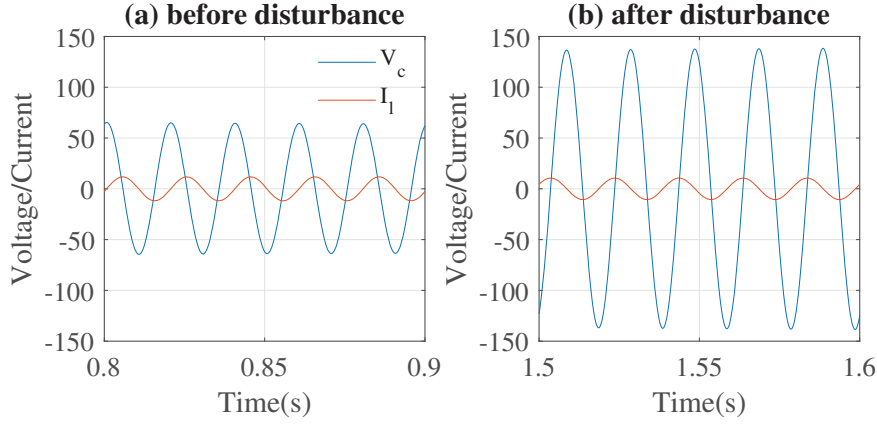


Fig. 5.8 Injected voltage (V_c) and load current (I_{nl}) (a) before the disturbance (inductive mode) and (b) after the disturbance (capacitive mode)

Fig. 5.8 (a) shows that I_{nl} lags V_c by 90° i.e. the compensator works in inductive mode before the disturbance while after the disturbance it switches to capacitive mode where I_{nl} leads V_c by 90° (Fig. 5.8 (b)).

From Fig. 5.7 (c), it is clear that the PoC voltage could not be regulated at its pre-disturbance level due to violation of the inverter current limit which is set according to the allowable voltage variation across the load [62]. This limit for V_{nl} is fixed at ± 0.1 p.u. in this particular case. Deviation in DC bus voltage after the disturbance, seen in Fig. 5.7 (d), is caused by additional losses in the filter resistor (R_f) due to change in I_i .

5.2 Linearised State Space Model of an PVC-Q

The linearised state-space model (SSM) of a distribution network with PVC-Q is developed here. First, the SSM is developed separately for the following sub-systems (a) PLL (b) PoC voltage control loop (c) current control loop (d) filter and (e) network and loads. Then, the Component Connection Method (CCM) [125] is used to obtain the overall SSM. For simplicity, only resistive loads are considered and the DC link dynamics is neglected.

5.2.1 Phase-Locked Loop

The PI compensator based single phase PLL has one state variable associated with the compensator (Δx_1) and another one corresponding to the integrator ($\Delta\theta$). The input and output variables are ΔV_{cq} and $\Delta\omega$, $\Delta\theta$ where ΔV_{cq} denotes the incremental change in q -axis component of the filter voltage, $\Delta\omega$ denotes the change in PLL frequency and $\Delta\theta$ represents the change in PLL angle. The SSM of PLL is given by (5.9) and (5.10) where k_p and k_i are proportional and integral gains, respectively.

$$\begin{bmatrix} \Delta \dot{x}_1 \\ \Delta \dot{\theta} \end{bmatrix} = \begin{bmatrix} 0 & 0 \\ k_i & 0 \end{bmatrix} \begin{bmatrix} \Delta x_1 \\ \Delta \theta \end{bmatrix} + \begin{bmatrix} 1 \\ k_p \end{bmatrix} [\Delta V_{cq}] \quad (5.9)$$

$$\begin{bmatrix} \Delta \omega \\ \Delta \theta \end{bmatrix} = \begin{bmatrix} k_i & 0 \\ 0 & 1 \end{bmatrix} \begin{bmatrix} \Delta x_1 \\ \Delta \theta \end{bmatrix} + \begin{bmatrix} k_p \\ 0 \end{bmatrix} [\Delta V_{cq}] \quad (5.10)$$

5.2.2 Point of Coupling Voltage Control Loop

The block diagram of the voltage control loop is shown in Fig. 5.9 which is divided into: outer PI controller (Fig. 5.9 (a)) and inner integral controller (Fig. 5.9 (b)). The state variable associated with the outer loop is denoted by Δx_{21} . The input signal V_{pmag} is the measured PoC voltage which can be expressed in terms of dq -components as $\sqrt{V_{pd}^2 + V_{pq}^2}$. This non-linear term has been linearised about a stable operating point V_{pmag0} which results in $(\frac{V_{pd0}}{V_{pmag0}} \Delta V_{pd})$ for an incremental change in d -axis component. Similar expression can be obtained for an incremental change in the q -axis component. Thus, the SSM of the outer loop (Fig. 5.9 (a)) is given by (5.11) and (5.12). k_{pv} and k_{iv} are the proportional and integral gains of the voltage control loop compensator, respectively. In Fig. 5.9 (a) the symbol for the sum is considered $-V_{pmagref} + V_{pmag}$ based on the operating principle of PVC. An increase in PoC voltage magnitude (due to disturbance) results in a positive error thus increasing the voltage reference set point across the load (V_{nlref}). This way the power consumption (both active and reactive in case of non-unity power factor load) of the load increases to regulate the PoC voltage back to its reference value.

$$\begin{bmatrix} \Delta \dot{x}_{21} \end{bmatrix} = \begin{bmatrix} 0 \end{bmatrix} \begin{bmatrix} \Delta x_{21} \end{bmatrix} + \begin{bmatrix} \frac{V_{pd0}}{V_{pmag0}} & \frac{V_{pq0}}{V_{pmag0}} \end{bmatrix} \begin{bmatrix} \Delta V_{pd} \\ \Delta V_{pq} \end{bmatrix} \quad (5.11)$$

$$\begin{bmatrix} \Delta V_{nlref} \end{bmatrix} = \begin{bmatrix} k_{iv} \end{bmatrix} \begin{bmatrix} \Delta x_{21} \end{bmatrix} + \begin{bmatrix} \frac{k_{pv} V_{pd0}}{V_{pmag0}} & \frac{k_{pv} V_{pq0}}{V_{pmag0}} \end{bmatrix} \begin{bmatrix} \Delta V_{pd} \\ \Delta V_{pq} \end{bmatrix} \quad (5.12)$$

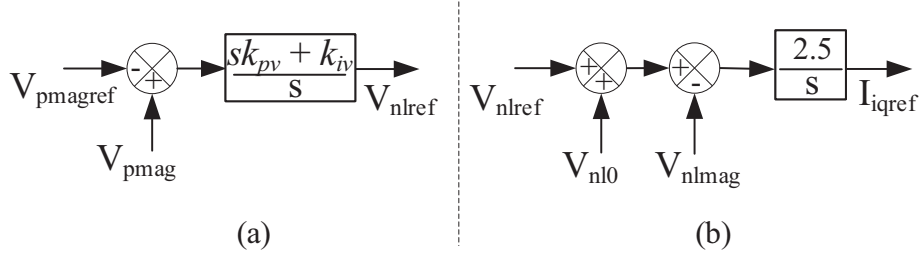


Fig. 5.9 Block diagram of (a) PoC and (b) load voltage control loops

The state variable associated with the inner loop is denoted by Δx_{22} . The outer loop sets the reference for the inner loop which is updated by the maximum load voltage V_{nl0} , (i.e. minimum voltage across the filter capacitor) corresponding to the operating point V_{pmag0} . A minimum voltage is required across the filter capacitor to ensure satisfactory operation of the PLL. The minimum filter capacitor voltage is considered to be 50 V here. The tuning of the PLL is carried out considering this minimum voltage. The choice of 50V is prompted by the fact that a sufficiently high value would ease the tuning of the PLL parameters to achieve an acceptable dynamic response. However, in practice this minimum filter voltage can be well below 50V depending on the type of PLL and the tuning of its compensator.

For a resistive load, $V_{nl0} = \sqrt{V_{pmag0}^2 - 50^2}$ which is linearised as before and is expressed as $\frac{V_{pd0}}{\sqrt{V_{pmag0}^2 - 50^2}} \Delta V_{pd}$ for an incremental change in d -axis component. Similar expression can be obtained for an incremental change in the q -axis component. The load voltage magnitude feedback term V_{nlmag} is also linearised in a similar way around V_{nlmag0} . The SSM of the inner loop (Fig. 5.9 (b)) is given by (5.13) and (5.14). In (5.14) (and other equations henceforth), zero in bold letter denote a matrix of appropriate dimension.

$$\begin{bmatrix} \Delta \dot{x}_{22} \end{bmatrix} = \begin{bmatrix} 0 \end{bmatrix} \begin{bmatrix} \Delta x_{22} \end{bmatrix} + \begin{bmatrix} 1 \\ \frac{-V_{nld0}}{V_{nlmag0}} \\ \frac{-V_{nlq0}}{V_{nlmag0}} \\ \frac{V_{pd0}}{\sqrt{V_{pmag0}^2 - 50^2}} \\ \frac{V_{pq0}}{\sqrt{V_{pmag0}^2 - 50^2}} \end{bmatrix}^T \begin{bmatrix} \Delta V_{nlref} \\ \Delta V_{nld} \\ \Delta V_{nlq} \\ \Delta V_{pd} \\ \Delta V_{pq} \end{bmatrix} \quad (5.13)$$

$$\begin{bmatrix} \Delta I_{iqref} \end{bmatrix} = \begin{bmatrix} 2.5 \end{bmatrix} \begin{bmatrix} \Delta x_{22} \end{bmatrix} + \begin{bmatrix} 0 \end{bmatrix} \begin{bmatrix} \Delta V_{nlref} \\ \Delta V_{nld} \\ \Delta V_{nlq} \\ \Delta V_{pd} \\ \Delta V_{pq} \end{bmatrix} \quad (5.14)$$

5.2.3 Current Control Loop

The structure of the current control loop adopted here is standard for any PEC. The state variables associated with the PI controllers in d and q axis loops are denoted by $\Delta \gamma_d$ and $\Delta \gamma_q$, respectively and the controller gains (same for d and q axis loops) are k_{pc} and k_{ic} . The SSM of the current controller is given by (5.15) and (5.16). The incremental changes in the current control loop reference values are denoted by ΔI_{idref} & ΔI_{iqref} while the change in the inverter currents and filter voltages are expressed as ΔI_{id} & ΔI_{iq} and ΔV_{cd} & ΔV_{cq} , respectively.

$$\begin{bmatrix} \Delta \dot{\gamma}_d \\ \Delta \dot{\gamma}_q \end{bmatrix} = \begin{bmatrix} 0 \end{bmatrix} \begin{bmatrix} \Delta \gamma_d \\ \Delta \gamma_q \end{bmatrix} + \begin{bmatrix} 1 & 0 \\ 0 & 1 \\ -1 & 0 \\ 0 & -1 \\ 0 & 0 \\ 0 & 0 \end{bmatrix}^T \begin{bmatrix} \Delta I_{idref} \\ \Delta I_{iqref} \\ \Delta I_{id} \\ \Delta I_{iq} \\ \Delta V_{cd} \\ \Delta V_{cq} \end{bmatrix} \quad (5.15)$$

$$\begin{aligned}
\begin{bmatrix} \Delta V_{id} \\ \Delta V_{iq} \end{bmatrix} &= \begin{bmatrix} k_{ic} & 0 \\ 0 & k_{ic} \end{bmatrix} \begin{bmatrix} \Delta \gamma_d \\ \Delta \gamma_q \end{bmatrix} \\
&+ \begin{bmatrix} k_{pc} & 0 \\ 0 & k_{pc} \\ -k_{pc} & \omega_0 L_f \\ -\omega_0 L_f & -k_{pc} \\ 1 & 0 \\ 0 & 1 \end{bmatrix}^T \begin{bmatrix} \Delta I_{idref} \\ \Delta I_{iqref} \\ \Delta I_{id} \\ \Delta I_{iq} \\ \Delta V_{cd} \\ \Delta V_{cq} \end{bmatrix}
\end{aligned} \tag{5.16}$$

5.2.4 Filter

The SSM of the filter part of the PEC can be obtained from the dynamics of the inverter current (I_i) and filter capacitor voltage (V_c) given by (5.1), (5.2), (5.3) and (5.4). The state variables are the d - and q - axis components of the inverter current (I_{id} , I_{iq}) and the filter capacitor voltage (V_{cd} , V_{cq}). The equations are linearised around I_{id0} , V_{cd0} (and similarly for the q - axis) to derive the SSM of the filter as in (5.17) and (5.18). The filter resistance, inductance and capacitance are given by R_f , L_f and C_f , the load resistance is given by R_{nl} and ω_0 denotes the nominal frequency of the network.

$$\begin{aligned}
\begin{bmatrix} \Delta \dot{I}_{id} \\ \Delta \dot{I}_{iq} \\ \Delta \dot{V}_{cd} \\ \Delta \dot{V}_{cq} \end{bmatrix} &= \begin{bmatrix} -\frac{R_f}{L_f} & \omega_0 & -\frac{1}{L_f} & 0 \\ -\omega_0 & -\frac{R_f}{L_f} & 0 & -\frac{1}{L_f} \\ \frac{1}{C_f} & 0 & 0 & \omega_0 \\ 0 & \frac{1}{C_f} & -\omega_0 & 0 \end{bmatrix} \begin{bmatrix} \Delta I_{id} \\ \Delta I_{iq} \\ \Delta V_{cd} \\ \Delta V_{cq} \end{bmatrix} \\
&+ \begin{bmatrix} I_{iq0} & \frac{1}{L_f} & 0 & 0 & 0 \\ -I_{id0} & 0 & \frac{1}{L_f} & 0 & 0 \\ V_{cq0} & 0 & 0 & \frac{1}{C_f R_{nl}} & 0 \\ -V_{cd0} & 0 & 0 & 0 & \frac{1}{C_f R_{nl}} \end{bmatrix} \begin{bmatrix} \Delta \omega \\ \Delta V_{id} \\ \Delta V_{iq} \\ \Delta V_{nld} \\ \Delta V_{nlq} \end{bmatrix}
\end{aligned} \tag{5.17}$$

$$\begin{bmatrix} \Delta I_{id} \\ \Delta I_{iq} \\ \Delta V_{cd} \\ \Delta V_{cq} \end{bmatrix} = \begin{bmatrix} 1 & 0 & 0 & 0 \\ 0 & 1 & 0 & 0 \\ 0 & 0 & 1 & 0 \\ 0 & 0 & 0 & 1 \end{bmatrix} \begin{bmatrix} \Delta I_{id} \\ \Delta I_{iq} \\ \Delta V_{cd} \\ \Delta V_{cq} \end{bmatrix} + \begin{bmatrix} 0 \\ 0 \\ 0 \\ 0 \end{bmatrix} + \begin{bmatrix} \Delta \omega \\ \Delta V_{id} \\ \Delta V_{iq} \\ \Delta V_{nld} \\ \Delta V_{nlq} \end{bmatrix} \quad (5.18)$$

5.2.5 Network and Loads

The simple network shown in Fig. 5.6 with three segments and an PVC-Q is considered here. The load R_{new} used for creating disturbance is modelled as a current source I_s with a high resistance (R_{high}) in parallel. The transformer impedance (R_{tr} and L_{tr}) is merged within R_1 and L_1 in (5.19) and (5.20). The line resistance R_3 is merged with the equivalent load (R_c) while the inductance L_3 is neglected. The state variables are the d - and q - axis components of the line currents flowing through L_1 and L_2 . The SSM of the network and the load is given by (5.23) and (5.24) with A_{line} , B_{line} , C_{line} and D_{line} expressed as in (5.19), (5.20), (5.21) and (5.22). The incremental change in the source voltage (and the disturbance current) is denoted by ΔV_{sd} & ΔV_{sq} (ΔI_{sd} & ΔI_{sq}).

$$A_{line} = \begin{bmatrix} -\frac{R_1+R_{high}}{L_1} & \omega_0 & \frac{R_{high}}{L_1} & 0 \\ -\omega_0 & -\frac{R_1+R_{high}}{L_1} & 0 & \frac{R_{high}}{L_1} \\ \frac{R_{high}}{L_2} & 0 & -\frac{1}{L_2}(R_2 + R_{high} + \frac{R_{nl}R_c}{R_{nl}+R_c}) & \omega_0 \\ 0 & \frac{R_{high}}{L_2} & -\omega_0 & -\frac{1}{L_2}(R_2 + R_{high} + \frac{R_{nl}R_c}{R_{nl}+R_c}) \end{bmatrix} \quad (5.19)$$

$$B_{line} = \begin{bmatrix} I_{L1q0} & \frac{1}{L_1} & 0 & -\frac{R_{high}}{L_1} & 0 & 0 & 0 \\ -I_{L1d0} & 0 & \frac{1}{L_1} & 0 & -\frac{R_{high}}{L_1} & 0 & 0 \\ I_{L2q0} & 0 & 0 & \frac{R_{high}}{L_2} & 0 & -\frac{1}{L_2} \frac{R_c}{R_c+R_{nl}} & 0 \\ -I_{L2d0} & 0 & 0 & 0 & \frac{R_{high}}{L_2} & 0 & -\frac{1}{L_2} \frac{R_c}{R_c+R_{nl}} \end{bmatrix} \quad (5.20)$$

$$C_{line} = \begin{bmatrix} 1 & 0 & 0 & 0 \\ 0 & 1 & 0 & 0 \\ 0 & 0 & 1 & 0 \\ 0 & 0 & 0 & 1 \\ 0 & 0 & \frac{R_c}{R_c + R_{nl}} & 0 \\ 0 & 0 & 0 & \frac{R_c}{R_c + R_{nl}} \end{bmatrix} \quad (5.21)$$

$$D_{line} = \begin{bmatrix} 0 & 0 & 0 & 0 & 0 & 0 \\ 0 & 0 & 0 & 0 & 0 & 0 \\ 0 & 0 & 0 & 0 & 0 & 0 \\ 0 & 0 & 0 & 0 & 0 & 0 \\ 0 & 0 & 0 & 0 & -\frac{1}{R_c + R_{nl}} & 0 \\ 0 & 0 & 0 & 0 & 0 & -\frac{1}{R_c + R_{nl}} \end{bmatrix} \quad (5.22)$$

$$\begin{bmatrix} \Delta \dot{I}_{L1d} \\ \Delta \dot{I}_{L1q} \\ \Delta \dot{I}_{L2d} \\ \Delta \dot{I}_{L2q} \end{bmatrix} = A_{line} \begin{bmatrix} \Delta I_{L1d} \\ \Delta I_{L1q} \\ \Delta I_{L2d} \\ \Delta I_{L2q} \end{bmatrix} + B_{line} \begin{bmatrix} \Delta \omega \\ \Delta V_{sd} \\ \Delta V_{sq} \\ \Delta I_{sd} \\ \Delta I_{sq} \\ \Delta V_{cd} \\ \Delta V_{cq} \end{bmatrix} \quad (5.23)$$

$$\begin{bmatrix} \Delta I_{L1d} \\ \Delta I_{L1q} \\ \Delta I_{L2d} \\ \Delta I_{L2q} \\ \Delta I_{nld} \\ \Delta I_{nlq} \end{bmatrix} = C_{line} \begin{bmatrix} \Delta I_{L1d} \\ \Delta I_{L1q} \\ \Delta I_{L2d} \\ \Delta I_{L2q} \end{bmatrix} + D_{line} \begin{bmatrix} \Delta \omega \\ \Delta V_{sd} \\ \Delta V_{sq} \\ \Delta I_{sd} \\ \Delta I_{sq} \\ \Delta V_{cd} \\ \Delta V_{cq} \end{bmatrix} \quad (5.24)$$

Once the SSM is developed for the individual sub-systems (5.9) – (5.22), their A , B , C , D matrices are arranged together to form block-diagonal matrices. As an example, for

four sub-systems, a block-diagonal state matrix $A = \text{diag}(A_1, A_2, A_3, A_4)$ is formed (and similarly for B, C, D matrices). Further, a matrix L_T is formed to capture the algebraic relationship between the inputs and outputs of all the subsystems. Finally, the state matrix of the whole system (F) is computed as (5.25). More details of this CCM can be found in [125].

$$F = A + BL_T(I - DL_T)C^{-1} \quad (5.25)$$

The SSM for a simple network with one PVC-Q can be easily scaled up to include any number of network segments and PVC-Qs using CCM by simply repeating the equations for individual sub-systems. This is used for the study case discussed next in Section 5.3 where four network segments and two PVC-Qs are considered, as shown in Fig. 5.11.

Presence of more than one converter requires that all the variables are expressed in a common reference frame. This is achieved by the frame transformation method provided in [131]. As an example, the filter voltage V_c can be expressed on a common reference frame ‘ DQ ’ according to (5.26), where T_S and T_C are the transformation matrices given by (5.27) & (5.28) and $\Delta\delta$ is the incremental change in the phase angle difference between the reference frame of the respective inverter and the common reference frame ‘ DQ ’. In (5.27) & (5.28), V_{cd0} , V_{cq0} & δ_0 represent the corresponding values at a stable operating point.

$$\begin{bmatrix} \Delta V_{cD} \\ \Delta V_{cQ} \end{bmatrix} = T_S \begin{bmatrix} \Delta V_{cd} \\ \Delta V_{cq} \end{bmatrix} + T_C \begin{bmatrix} \Delta\delta \end{bmatrix} \quad (5.26)$$

$$T_S = \begin{bmatrix} \cos(\delta_0) & -\sin(\delta_0) \\ \sin(\delta_0) & \cos(\delta_0) \end{bmatrix} \quad (5.27)$$

$$T_C = \begin{bmatrix} -V_{cd0}\sin(\delta_0) - V_{cq0}\cos(\delta_0) \\ V_{cd0}\cos(\delta_0) - V_{cq0}\sin(\delta_0) \end{bmatrix} \quad (5.28)$$

5.2.6 Validation of Linearised State Space Model

The developed SSM is validated by comparing the dynamic response of the state variables with respect to that of the non-linear model developed in Matlab Simulink. At $t = 1\text{sec}$, a 100 W disturbance was introduced through R_{new} (Fig. 5.6) for 3 cycles. Fig. 5.10 shows

the comparison for six state variables associated with the filter capacitor and the network inductances. The responses match closely confirming the validity of the SSM.

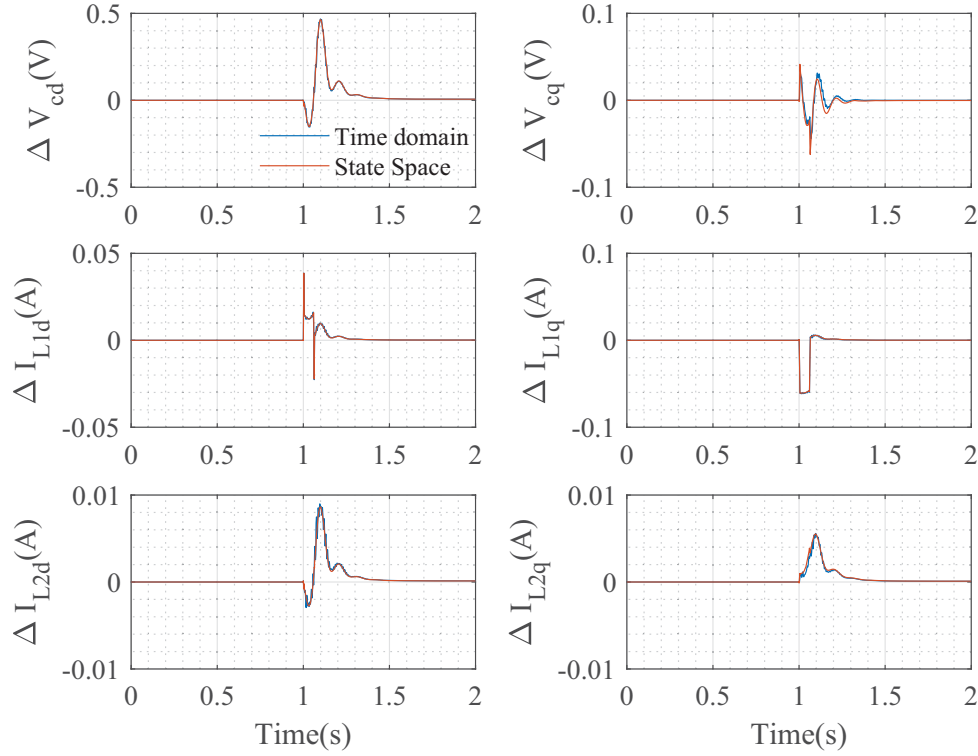


Fig. 5.10 Comparison of dynamic response of state variables in linearised state space model and non-linear model due to a small disturbance

5.3 Frequency Domain Analysis

The modelling framework discussed in Section 5.2 is used to obtain the SSM of the study system shown in Fig. 5.11. The dq -frame corresponding to the first PVC-Q is considered to be the common frame and all other quantities are referred to this using the previously discussed transformation technique (5.26), (5.27) & (5.28).

Eigen value analysis of the state matrix (5.25) of the study system shown in Fig. 5.11 confirms that there are 32 state variables. There are two high-frequency modes of 472.31 Hz & 369.63 Hz with a damping ratio of 87.3% & 91.6% respectively as well as a third mode (56.07 Hz, damping ratio : 99.6%) close to the fundamental frequency. Participation factor analysis reveals that the filter capacitor voltage of both PVC-Qs (V_{c1} & V_{c2}) and the current through the network segment 1 (I_{L1}) and 2 (I_{L2}) have dominant participation in the two high-

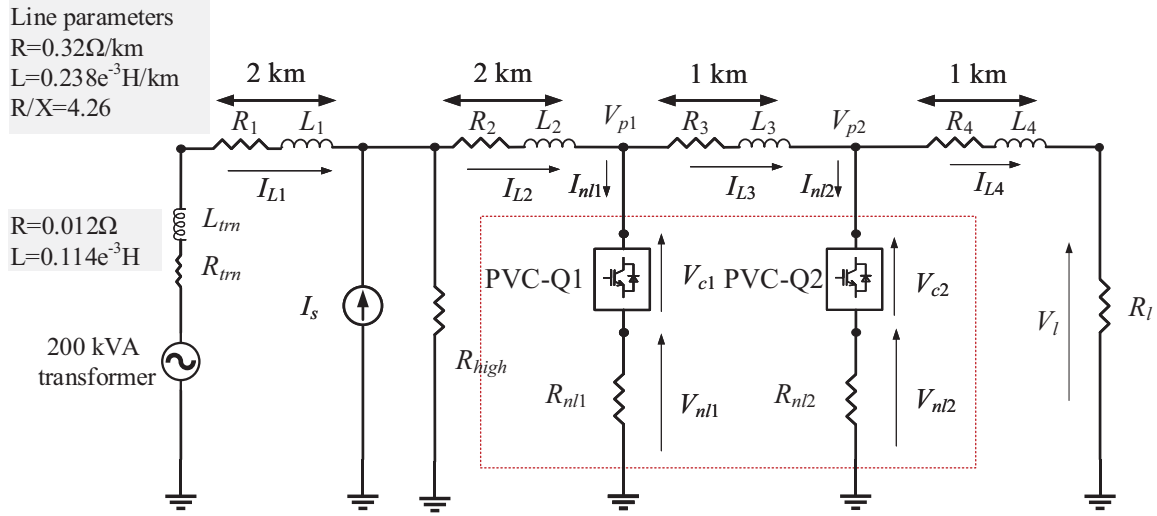


Fig. 5.11 Study system with two PVC-Qs used for frequency-domain analysis

frequency modes (472.31 Hz & 369.63 Hz) while the 56.07 Hz mode is mainly associated with the filter capacitor voltage.

Varying the network parameters, such as the length of the line segments and R/X ratio, over a certain range shows movement of the critical system modes obtained from the eigen values of the system state matrix. This study helps to ascertain the overall small signal stability of the system under different scenarios. Although the study system shown in Fig. 5.11 is simple, varying the length of line segments 1, 2 and 3 and the R/X ratios cover a wide range of distribution network scenarios. For instance, the length of line segment 1 and 2 indicates the location of the PVC-Q with respect to the substation while the length of line segment 3 signifies the proximity of adjacent PVC-Qs. Similarly, a range of R/X ratio can be chosen to represent a dense urban ($R/X \approx 4$) to sparse rural ($R/X \approx 10$) low-voltage (LV) network as well as the medium-voltage (MV) level ($R/X \approx 1$) with industrial/commercial customers.

Stability of the distribution network with PVC-Qs (PEC in series with the loads) is compared against the case where PoC voltage is regulated by shunt (connection with respect to the loads) converters such as STATCOM or DG inverters. The inverters in both cases are chosen to be equivalent in terms of PoC voltage regulation capability. More detailed information is provided in Appendix C. The SSM of a network with DG inverters is fairly well reported [126] and hence, not repeated here. The SSM of the study system shown in Fig. 5.11, but with the two PVC-Qs replaced by equivalent DG inverters, reveals the presence of four

modes with much higher frequencies (4798.3Hz, 4695Hz, 1124.46Hz and 996.23Hz) and much lower damping ratios (3.6%, 3.7%, 16.7%, 16.9%) compared to the case with PVC-Q.

5.3.1 Distance from Substation

The impact of distance of the PVC-Q or shunt converter from the substation is investigated by varying the length of line segments 1 and 2 which are separated by a unity power factor load. The length of the remaining line segments are kept the same as the base case (as in Fig. 5.11) and the R/X ratio of all segments are fixed at 4.26. The impact of varying the lengths between 0.1km to 2km on the 472.31 Hz & 369.63 Hz modes is shown in Fig. 5.12 (a) for PVC-Q. The frequency of both modes is significantly higher for PVC-Qs located farther away from the substation. However, the real part remains well beyond $-4000s^{-1}$ (i.e. far away in the left half of s-plane) without posing any threat to network stability.

Fig. 5.12 (b) shows the impact with PVC-Qs replaced by equivalent DG inverters. In this case, increasing distance from the substation causes the high frequency modes (> 4 kHz) to move away from the imaginary axis. It is worth noting that with PVC-Q the modes are much farther away in the left half of the s-plane compared to the case with DG inverters.

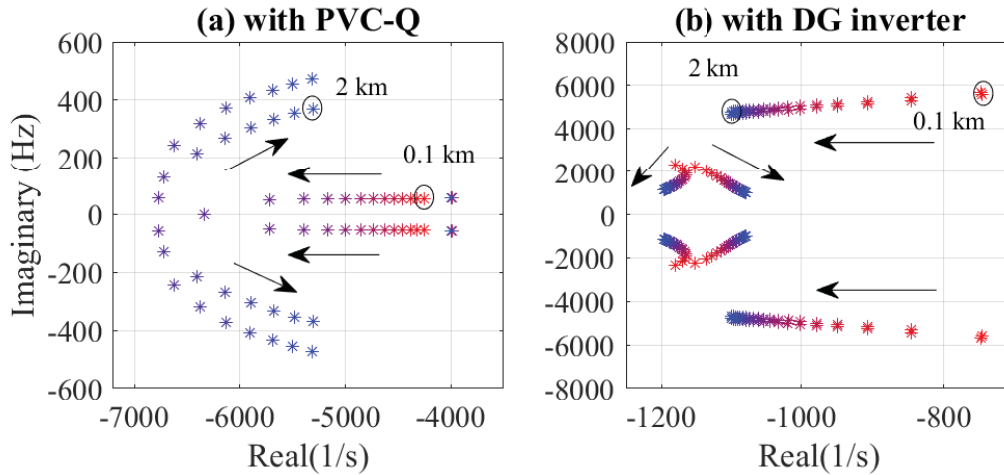


Fig. 5.12 Root locus with (a) PVC-Q and (b) DG inverters when length of L1 & L2 is varied from 0.1km to 2km (red to blue) while keeping the other line parameters constant

5.3.2 Electrical Proximity

The length of line segment 3 is varied to represent the electrical proximity between adjacent PVC-Q or DG inverters. A single PVC-Q will typically be installed at the PoC of a cluster of

customers instead of individual customers to exploit the load diversity. Depending on the number of customers within a cluster, the distance of separation between adjacent PVC-Qs will vary. Fig. 5.13 (a) shows that separation distance has hardly any effect on the frequency of the mode while the real part remains beyond $-3500s^{-1}$, thus posing no threat to system stability.

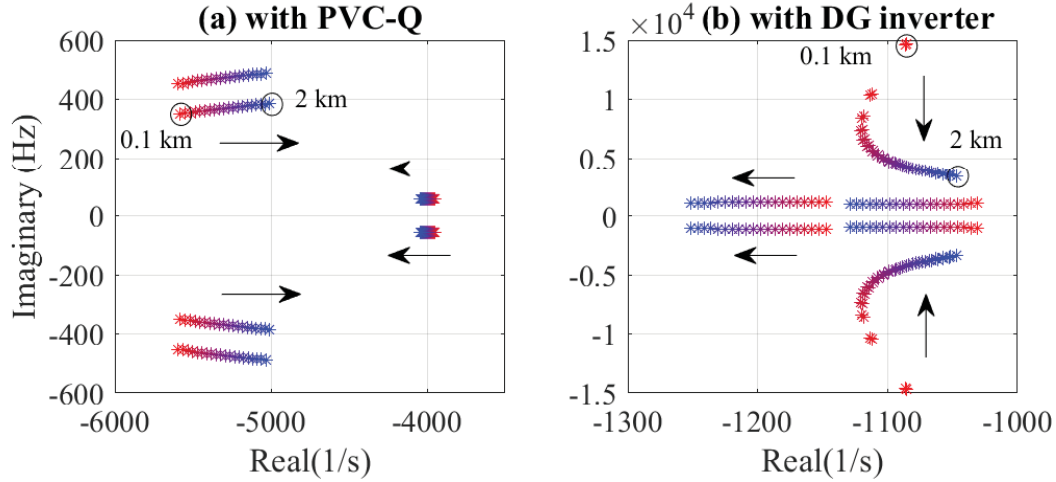


Fig. 5.13 Root locus with (a) PVC-Q and (b) DG inverters when length of L3 is varied from 0.1km to 2km (red to blue) while keeping the other line parameters constant

Fig. 5.13 (b) shows that DG inverters in close electrical proximity will result in very high frequency modes (> 10 kHz). With increasing separation, the frequency reduces but the modes migrate closer to the imaginary axis.

5.3.3 Distribution Network Voltage Level

The R/X ratio of the line segments 1 and 2 is varied between 1 (MV level) to 10 (LV level sparse rural network). The state variables associated with line segments 1 and 2 have dominant participation in the 472.31 Hz & 369.63 Hz modes present in the case of PVC-Q. This results in a large shift in those modes seen in Fig. 5.14 (a). For higher R/X ratios, the modes move farther to left of the s-plane due to larger damping introduced by higher resistance. Similar effect is observed in Fig. 5.14 (b) in case of DG inverter except that the frequencies increase slightly for higher R/X unlike the case with PVC-Q where it reduces slightly.

Fig. 5.15 shows the effect of varying the R/X ratio of line segment 3 while keeping other line parameters constant. The state variable associated with this line segment shows very

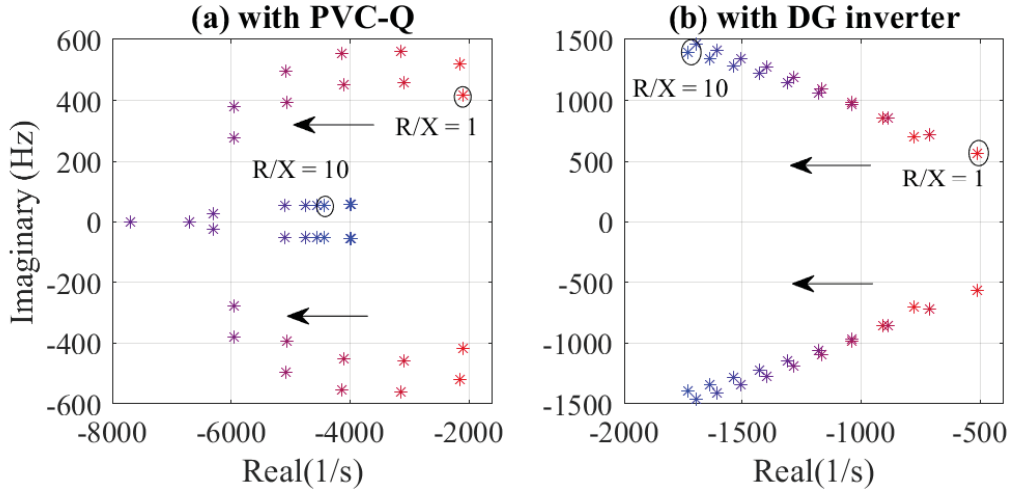


Fig. 5.14 Root locus with (a) PVC-Q and (b) DG inverters when R/X ratios of L1 & L2 are varied from 1 to 10 (red to blue) while keeping the other line parameters constant

limited impact on the three system modes (Fig. 5.15 (a)) compared to varying the R/X of line segment 1 & 2 (Fig. 5.14 (a)). For the case with DG inverter, varying the R/X ratio of line segment 3 actually shows movement of the high frequency mode whereas, limited movement is observed for the lower frequency mode compared to Fig. 5.14(b).

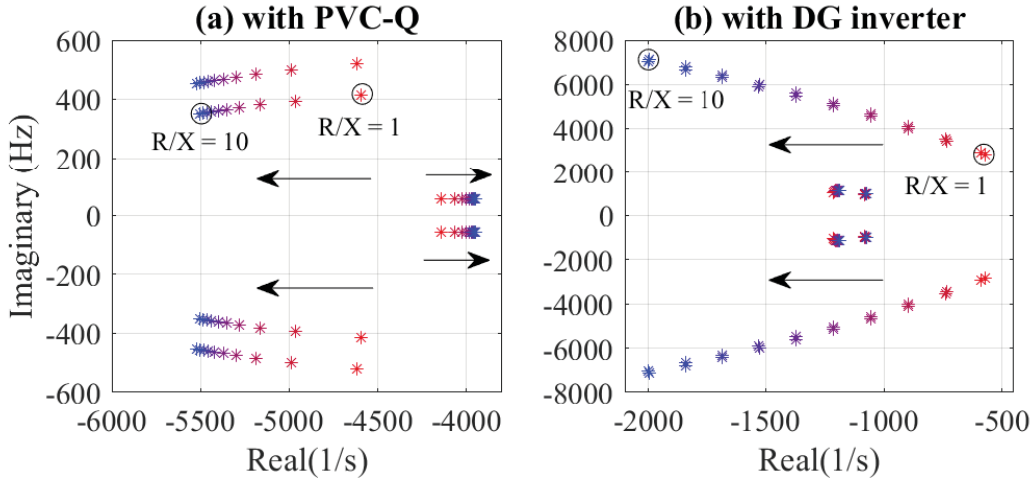


Fig. 5.15 Root locus plot with (a) PVC-Q and (b) DG inverters when R/X ratio of L3 is varied from 1 to 10 (red to blue) while keeping the other line parameters constant

From the discussion in Sections 5.3.1, 5.3.2 and 5.3.3, it can be concluded that the installation of PVC-Qs at different locations with respect to the substation, with varying electrical separation and at MV and LV levels will not pose any threat to distribution network stability. In fact, the situation is more stable (modes are farther to the left of s-plane) with PVC-Q than equivalent penetration of DG inverters. Unlike the case of a microgrid [128],

the choice of voltage droop gain did not have a major influence on stability in this case due to the stiff (or strong) upstream system mimicked by the voltage source in Fig. 5.6 & 5.11.

The small signal analysis presented here is based on a simple network. However, it covers a wide range of scenarios encountered in practical distribution networks. For example, the impact of different distance of an PVC-Q from the substation is captured by varying the length of the line segments 1 and 2 while maintaining the R/X ratio and the length of other lines constant. Similarly, the impact of electrical proximity between adjacent PVC-Qs is investigated by varying the length of the line segment 3 while keeping the length and R/X ratio of other lines constant. Voltage level (e.g. MV or LV) and topology (e.g. dense urban, sparse rural network) of distribution network is accounted for in the study by varying the R/X ratio of the line segments.

5.4 Conclusion

In this chapter, the vector control of a load equipped with point-of-load voltage control (PVC) for reactive power compensation only (referred to as PVC-Q for simplicity) is firstly developed, followed by a linearised state-space model (LSSM) of a distribution network with multiple PVC-Qs using the component connection method for stability analysis, which can be easily scaled up to include more loads with PVC and DG inverters.

Through frequency domain analysis, it is shown that PVC-Qs in distribution networks are not likely to threaten the small signal stability of the system. In fact, the stability margin with PVC-Q installed is more than the case with equivalent penetration of shunt converters such as DG inverters. The distance of an PVC-Q from the substation, proximity between adjacent PVC-Q installations and the R/X ratio of the distribution feeder influence the stability. However, for a wide range of distance, proximity and R/X ratios representing low- to medium voltage levels and typical dense urban networks to sparse rural feeders, only benign impact on system stability was observed.

Chapter 6

System Stability with Point-of-load Voltage Control for Flexible Demand

Following Chapter 5, this chapter continues to investigate possible instabilities induced by loads with point-of-load voltage control (PVC) for flexible demand in an isolated microgrid (IMG) with converter-interfaced distributed generators (CDGs) such as wind, solar photovoltaic (PV) and battery energy storage etc. but no synchronous generators. Note that loads with PVC in this chapter are also referred to as smart loads (SLs) for simplicity.

The dynamics of the control loops of SLs is considered for stability analysis of power networks in Chapter 5, in general but not specifically for IMGs. The stability problem revealed in Chapter 5 is mainly associated with the dynamics of the filter components leading to relatively high frequency (hundreds or thousands of Hz) instability which is fundamentally different in nature from the low frequency oscillatory stability problem studied in this chapter. Moreover, the last chapter considered a configuration with only the series converter in its voltage compensator, which could account for the absence of low frequency stability problem introduced in this chapter.

In this chapter, the stability analysis presented in Chapter 5 is extended to include the dynamics of the shunt converter and the DC link and then applied in the context of IMG to analyse the role of SLs in low frequency dynamics. A simple isolated microgrid with 100% converter-interfaced renewables is considered which can be extended to larger power grids.

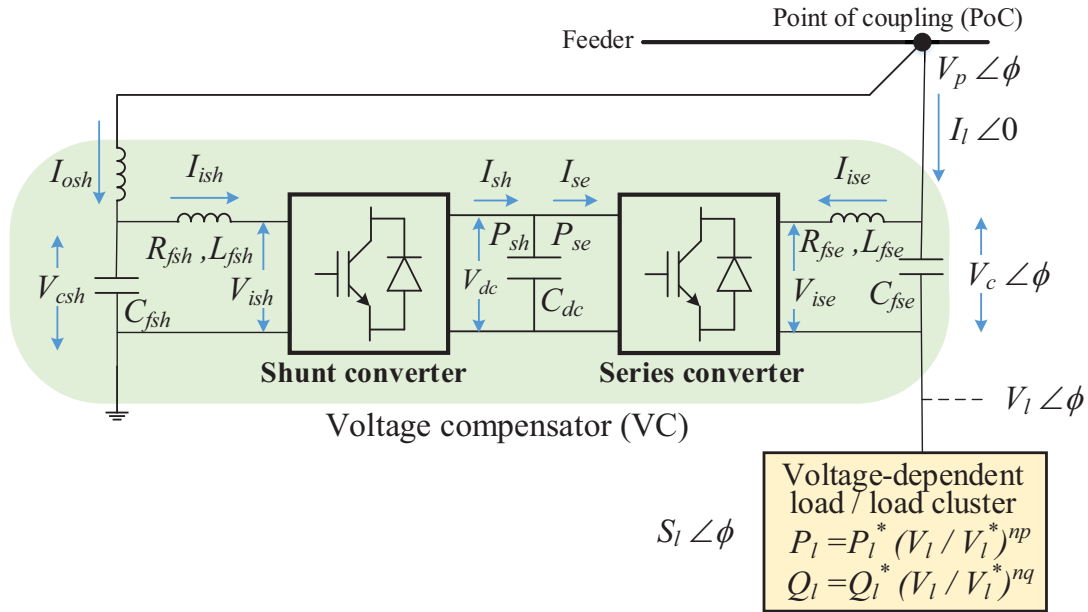


Fig. 6.1 A smart load (SL) with a series-shunt converter arrangement of voltage compensator (VC)

6.1 Isolated Microgrid with Smart Loads

Operation of an IMG with CDGs and SLs is considered in this section. The CDGs operate in grid forming mode using conventional P - f , Q - V droop and cascaded voltage and current control strategy as in [71]. The SLs contribute to frequency regulation in grid-following mode using an equivalent P - f droop control mechanism as discussed later.

6.1.1 Operation of Smart Loads

The configuration of the SL is the same as that introduced in Section 2.2, i.e. a voltage compensator (VC) with a series-shunt converter arrangement which decouples the voltage-dependent load (or load cluster) from the point of coupling (PoC) with the supply feeder. The detailed configuration is shown in Fig. 6.1 for convenience.

The active power consumption of the SL can be controlled within certain limits by adjusting the voltage (V_c) injected by the series converter (SeC). Thus the SL can participate in frequency regulation to relieve the burden on the CDGs to some extent. For maximum possible change in active power consumption of SL for a given apparent power rating of the VC, the

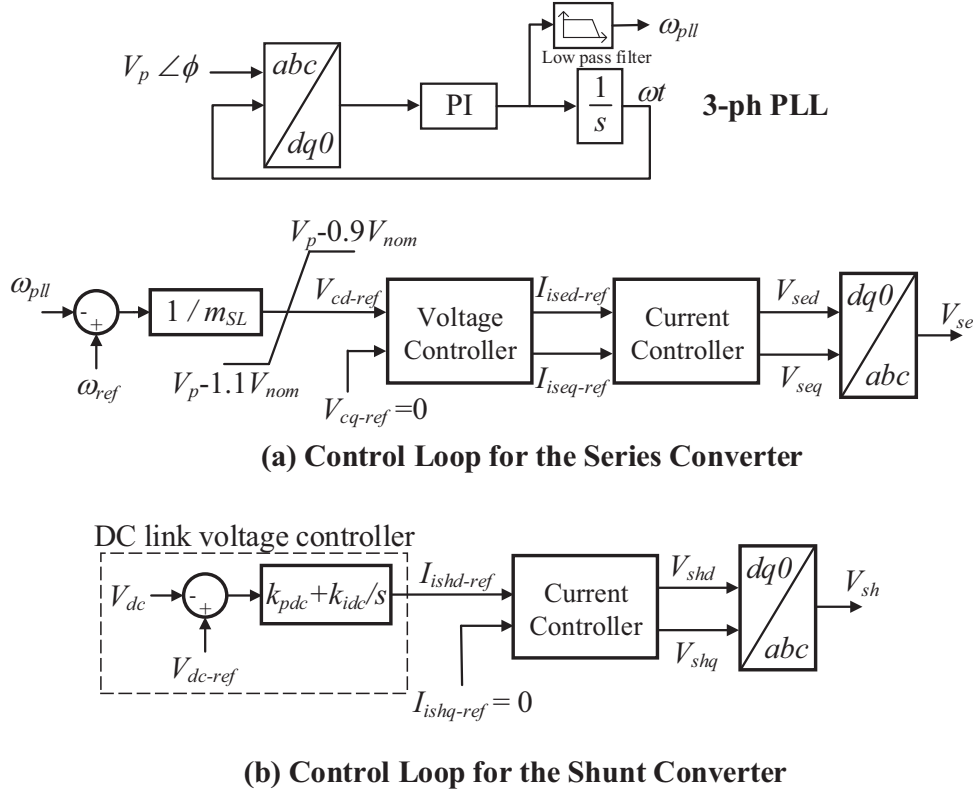


Fig. 6.2 Control of series and shunt converter (SeC and ShC) of a smart load

voltage (V_c) injected by the SeC is controlled to be in phase (for demand reduction) or out of phase (for demand increase) with the voltage of the PoC (V_p) or load (V_l) [132].

As introduced in Section 1.2.2, the shunt converter (ShC) maintains the DC link voltage and thereby, supports the active power exchanged by the SeC. Neglecting the converter losses, the active power exchanged by the SeC would be the same as the power drawn from or injected back to the grid though the ShC. Generally, the ShC is operated at unity power factor to keep its apparent power rating down to minimum.

6.1.2 Control of Smart Loads

A schematic overview of the control loops for the SeC and ShC are shown in Fig. 6.2. A three-phase phase-locked loop (PLL) is simplified by a proportional-integral (PI) controller and a second-order low pass filter. The PLL senses the PoC voltage ($V_p \angle \phi$) to maintain the injected voltage (V_c) in phase or out of phase and obtains the microgrid frequency ω_{pll} . The

standard decoupled vector control strategy with a synchronously rotating d - q reference frame [126] is used for the voltage and/or current controllers of SeC and ShC and are not discussed here in detail.

The burden of power sharing on the SLs depends on the droop gain (m_{SL}) defined in (6.1), where V_{cd-ref} is the reference of the d -axis component of the series voltage (V_c) to be injected by the SeC. As can be seen in Fig. 6.3 (a), for the same system frequency, a lower droop gain indicates a larger injected voltage (V_{cd}) which further implies SL would take up more burden in power sharing. The q -axis component of V_c is zero for in phase or out of phase injection. The saturation block maintains the load voltage within the stipulated limits of 0.9-1.1 p.u. [133]. For the ShC, the q -axis component of the filter inductor current (I_{ish}) is maintained at zero for unity power factor operation. It is to be noted that this chapter only focuses on small signal stability and neglects the non-linearity introduced by the saturation block.

$$m_{SL} = \frac{\omega_{ref} - \omega_{pll}}{V_{cd-ref}} \quad (6.1)$$

Using (6.1), the relation between the power consumption (P_l) of SL and the frequency (ω_{pll}) can be expressed as in (6.2).

$$\omega_{pll} = \omega_{ref} - m_{SL} \cdot \left[1 - \left(\frac{P_l}{P_l^*} \right)^{\frac{1}{n_p}} \right] \cdot V_l^* \quad (6.2)$$

This is similar to conventional P - f droop control of CDGs where P_l^* , V_l^* denote the nominal active power consumption and load voltage and n_p denotes the active power voltage sensitivity. The equation is simplified by assuming the nominal load voltage (with $V_c = 0$) to be the same as the PoC voltage neglecting the effect of filter components of the SeC.

The intersection between the droop characteristics of the CDG and SL determines the frequency of the IMG as shown in Fig. 6.3 (b). The system frequency is closer to nominal for a smaller droop gain (m_{SL2}) and/or a larger active power voltage sensitivity n_p of the SL. Thus, for a given n_p it is desirable to use as low a value of droop gain (m_{SL}) as possible.

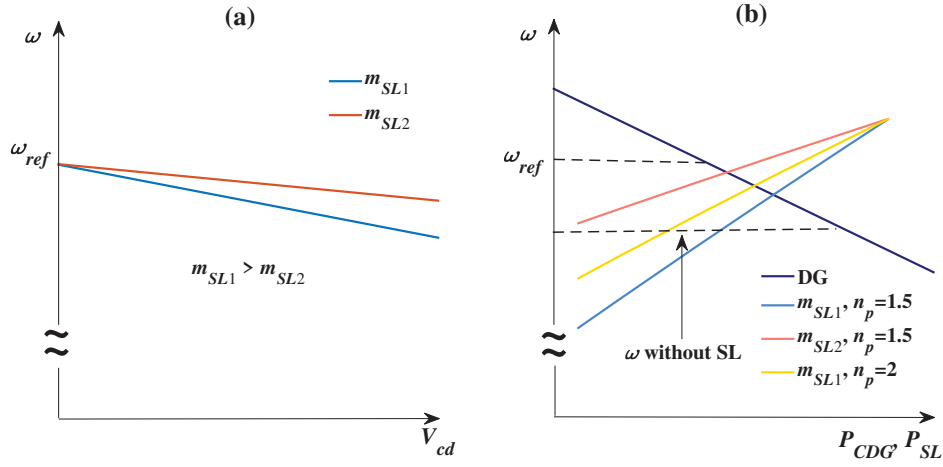


Fig. 6.3 (a) Relation between V_{cd} and system frequency for different droop gains; (b) droop characteristic of a converter-interfaced distributed generator (CDG) and smart load (SL)

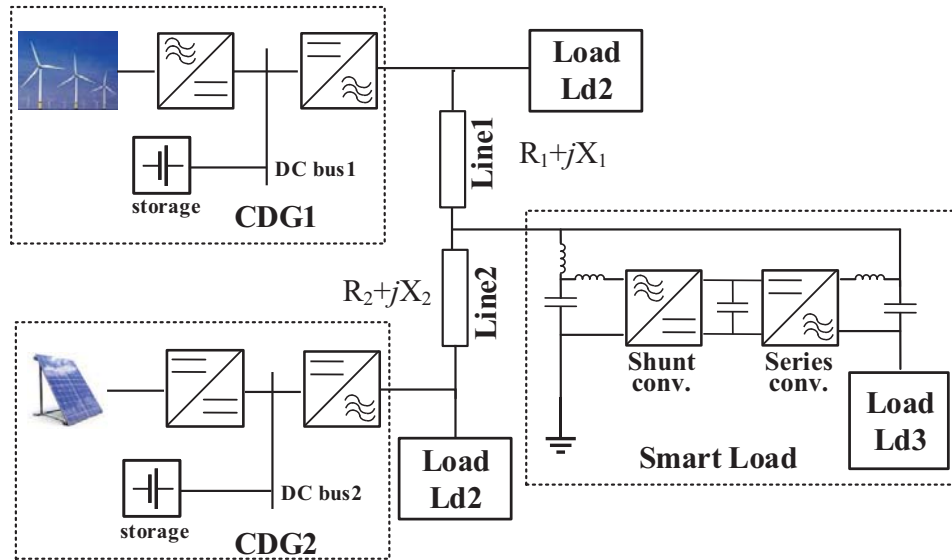


Fig. 6.4 An isolated microgrid (IMG) test system with two converter-interfaced distributed generators (CDGs) fuelled by wind and solar PV with battery energy storage and a smart load (SL)

6.1.3 Performance vs. Stability

The effectiveness of a SL is verified through a simple test IMG with two CDGs (CDG1 and CDG2), two normal loads (Ld1 and Ld2) and one SL, as shown in Fig. 6.4. CDG1 and CDG2 are hybrid distributed generators with wind/PV solar and battery energy storage connected on the DC bus. The parameters of the IMG (including two CDGs and two normal loads) and

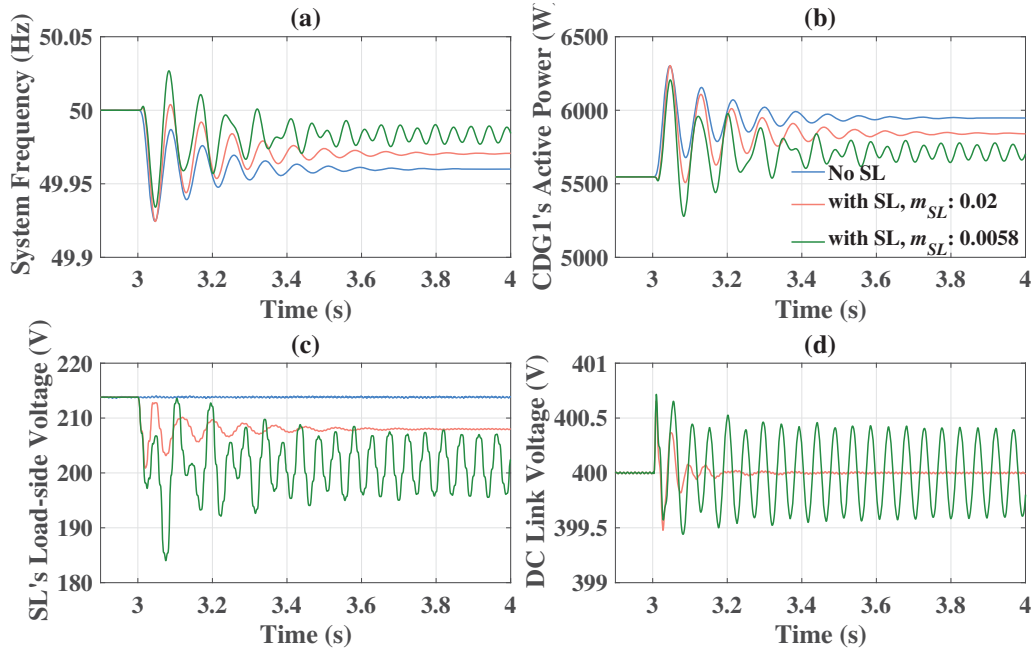


Fig. 6.5 Dynamic response of (a) microgrid frequency; (b) Active power output of CDG1; (c) RMS value of SL's load voltage; (d) DC-link voltage

the SL are provided in Table D.1 & Table D.2 in Appendix D. The normal loads are assumed to be of impedance type while the load within the SL is modelled in exponential form [82]. An active power voltage sensitivity n_p of 1.5 [134] is used for the nominal case but the trend for different values of n_p is provided in Section 6.3.

The dynamic response of the IMG and the SL's internal variables is shown in Fig. 6.5 following a step reduction in active power reference of CDG2 by 0.8 kW at $t = 3$ s. This change could be due to a sudden variation of solar irradiance with insufficient battery SoC to compensate for it. The blue trace (marked 'no SL') represents the case where all three loads in the IMG are normal loads while the red and green traces consider the SL with two different droop gains (m_{SL}) as marked on the legend. It can be seen that the SL reduces the deviation of frequency from the nominal value and the extent of the frequency deviation decreases further with lower droop gains as expected from Fig. 6.3. This demonstrates the fact that the SLs provide some cushion in face of intermittent renewable generation in an IMG. However, the dynamic response becomes more oscillatory and approaches instability as the droop gain of SL (m_{SL}) is reduced. Also dynamic response for low droop gains reflects two interleaved modes. To find the root cause of this trend, a linearised state space model for stability analysis of the IMG (in Fig. 6.4) is developed next in Section 6.2.

6.2 Linearised State Space Model

The linearised state space model (LSSM) of an IMG with CDGs in grid-forming mode [71] is extended to include a SL with a series-shunt converter. The LSSM of the SeC of the SL can be taken from Chapter 5 while the CDGs and the line segments are modelled using equations (10) – (41), (50) – (51) from [71]. Hence, only the LSSMs of the ShC of the SL, the DC link and the voltage-dependent load are presented here. In the following subchapters, the LSSM of individual components are summarised referring to Figs 6.1 and 6.2 and the notations used there.

6.2.1 DC Link and its Voltage Controller

As shown in Fig. 6.1, the DC link dynamics can be expressed by (6.3) neglecting the converter losses. Thus, the LSSM of the DC link is given by (6.4).

$$\begin{aligned} C_{dc} \frac{dV_{dc}}{dt} &= I_{sh} - I_{se} = \frac{P_{sh}}{V_{dc}} - \frac{P_{se}}{V_{dc}} \\ &= \frac{1}{V_{dc}} \left(V_{ishd} I_{ishd} + V_{ishq} I_{ishq} - V_{ised} I_{ised} - V_{iseq} I_{iseq} \right) \end{aligned} \quad (6.3)$$

$$\begin{aligned} \left[\Delta \dot{V}_{dc} \right] &= \left[\frac{V_{ised0} I_{ised0} + V_{iseq0} I_{iseq0}}{C_{dc} V_{dc0}^2} - \frac{V_{ishd0} I_{ishd0} + V_{ishq0} I_{ishq0}}{C_{dc} V_{dc0}^2} \right] \left[\Delta V_{dc} \right] \\ &+ \frac{1}{C_{dc} V_{dc0}} \left[\begin{array}{cccccc} I_{ishd0} & I_{ishq0} & V_{ishd0} & V_{ishq0} & -I_{ised0} & -I_{iseq0} & -V_{ised0} & -V_{iseq0} \end{array} \right] \times \\ &\left[\begin{array}{cccccc} \Delta V_{ishd} & \Delta V_{ishq} & \Delta I_{ishd} & \Delta I_{ishq} & \Delta V_{ised} & \Delta V_{iseq} & \Delta I_{ised} & \Delta I_{iseq} \end{array} \right]^T \end{aligned} \quad (6.4)$$

The DC link voltage control loop has only one state variable (Δx_{dc}) associated with the integrator of the PI controller. The input and output are the DC link voltage (ΔV_{dc}) and d -axis current reference $\Delta I_{ishd-ref}$. The LSSM of the DC link voltage controller is given by (6.5) and (6.6).

$$\left[\Delta \dot{x}_{dc} \right] = \left[0 \right] \left[\Delta x_{dc} \right] + \left[-1 \right] \left[\Delta V_{dc} \right] \quad (6.5)$$

$$\begin{bmatrix} \Delta I_{ishd-ref} \end{bmatrix} = \begin{bmatrix} k_{idc} \end{bmatrix} \begin{bmatrix} \Delta x_{dc} \end{bmatrix} + \begin{bmatrix} -k_{pdc} \end{bmatrix} \begin{bmatrix} \Delta V_{dc} \end{bmatrix} \quad (6.6)$$

6.2.2 Current Controller of the Shunt Converter

The standard decoupled vector control strategy with a synchronously rotating d - q reference frame [126] is used for the current controller of the shunt converter (ShC). The filter inductor current control is achieved with PI controllers. It is to be noted that a negative gain (-1) is introduced here to account for the direction of the measured current which is considered to be positive from the PoC towards the ShC. The LSSM of the current controller of the ShC is given by (6.7) and (6.8). The state variables associated with the PI controllers in d and q axis loops are denoted by $\Delta\gamma_{shd}$ and $\Delta\gamma_{shq}$ while the corresponding controller parameters are given by k_{pcsh} and k_{icsh} . The incremental change in d and q axis components of the voltage across the converter and the input current are denoted by ΔV_{ishd} , ΔV_{ishq} and ΔI_{ishd} , ΔI_{ishq} respectively. The nominal frequency is denoted by ω_0 .

$$\begin{bmatrix} \Delta\dot{\gamma}_{shd} \\ \Delta\dot{\gamma}_{shq} \end{bmatrix} = \begin{bmatrix} 0 \end{bmatrix} \begin{bmatrix} \Delta\gamma_{shd} \\ \Delta\gamma_{shq} \end{bmatrix} + \begin{bmatrix} 1 & 0 \\ 0 & 1 \\ -1 & 0 \\ 0 & -1 \end{bmatrix}^T \begin{bmatrix} \Delta I_{ishd-ref} \\ \Delta I_{ishq-ref} \\ \Delta I_{ishd} \\ \Delta I_{ishq} \end{bmatrix} \quad (6.7)$$

$$\begin{bmatrix} \Delta V_{ishd} \\ \Delta V_{ishq} \end{bmatrix} = \begin{bmatrix} -k_{icsh} & 0 \\ 0 & -k_{icsh} \end{bmatrix} \begin{bmatrix} \Delta\gamma_{shd} \\ \Delta\gamma_{shq} \end{bmatrix} + \begin{bmatrix} -k_{pcsh} & 0 \\ 0 & -k_{pcsh} \\ k_{pcsh} & -\omega_0 L_{fsh} \\ \omega_0 L_{fsh} & k_{pcsh} \end{bmatrix}^T \begin{bmatrix} \Delta I_{ishd-ref} \\ \Delta I_{ishq-ref} \\ \Delta I_{ishd} \\ \Delta I_{ishq} \end{bmatrix} \quad (6.8)$$

6.2.3 Shunt Converter Filter

The LSSM of the LCL filter of the ShC is obtained by linearising the dynamics of the d and q axes components of the filter inductor current (ΔI_{ishd} , ΔI_{ishq}), capacitor voltage (ΔV_{cshd} , ΔV_{cshq}) and the coupling inductance current (ΔI_{oshd} , ΔI_{oshq}) and can be expressed as (6.9) and (6.10). Incremental change in PoC voltage is denoted by ΔV_{pd} and ΔV_{pq} and subscript '0' indicates the operating point about which linearisation is done.

$$\begin{bmatrix} \Delta \dot{I}_{ishd} \\ \Delta \dot{I}_{ishq} \\ \Delta \dot{V}_{cshd} \\ \Delta \dot{V}_{cshq} \\ \Delta \dot{I}_{oshd} \\ \Delta \dot{I}_{oshq} \end{bmatrix} = \begin{bmatrix} -\frac{R_{fsh}}{L_{fsh}} & \omega_0 & \frac{1}{L_{fsh}} & 0 & 0 & 0 \\ -\omega_0 & -\frac{R_{fsh}}{L_{fsh}} & 0 & \frac{1}{L_{fsh}} & 0 & 0 \\ -\frac{1}{C_{fsh}} & 0 & 0 & \omega_0 & \frac{1}{C_{fsh}} & 0 \\ 0 & -\frac{1}{C_{fsh}} & -\omega_0 & 0 & 0 & \frac{1}{C_{fsh}} \\ 0 & 0 & -\frac{1}{L_{fsh}} & 0 & 0 & \omega_0 \\ 0 & 0 & 0 & -\frac{1}{L_{fsh}} & -\omega_0 & 0 \end{bmatrix} \times \begin{bmatrix} \Delta I_{ishd} \\ \Delta I_{ishq} \\ \Delta V_{cshd} \\ \Delta V_{cshq} \\ \Delta I_{oshd} \\ \Delta I_{oshq} \end{bmatrix} \\
+ \begin{bmatrix} I_{ishq0} & \frac{1}{L_{fsh}} & 0 & 0 & 0 \\ -I_{ishd0} & 0 & \frac{1}{L_{fsh}} & 0 & 0 \\ V_{cshq0} & 0 & 0 & 0 & 0 \\ -V_{cshd0} & 0 & 0 & 0 & 0 \\ I_{oshq0} & 0 & 0 & \frac{1}{L_{csh}} & 0 \\ -I_{oshd0} & 0 & 0 & 0 & \frac{1}{L_{csh}} \end{bmatrix} \begin{bmatrix} \Delta \omega_{pll} \\ \Delta V_{ishd} \\ \Delta V_{ishq} \\ \Delta V_{pd} \\ \Delta V_{pq} \end{bmatrix} \quad (6.9)$$

$$\begin{bmatrix} \Delta I_{ishd} \\ \Delta I_{ishq} \\ \Delta V_{cshd} \\ \Delta V_{cshq} \\ \Delta I_{oshd} \\ \Delta I_{oshq} \end{bmatrix} = [\mathbf{I}] \begin{bmatrix} \Delta I_{ishd} \\ \Delta I_{ishq} \\ \Delta V_{cshd} \\ \Delta V_{cshq} \\ \Delta I_{oshd} \\ \Delta I_{oshq} \end{bmatrix} + [\mathbf{0}] \begin{bmatrix} \Delta \omega_{pll} \\ \Delta V_{ishd} \\ \Delta V_{ishq} \\ \Delta V_{pd} \\ \Delta V_{pq} \end{bmatrix} \quad (6.10)$$

6.2.4 Voltage-dependent Load

The dynamic model of a constant power load [135] is extended to include different power voltage sensitivity (n_p, n_q). At a given operating point, the active power consumption of the voltage dependent load is given by (6.11), where V_{ld0}, V_{lq0} and I_{ld0}, I_{lq0} are d and q axis components of the load voltage and current at that operating point with a power factor $\cos \phi$. The q -axis component of the load voltage is zero ($V_{l0} = V_{ld0}$) as the voltage (V_c) injected by the SeC is in phase or out of phase with the PoC and load voltage.

$$V_{ld0} \cdot I_{ld0} = V_{l0} \cdot I_{l0} \cdot \cos \phi = P_l^* \left(\frac{V_{ld0}}{V_l^*} \right)^{n_p} \quad (6.11)$$

A small perturbation about the nominal load voltage and current gives rise to (6.12).

$$(V_{l0} + \Delta V) \cdot (I_{l0} + \Delta I) \cdot \cos \phi = P_l^* \left(\frac{V_{ld0} + \Delta V}{V_l^*} \right)^{n_p} \quad (6.12)$$

Neglecting high order terms in (6.12), the equivalent incremental resistance and inductance of the load can be expressed as (6.13) and (6.14).

$$R_{n_p} = \frac{\Delta V}{\Delta I} \cos \phi = \frac{V_{ld0}^{2-n_p}}{\frac{P_l^*}{V_l^{*n_p}} \cos \phi (n_p - 1)} \cos \phi \quad (6.13)$$

$$L_{n_q} = \frac{\Delta V}{\Delta I} \sin \phi = \frac{V_{ld0}^{2-n_q}}{\omega_0 \frac{P_l^*}{V_l^{*n_q}} \cos \phi (n_q - 1)} \sin \phi \quad (6.14)$$

Using R_{n_p} and L_{n_q} , the LSSM of a voltage-dependent load modeled in an exponential form can be expressed as (6.15) and (6.16).

$$\begin{bmatrix} \Delta \dot{I}_{ld} \\ \Delta \dot{I}_{lq} \end{bmatrix} = \begin{bmatrix} -\frac{R_{n_p}}{L_{n_p}} & \omega_0 \\ -\omega_0 & -\frac{R_{n_p}}{L_{n_p}} \end{bmatrix} \begin{bmatrix} \Delta I_{ld} \\ \Delta I_{lq} \end{bmatrix} + \begin{bmatrix} I_{lq0} & -I_{ld0} \\ \frac{1}{L_{n_q}} & 0 \\ 0 & \frac{1}{L_{n_q}} \\ -\frac{1}{L_{n_q}} & 0 \\ 0 & -\frac{1}{L_{n_q}} \end{bmatrix}^T \begin{bmatrix} \Delta \omega_{pll} \\ \Delta V_{pd} \\ \Delta V_{pq} \\ \Delta V_{cd} \\ \Delta V_{cq} \end{bmatrix} \quad (6.15)$$

$$\begin{bmatrix} \Delta I_{ld} \\ \Delta I_{lq} \end{bmatrix} = \begin{bmatrix} \mathbf{I} \end{bmatrix} \begin{bmatrix} \Delta I_{ld} \\ \Delta I_{lq} \end{bmatrix} + \begin{bmatrix} \mathbf{0} \end{bmatrix} \begin{bmatrix} \Delta \omega_{pll} \\ \Delta V_{pd} \\ \Delta V_{pq} \\ \Delta V_{cd} \\ \Delta V_{cq} \end{bmatrix} \quad (6.16)$$

where the d and q axis components of the capacitor voltage of the SeC filter are denoted by ΔV_{cd} and ΔV_{cq} .

6.2.5 Overall Model

The individual LSSM of ShC, DC link and the voltage-dependendent load (described above) together with LSSM of CDGs, line segments [71] and SeC (see Chapter 5) are stacked up to form the overall state (A), input (B), output (C) and transfer (D) matrices. The algebraic relations between the elements is captured through a matrix L_T by matching the inputs and outputs of each LSSM. Similar as in Chapter 5, the overall state matrix of the IMG is then derived from (6.17) using Component Connection Method (CCM) [125].

$$F = A + BL_T(I - DL_T)C^{-1} \quad (6.17)$$

It should be noted that the variables associated with the converter are transformed back and forth between their individual dq reference frame and a common DQ reference frame.

6.2.6 Validation

The developed LSSM of the IMG is validated using the test case shown in Fig. 6.4. The time-variation of the state variables obtained from the LSSM are compared against the simulation model in Matlab Simulink. A small disturbance is created at $t = 5$ s by reducing the frequency reference of the SL by 0.01 Hz for 3 cycles. Close match between the responses from the LSSM and the non-linear simulation model shown in Fig. 6.6, validates the developed LSSM. This is used for stability analysis in the next section.

6.3 Stability Analysis

The LSSM derived in Chapter 6.2 for the IMG test system in Fig. 6.4 is used for stability analysis to identify the root cause of the performance-stability trade-off observed in Section 6.1.

6.3.1 Modal Analysis

The LSSM of the IMG test system in Fig. 6.4 has 68 state variables in total. Eigenvalue analysis reveals 20 oscillatory modes with frequencies ranging from just over 10 Hz up to around 2000 Hz. The focus of this study is low frequency (< 30 Hz) modes with inadequate damping ($< 30\%$) which are at relatively larger risk of instability. The oscillatory modes are analysed under three separate cases:

- Case 1 - IMG without any SL

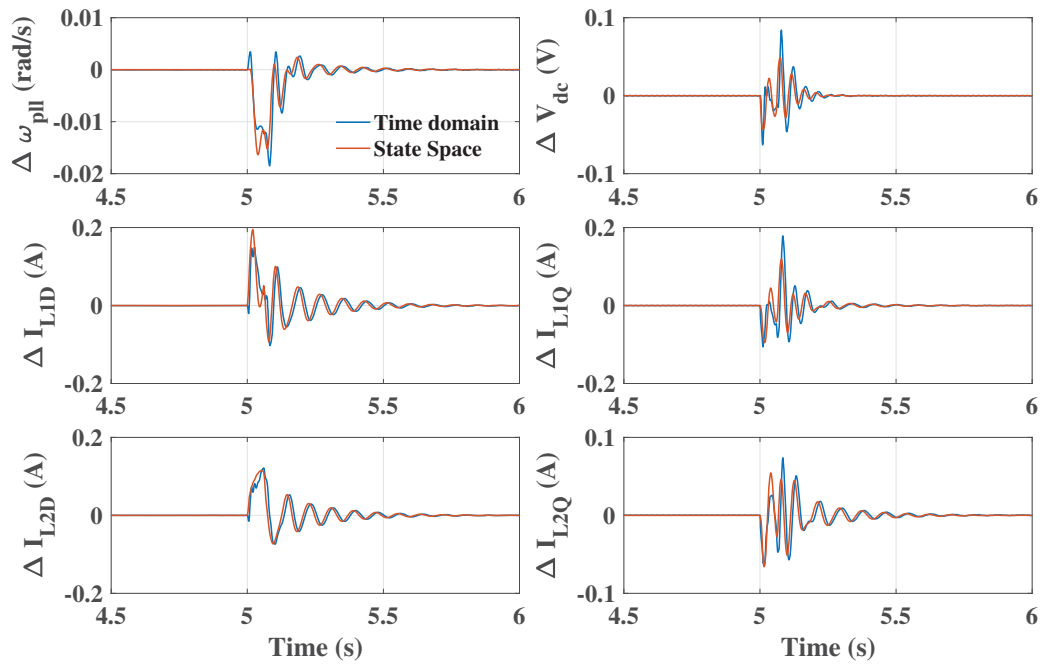


Fig. 6.6 Comparison of dynamic response from the linearised state space model (LSSM) and non-linear simulation model

- Case 2 - IMG with SL and dynamic model of SeC only
- Case 3 - IMG with SL and dynamic model of SeC, ShC, DC link and voltage dependent load (as presented in Section 6.2)

The low frequency oscillatory mode(s) for each case are listed in Table 6.1. Besides, the damping, frequency of all oscillatory modes of Case 3 and the corresponding participation factors of the dominant states are given in Table E.2 in Appendix E. The additional state variables are described in Table E.1.

The components with dominant participation in the low frequency mode(s) are identified from the participation factors (PF) of different state variables shown in Fig. 6.7. The PFs are calculated from the left and right eigenvectors and normalised with respect to the maximum PF for each mode [82].

The following observations can be made from the results presented in Tables 6.1, 6.2 and Fig. 6.7:

Table 6.1 Low Frequency Oscillatory Modes with and without Smart Loads

Case	Case 1 - IMG without SL	Case 2 - IMG with SL and dynamic modelling of SeC	Case 3 - IMG with SL and dynamic modelling of SeC, ShC, DC link	
Mode No.	1	1	1	2
Frequency (Hz)	11.87	12.01	12.18	7.53
Damping (%)	8.23	7.89	22.23	16.15
Dominant Components	CDG1, CDG2, Line2	CDG1, CDG2, Line2, SeC	CDG1, CDG2, Line2, SeC	CDG1, CDG2, Line2, SeC, ShC, DC link
Dominant States	1-8	1-10, 12-13	1-10, 12-13	3, 6, 8-18

Table 6.2 State Variable Description

No.	Component	Description
1-3	CDG1	power angle, active and reactive power
4-6	CDG2	power angle, active and reactive power
7-8	Line2	line currents (dq)
9	SeC	power angle
10-11		PLL's low pass filter
12-13		voltage and current controllers (d - axis)
14-15	ShC	current controller (dq)
16-17		currents of the coupling inductance (dq)
18		DC-link voltage

1) Case 1 and 2: The SL has little (but not zero) influence on the low frequency (12 Hz) mode which is primarily due to the CDGs. Introduction of the SL marginally reduces the participation of CDG2 and also decreases the damping ratio of the low frequency mode by a small ($< 0.5\%$) amount.

2) Case 3: Detailed dynamic model of the ShC, and DC link introduces another low frequency mode (Mode 2) with slightly higher frequency (22.12 Hz). This mode is primarily associated with the voltage and current controllers of both SeC, ShC, DC link dynamics, and the PLL and is not present with detailed dynamic model of the SeC only (Case 2). This highlights the importance of detailed dynamic model of the ShC and the DC link as presented earlier

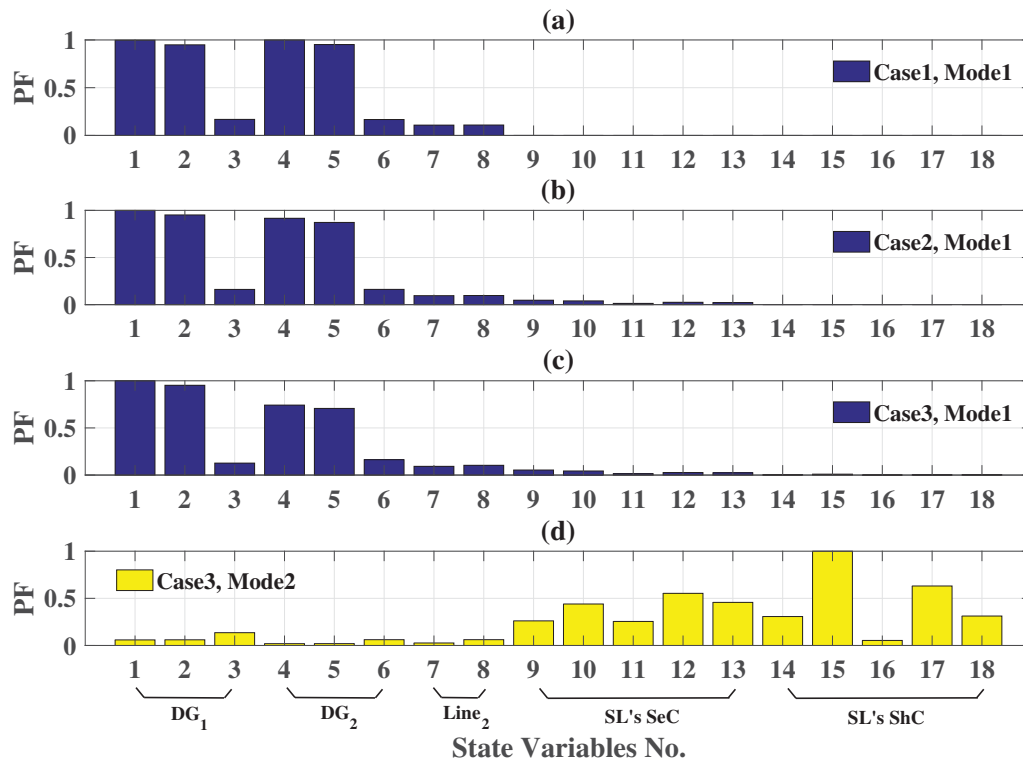


Fig. 6.7 Participation factor (PF) of dominant state variable in low frequency modes (a) Case1, Mode1; (b) Case2, Mode1; (c) Case3, Mode1; (d) Case3, Mode2

in Section 6.2. It is to be noted that both CDGs also participate in Mode 2 although to a lesser extent than in Mode 1. Under the nominal operating condition of the IMG, Mode 1 is primarily due to the CDGs and line segments, while Mode 2 is primarily due to the SL with little coupling between the CDGs and SLs.

The change in damping of the two low frequency modes (Modes 1 and 2) and the relative participation of the CDGs and SL (state variable with maximum participation for each component is shown) in Mode 1 are analysed next by varying the following parameters:

6.3.2 Droop Gain of Smart Load

In Section 6.1, it is observed that a low droop gain of the SL reduces the deviation from nominal frequency but could trigger an oscillatory (or even unstable) response. This is explained by the movement of Modes 1 and 2, shown in Fig. 6.8, as the droop gain is varied between 0.001 to 0.1.

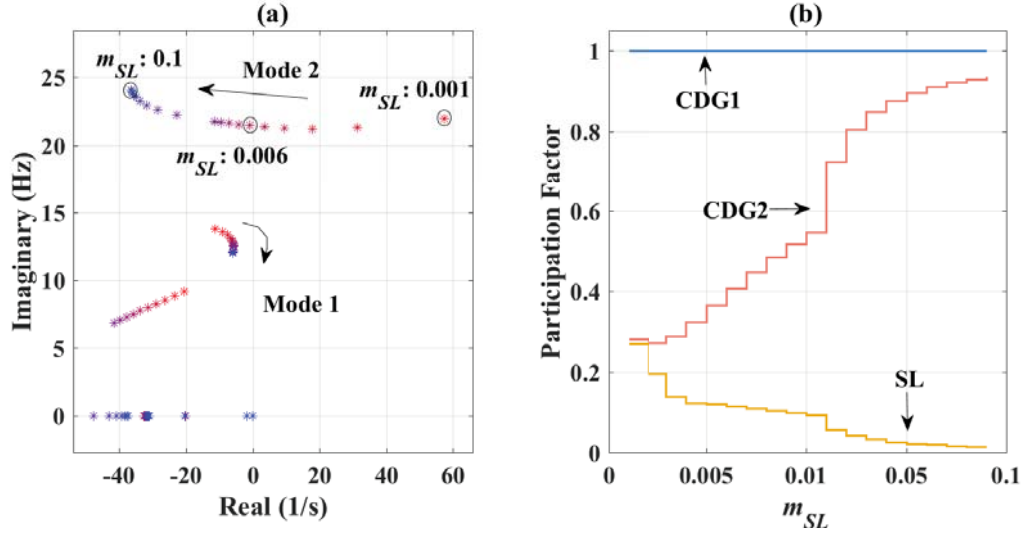


Fig. 6.8 Impact of varying droop gain of SL between 0.001 and 0.1 (a) root locus plot; (b) participation factors for Mode 1

With increasing droop gain, Mode 1 initially becomes more oscillatory before its damping actually starts to increase. Change of droop gain of the SL does not threaten the stability of Mode 1 unlike the case with CDGs [71]. Participation of SL in Mode 1 increases at the expense of CDG2 for smaller droop gains where the SL has a higher contribution to frequency regulation. However, Mode 2 becomes more oscillatory for lower droop gains and eventually gets unstable below a certain value (0.006). This corresponds to the observed responses in Section 6.1 which would not have been apparent without the detailed dynamic model of the ShC and DC link.

Reduction of damping of Mode 2 for lower droop gains could be explained as follows. As per (6.1), a low droop gain (m_{SL}) increases the voltage (V_c) injected by the SeC for a given frequency deviation. As a result, large amount of active power is exchanged with the ShC through the DC link triggering an oscillatory/unstable response of the DC link voltage regulation.

6.3.3 Phase-Locked Loop

The bandwidth of a synchronous reference frame PLL depends on the integrator gain of the PLL's PI controller [136]. To investigate the impact of PLL's bandwidth on the low frequency modes, the integrator gain of the PI controller (k_{i_pll}) is varied from 0.5 to 40.5 with a step of 2 for three sets of SL's droop gain. As can be seen in Fig. 6.9, Mode 2 moves towards the

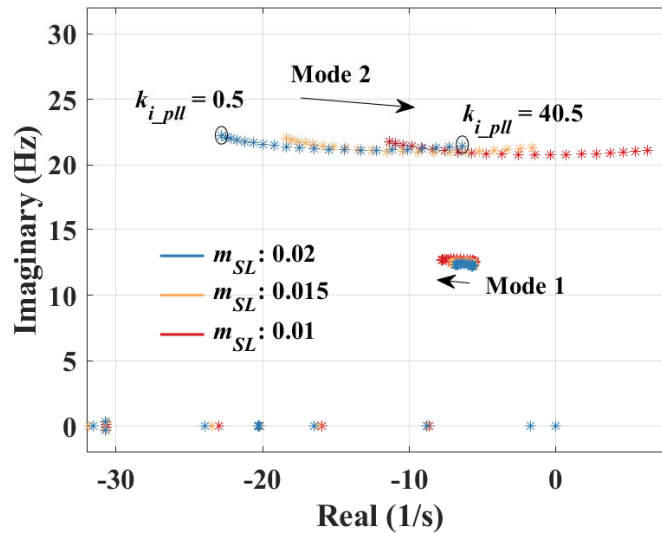


Fig. 6.9 Impact of bandwidth of PLL on low frequency modes

unstable region with an increase of k_{i_pll} (and hence bandwidth of the PLL), which indicates a faster PLL would have a negative impact on stability. It is shown that the system can get unstable when the droop gain of the SL is 0.01. This clearly suggests that the PLL dynamics should be incorporated when determining the lower limit of the droop gain of SL.

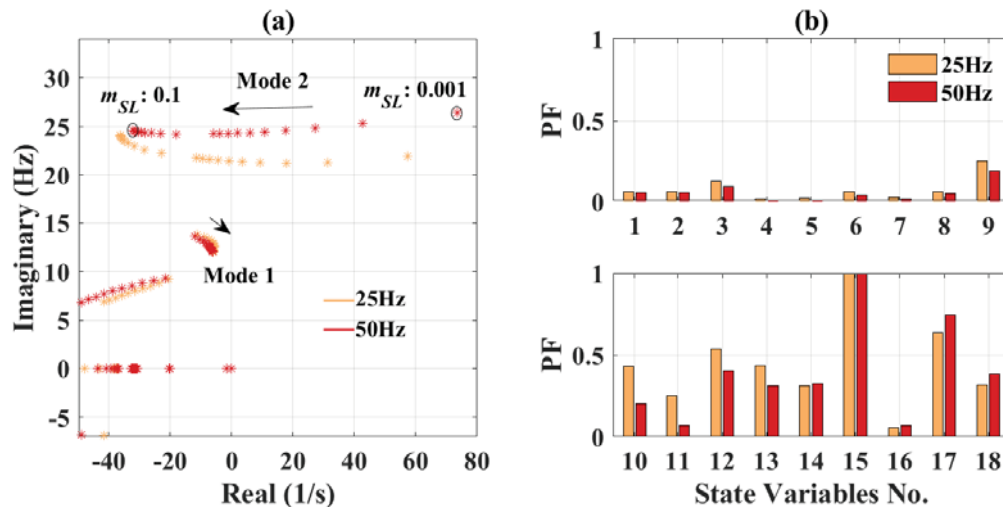


Fig. 6.10 Impact of cut-off frequency of PLL's low pass filter (LPF) (a) root locus; (b) participation factors in Mode 2

The effect of droop gain of the SL on low frequency modes is further evaluated for two different cut-off frequencies (25 and 50 Hz) of the PLL's low pass filter (LPF) as shown in

Fig. 6.10. From the root locus (Fig. 6.10 (a)) and the participation factors for nominal droop gain in Mode 2 (Fig. 6.10 (b)), it is evident that the basic characteristic of Mode 2 is very similar for both filter cut-off frequencies (as evident from the participation factors) although the cut-off frequency does have some influence on Mode 2, in particular. The movement of both modes is primarily due to the variation of droop gain irrespective of the filter cut-off frequencies. Fundamentally, Mode 2 is mainly influenced by the active power exchange between the series and shunt converter of the SL. The response time of each component within the feedback loop of the SL (e.g. cut-off frequency of the filter within the PLL) will certainly have an impact on this mode. However, the droop gain has dominant influence as it directly affects the power processed by the SL.

6.3.4 Line Parameters

The R/X ratio of Line1 is larger than 1 while the R/X ratio of Line2 is smaller than 1. The impact of varying the R/X ratio of Line 1 and Line 2 is shown in Figs 6.11 and 6.12, respectively.

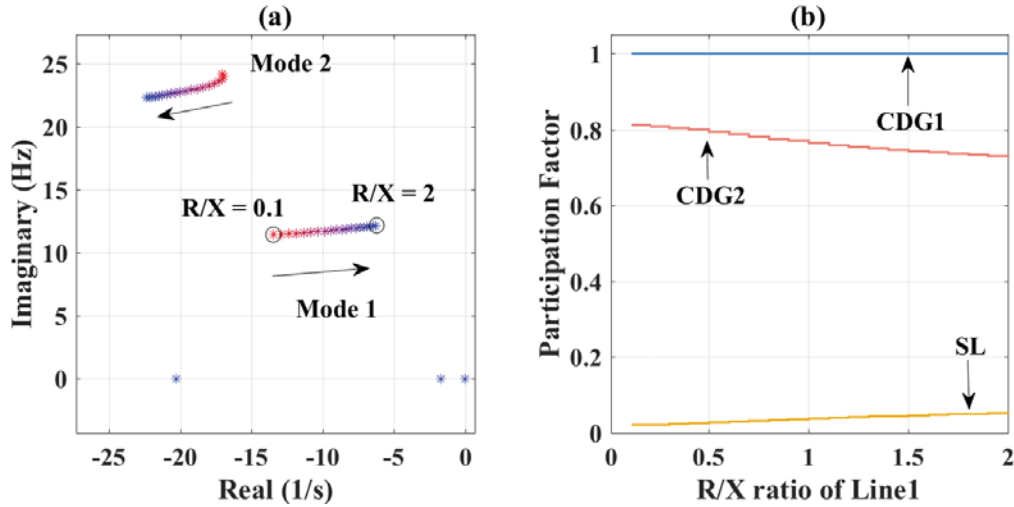


Fig. 6.11 Impact of R/X ratio of Line1 on low frequency modes (a) root locus plot; (b) participation factors for Mode 1

With increase of R/X ratio, Mode 1 becomes more oscillatory or even unstable due to the decreasing extent of P - f , Q - V decoupling which do not correspond to the adopted droop control strategy. Use of a larger coupling inductance or a virtual impedance [137] can mitigate this problem for low voltage IMGs with relatively high R/X ratio of the lines. The participation factor trend indicates stronger involvement of SL in Mode 1 for larger difference in R/X

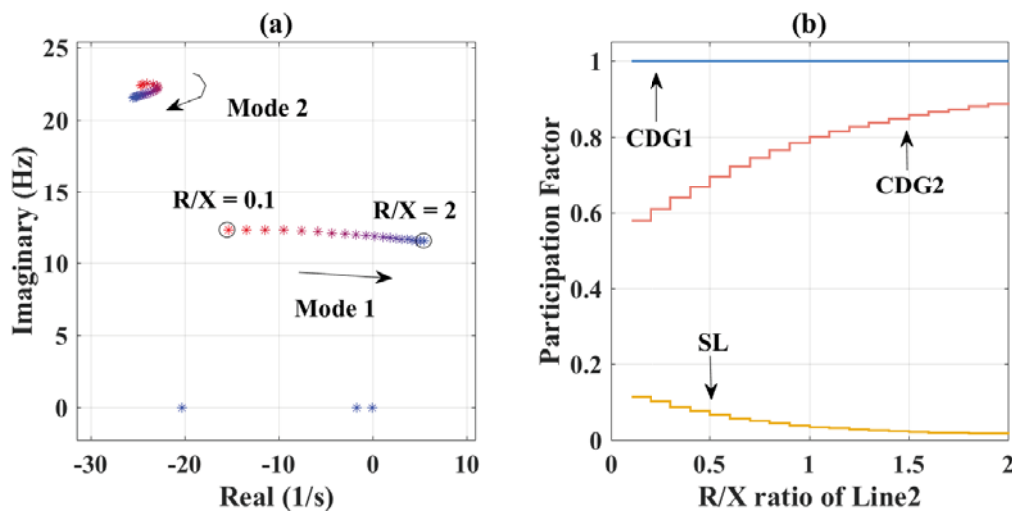


Fig. 6.12 Impact of R/X ratio of Line2 on low frequency modes (a) root locus plot; (b) participation factors for Mode 1

ratio of the lines.

Unlike Mode 1, the damping of Mode 2 eventually increases with R/X ratio which can be explained as follows. For a lower line reactance (X) (i.e. higher R/X), a given change in power consumption of the SL requires a lower change in phase angle (ϕ) of PoC voltage (V_p) and would have relatively low impact on the PLL dynamics which influences Mode 2 as in Fig 6.7.

6.3.5 Voltage Controller Gain of Series Converter

With the integral gain of the voltage controller of the SeC varying between 10 and 100, Fig. 6.13 shows that Mode 1 becomes more oscillatory to start with before getting increasingly damped. The point of inflection for Mode 1 on the root locus turns out to correspond to maximum participation of the SL.

6.3.6 Active Power Voltage Sensitivity of Smart Load

Increase in active power voltage sensitivity (n_p) of the SL improves the damping of Mode 2 as shown in Fig. 6.14. This could be attributed to the amount of power processed by the ShC, SeC and the DC link which reduces with increase in n_p . For instance, if $n_p = 0$, a reduced load voltage corresponds to an increase in both load current and voltage injected by the SeC

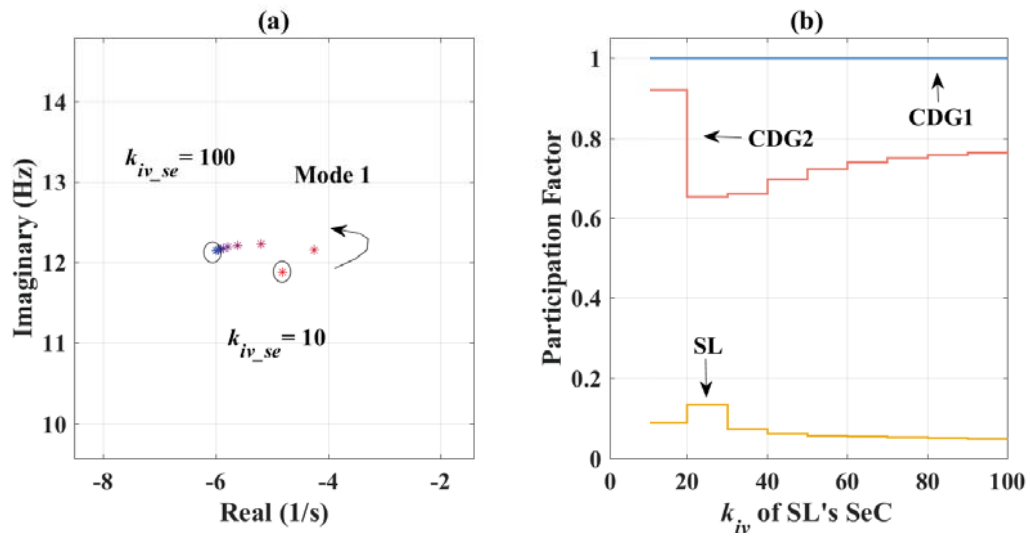


Fig. 6.13 Impact of integral gain of voltage controller of the SeC on low frequency modes (a) root locus plot; (b) participation factors for Mode 1

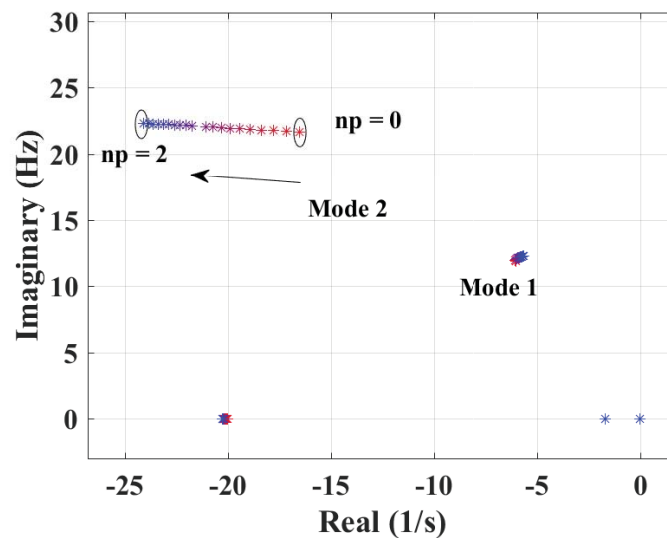


Fig. 6.14 Root locus plot with active power voltage sensitivity of smart load varying between 0 and 2

and hence, an increase in the power processed by the SeC and ShC. Participation of SL in Mode 1 is not given here as varying n_p has marginal impact on damping of Mode 1.

6.4 Conclusion

Loads with point-of-load voltage control (PVC)/smart loads (SLs) can provide a degree of flexibility in an isolated microgrid (IMG) with converter-interfaced distributed generators (CDGs) fuelled by renewable energy sources with battery energy storage and working in grid forming mode.

In this chapter, the linearised state space model (LSSM) of an IMG with CDGs and a SL is built. Modal analysis and time domain simulation show that 1) the SLs have marginal influence on the low frequency (<20 Hz) oscillations caused by droop control of CDGs. Damping of these oscillations is much less sensitive to change in droop gain of the SLs compared to the case with CDGs where the damping gets significantly worse for high droop gains of CDGs; 2) The dynamics of the PLL, DC link as well as the control loops of the series and shunt converters gives rise to another oscillatory mode at slightly higher frequency (>20 Hz) which becomes poorly damped and even unstable for low droop gains and high PLL bandwidth of SL. Lower droop gains of SL ensure better frequency regulation in face of intermittent renewable generation but the above stability constraint imposes a lower limit on the droop gain.

The stability model presented in this chapter and the insights developed would help fine tune the droop gains for SLs to ensure stable and acceptable oscillatory response in an IMG comprising of both CDGs and SLs.

Chapter 7

Summary and Future Work

7.1 Summary of Contributions

The contributions of this thesis are summarised in this chapter. To conclude, the thesis demonstrates the effectiveness of point-of-load voltage control (PVC) by presenting 1) a realistic quantification of demand reduction (DR) capability from PVC and corresponding techno-economic feasibility for Great Britain; 2) small signal stability analysis for systems with PVC for flexible demand or voltage regulation.

In Chapter 2, DR capability from PVC is quantified through high-resolution stochastic domestic demand models, a generic LV feeder and a CIGRE benchmark network. The DR capability of PVC is found to be twice as much as that of voltage control at the substation (VCS) on average for most part of the day at an expense of deploying a power electronic compensator (PEC) rated only about 10% of the diversified peak demand (DPD) of a cluster of domestic customers (CDC) in close electric proximity.

In Chapter 3, it is estimated that PVC in the urban domestic sector across Great Britain (GB) can provide up to 1.9 GW of DR depending on the time of the day and the season. Utilising this DR for enhanced frequency response (EFR) provision results in annual savings in system operation cost of £0.23b and £0.72b for 2030 Slow Progression (SP) and 2030 Green World (GW) scenarios, respectively. Due to the diminishing effect, the payback period for the investment in deploying the PECs increases with the penetration level of PVC, ranging from 0.8 to 3.5 years for different scenarios presented. It is interesting to note PVC in fully controllable mode, which allows increasing power consumption for higher EFR provision or decreasing the consumption when less EFR is required, can still gain significant economic benefits even when there is considerable level of battery energy storage system (BESS). This

further demonstrates that PVC could effectively complement BESS towards EFR provision in future GB power system.

The fast DR available from PVC is utilised for virtual inertia in Chapter 4. Through the CIGRE benchmark microgrid model, it has been shown that an average of 1.3s of inertia can be provided from the loads (with respect to the load power rating) within allowable voltage range under the control design following the UK National Grid frequency requirement. Time domain simulations confirm the effectiveness of PVC in improvement of rate of change of frequency (RoCoF) and frequency nadir.

Regarding the small signal stability analysis, the linearised state space model of a distribution network with PVC for voltage regulation (also termed as PVC-Q) as well as an IMG with PVC for flexible demand are developed in Chapter 5 & 6 respectively. It has been shown that for a wide range of distribution network scenarios, ranging from low- to medium voltage levels and dense urban to sparse rural feeders, SLQs are not likely to threaten the small signal stability of the system. In fact, the stability margin with SLQs is more than the case with equivalent penetration of shunt converter-interfaced distributed generators (CDGs).

In the case of an IMG, modal analysis reveals that the introduction of PVC-loads has marginal impact on the low frequency modes associated with the droop control of the CDGs. However, there is also a trade-off when choosing the droop gain of the loads with PVC. On one hand, lower droop gains ensure better frequency regulation in face of intermittent renewables; on the other, an oscillation mode at a frequency slightly higher than 20 Hz could become poorly damped or even unstable for lower droop gains. This mode is related with the dynamics of the phase-locked loop (PLL), DC link along with the control loops of the series and shunt converters of the PVC-loads and would not be apparent from the simplified models (i.e. neglecting dynamics of the shunt converter and DC link) reported in previous literature.

I would like to acknowledge my collaborators Mr Luis Badesa, Mr Tong Chen and Dr Diptargha Chakravorty again for their contributions in developing SUC model, design of virtual inertia from PVC and vector control of PVC-Q for voltage regulation, respectively.

7.2 Future Work

Based on the research carried out in this thesis, there are several areas of interest that deserve further investigation in the future.

- **Study the effect of embedded generation** The effect of embedded generation on DR capability from PVC has not been considered in this thesis. However, this issue should be addressed with an increasing penetration of embedded generation, especially roof-top photovoltaic (PV) [4] across the GB. The DR capability from PVC would vary depending on the location, different penetration level of embedded generation etc. and correlation between demand and renewable profiles considering diurnal and seasonal variations and should be verified under realistic scenarios.
- **Refine value assessment considering multi-service provision from PVC** Flexibility in demand through PVC can be incorporated in various system-level optimisation schemes such as active network management. Value assessment of PVC can be extended to include other ancillary services besides EFR.
- **Estimate DR capability in near-real time** The DR capability provided in this thesis is based on simulated data from high-resolution demand model. It would be quite conservative if the system operators adopt the lower bound 5 pc trace, which is the very likely amount of DR availability. For practical application of flexible demand from PVC, it's essential for system operators to estimate the DR capability in near-real time (say 15 min or less) in presence of uncertainties in demand and embedded generation which requires near-real time demand and renewable forecast as well as online power flow calculation.
- **Analyse the interplay between other voltage control and PVC** There are many centralised [138] and decentralised approaches [65–67] for voltage regulation in distribution networks under high penetration of distributed generation. It would be interesting to investigate how PVC would perform alongside these schemes and how those could be coordinated.
- **Efficient PEC topology to cater for specific phase angle requirements** PVC with back-to-back configuration allows injecting a voltage with any arbitrary angle. However, for applications with specific phase angle requirements, say demand reduction, a more efficient and optimised PEC topology could be developed which might further reduce the implementation cost for such technology.
- **Practical aspects of PVC deployment** In reality, it is not practical or necessary (considering the economic diminishing effect) to implement PVC in all urban domestic customers. Besides, the rating of the converters should be standardised and uniform. Hence, it would be important to investigate questions like how many households should be included in a CDC or how to decide which CDCs to be deployed with PVC.

- **Extend stability analysis for realistic test systems** The stability analysis presented in this thesis could be extended for realistic test systems with uncertain generation and demand, a mix of grid-forming and grid-following converters as well as a mix of PVC for flexible demand and voltage regulation. The system should remain stable considering all the demand and renewable uncertainties and thereby requiring probabilistic/robust stability analysis approach [139]. Besides, this thesis does not consider an unbalanced system and neglects the harmonic frequency coupling between DC and AC side caused by switching process. If those issues are to be taken into account, a different modelling approach say dynamic phasor [140] or harmonic state space (HSS) [79, 80] may be required.

References

- [1] A. Chase, R. Gross, P. Heptonstall, M. Jansen, M. Kenefick, B. Parrish, and P. Robson, “Realising the potential of demand-side response to 2025: A focus on small energy users (summary report).” https://assets.publishing.service.gov.uk/government/uploads/system/uploads/attachment_data/file/657144/DSR_Summary_Report.pdf, 2017. [Last Accessed: Jun. 7 2020].
- [2] Intergovernmental Panel on Climate Change, “Global warming of 1.5°.” <https://www.ipcc.ch/sr15/>, Oct. 2018. [Last Accessed: Jun. 12 2020].
- [3] Government of the United Kingdom, “The Clean Growth Strategy.” https://assets.publishing.service.gov.uk/government/uploads/system/uploads/attachment_data/file/700496/clean-growth-strategy-correction-april-2018.pdf, 2017. [Last Accessed: Jun. 12 2020].
- [4] “Solar Photovoltaics Deployment in the UK.” <https://www.gov.uk/government/statistics/solar-photovoltaics-deployment#history>. [Last Accessed: Jun. 12 2020].
- [5] “Electric car market statistics.” <https://www.nextgreencar.com/electric-cars/statistics/>, 2020. [Last Accessed: Jun. 12 2020].
- [6] S. Y. R. Hui, C. K. Lee, and F. F. Wu, “Electric springs: A new smart grid technology,” *IEEE Transactions on Smart Grid*, vol. 3, no. 3, pp. 1552–1561, 2012.
- [7] W. Cao, J. Wu, N. Jenkins, C. Wang, and T. Green, “Operating principle of soft open points for electrical distribution network operation,” *Applied Energy*, vol. 164, pp. 245–257, 2016.
- [8] T. Frost, P. D. Mitcheson, and T. C. Green, “Power electronic voltage regulation in lv distribution networks,” in *Power Electronics for Distributed Generation Systems (PEDG), 2015 IEEE 6th International Symposium on*, pp. 1–7, IEEE, 2015.
- [9] X. Chen, Y. Hou, S.-C. Tan, C.-K. Lee, and S. Y. R. Hui, “Mitigating voltage and frequency fluctuation in microgrids using electric springs,” *IEEE Transactions on Smart Grid*, vol. 6, no. 2, pp. 508–515, 2015.
- [10] X. Luo, Z. Akhtar, C. K. Lee, B. Chaudhuri, S. C. Tan, and S. Y. R. Hui, “Distributed voltage control with electric springs: Comparison with statcom,” *IEEE Transactions on Smart Grid*, vol. 6, no. 1, pp. 209–219, 2015.

- [11] Z. Akhtar, B. Chaudhuri, and S. Y. R. Hui, "Primary frequency control contribution from smart loads using reactive compensation," *IEEE Transactions on Smart Grid*, vol. 6, no. 5, pp. 2356–2365, 2015.
- [12] D. Chakravorty, B. Chaudhuri, and S. Y. R. Hui, "Rapid frequency response from smart loads in great britain power system," *IEEE Transactions on Smart Grid*, vol. 8, no. 5, pp. 2160–2169, 2017.
- [13] T. Liu, D. J. Hill, and C. Zhang, "Non-disruptive load-side control for frequency regulation in power systems," *IEEE transactions on smart grid*, vol. 7, no. 4, pp. 2142–2153, 2016.
- [14] C. Zhang, T. Liu, and D. J. Hill, "Granulated load-side control of power systems with electric spring aggregators," in *2017 IEEE Manchester PowerTech*, pp. 1–6, IEEE, 2017.
- [15] Y. Zheng, C. Zhang, D. J. Hill, and K. Meng, "Consensus control of electric spring using back-to-back converter for voltage regulation with ultra-high renewable penetration," *Journal of Modern Power Systems and Clean Energy*, vol. 5, no. 6, pp. 897–907, 2017.
- [16] Q. Wang, M. Cheng, Y. Jiang, W. Zuo, and G. Buja, "A simple active and reactive power control for applications of single-phase electric springs," *IEEE Transactions on Industrial Electronics*, vol. 65, no. 8, pp. 6291–6300, 2018.
- [17] X. Che, T. Wei, Q. Huo, and D. Jia, "A general comparative analysis of static synchronous compensator and electric spring," in *2014 IEEE Conference and Expo Transportation Electrification Asia-Pacific (ITEC Asia-Pacific)*, pp. 1–5, IEEE, 2014.
- [18] J. Soni, K. Krishnanand, and S. Panda, "Load-side demand management in buildings using controlled electric springs," in *IECON 2014-40th Annual Conference of the IEEE Industrial Electronics Society*, pp. 5376–5381, IEEE, 2014.
- [19] V. Kanakesh, B. Sen, J. Soni, and S. Panda, "Control strategies for electric spring in an islanded microgrid: A comparative evaluation," in *Future Energy Electronics Conference and ECCE Asia (IFEEEC 2017-ECCE Asia), 2017 IEEE 3rd International*, pp. 1714–1718, IEEE, 2017.
- [20] Q. Wang, M. Cheng, Z. Chen, and Z. Wang, "Steady-state analysis of electric springs with a novel δ control," *IEEE Transactions on Power Electronics*, vol. 30, no. 12, pp. 7159–7169, 2015.
- [21] J. Soni and S. K. Panda, "Electric spring for voltage and power stability and power factor correction," *IEEE Transactions on Industry Applications*, vol. 53, no. 4, pp. 3871–3879, 2017.
- [22] C. K. Lee and S. Y. R. Hui, "Reduction of energy storage requirements in future smart grid using electric springs," *IEEE Transactions on Smart Grid*, vol. 4, no. 3, pp. 1282–1288, 2013.

- [23] S. Yan, S. C. Tan, C. K. Lee, B. Chaudhuri, and S. Y. R. Hui, "Electric springs for reducing power imbalance in three-phase power systems," *IEEE Transactions on Power Electronics*, vol. 30, no. 7, pp. 3601–3609, 2015.
- [24] S. Yan, S. C. Tan, C. K. Lee, B. Chaudhuri, and S. Y. R. Hui, "Use of smart loads for power quality improvement," *IEEE Journal of Emerging and Selected Topics in Power Electronics*, vol. 5, no. 1, pp. 504–512, 2017.
- [25] Q. Wang, M. Cheng, and Y. Jiang, "Harmonics suppression for critical loads using electric springs with current-source inverters," *IEEE Journal of emerging and selected topics in power electronics*, vol. 4, no. 4, pp. 1362–1369, 2016.
- [26] K. Krishnanand, S. M. F. Hasani, J. Soni, and S. K. Panda, "Neutral current mitigation using controlled electric springs connected to microgrids within built environment," in *2014 IEEE Energy Conversion Congress and Exposition (ECCE)*, pp. 2947–2951, IEEE, 2014.
- [27] P. Du, N. Lu, and H. Zhong, *Demand Response in Smart Grids*. Springer International Publishing, July 2019.
- [28] Ofgem, "Upgrading our energy system: Smart systems and flexibility plan." https://assets.publishing.service.gov.uk/government/uploads/system/uploads/attachment_data/file/633442/upgrading-our-energy-system-july-2017.pdf, 2017. [Last Accessed: Jun. 7 2020].
- [29] D. W. Caves, L. R. Christensen, and J. A. Herriges, "Consistency of residential customer response in time-of-use electricity pricing experiments," *Journal of Econometrics*, vol. 26, no. 1-2, pp. 179–203, 1984.
- [30] Rocky Mountain Institute, "Demand Response: An Introduction (Overview of Programs, Technologies, and Lessons Learned)," tech. rep., Apr. 2006.
- [31] F. A. Wolak, "Residential customer response to real-time pricing: The anaheim critical peak pricing experiment," 2007.
- [32] K. Herter, "Residential implementation of critical-peak pricing of electricity," *Energy policy*, vol. 35, no. 4, pp. 2121–2130, 2007.
- [33] H. Allcott, "Real time pricing and electricity markets," 2009.
- [34] "Power Smart Pricing." <http://www.powersmartpricing.org/prices/>, 2015. [Last Accessed: Jun. 12 2020].
- [35] Department for Business, Energy and Industrial Strategy, "Smart meter roll-out cost-benefit analysis: Part 1." <https://www.gov.uk/government/publications/smart-meter-roll-out-gb-cost-benefit-analysis>, 2016. [Last Accessed: Jun. 7 2020].
- [36] R. Carmichael, R. Gross, and A. Rhodes, "Unlocking the potential of residential electricity consumer engagement with demand response," *Energy Futures Lab (Imperial College London), Briefing Paper*, 2018.

- [37] HM Government, “The road to zero next steps towards cleaner road transport and delivering our industrial strategy.” https://assets.publishing.service.gov.uk/government/uploads/system/uploads/attachment_data/file/739460/road-to-zero.pdf, 2018. [Last Accessed: Jun. 8 2020].
- [38] OVO Energy and Imperial College London, “Blueprint for a post-carbon society: How residential flexibility is key to decarbonising power, heat and transport.” <https://www.ovoenergy.com/binaries/content/assets/documents/pdfs/newsroom/blueprint-for-a-post-carbon-society-how-residential-flexibility-is-key-to-decarbonising-power-heat-and-transport/blueprintforapostcarbonsocietypdf-compressed.pdf>, 2018. [Last Accessed: Jun. 8 2020].
- [39] National Grid, “Future energy scenarios fes 2018.” <http://fes.nationalgrid.com/fes-document/>, 2018. [Last Accessed: Jun. 8 2020].
- [40] K. Bhattacharya *et al.*, “Competitive framework for procurement of interruptible load services,” *IEEE Transactions on Power systems*, vol. 18, no. 2, pp. 889–897, 2003.
- [41] K.-Y. Huang and Y.-C. Huang, “Integrating direct load control with interruptible load management to provide instantaneous reserves for ancillary services,” *IEEE Transactions on power systems*, vol. 19, no. 3, pp. 1626–1634, 2004.
- [42] A. Zakariazadeh, O. Homaei, S. Jadid, and P. Siano, “A new approach for real time voltage control using demand response in an automated distribution system,” *Applied Energy*, vol. 117, pp. 157–166, 2014.
- [43] D. Wang, S. Parkinson, W. Miao, H. Jia, C. Crawford, and N. Djilali, “Online voltage security assessment considering comfort-constrained demand response control of distributed heat pump systems,” *Applied Energy*, vol. 96, pp. 104–114, 2012.
- [44] E. Dehnavi and H. Abdi, “Determining optimal buses for implementing demand response as an effective congestion management method,” *IEEE Transactions on Power Systems*, vol. 32, no. 2, pp. 1537–1544, 2016.
- [45] A. Haque, M. Rahman, P. Nguyen, and F. Bliet, “Smart curtailment for congestion management in lv distribution network,” in *2016 IEEE Power and Energy Society General Meeting (PESGM)*, pp. 1–5, IEEE, 2016.
- [46] D. Angeli and P.-A. Kountouriotis, “A stochastic approach to “dynamic-demand” refrigerator control,” *IEEE Transactions on control systems technology*, vol. 20, no. 3, pp. 581–592, 2011.
- [47] M. Aunedi, P.-A. Kountouriotis, J. O. Calderon, D. Angeli, and G. Strbac, “Economic and environmental benefits of dynamic demand in providing frequency regulation,” *IEEE Transactions on Smart Grid*, vol. 4, no. 4, pp. 2036–2048, 2013.
- [48] K. Schneider, F. Tuffner, J. Fuller, and R. Singh, “Evaluation of conservation voltage reduction (CVR) on a national level.” https://www.pnnl.gov/main/publications/external/technical_reports/PNNL-19596.pdf, 2010. [Last Accessed: Jun. 12 2020].
- [49] A. Ballanti and L. F. Ochoa, “Voltage-led load management in whole distribution networks,” *IEEE Transactions on Power Systems*, vol. 33, no. 2, pp. 1544–1554, 2018.

- [50] G. De Carne, G. Buticchi, M. Liserre, and C. Vournas, "Real-time primary frequency regulation using load power control by smart transformers," *IEEE Transactions on Smart Grid*, vol. 10, no. 5, pp. 5630–5639, 2019.
- [51] M. Farrokhhabadi, C. A. Cañizares, and K. Bhattacharya, "Frequency control in isolated/islanded microgrids through voltage regulation," *IEEE Transactions on Smart Grid*, vol. 8, no. 3, pp. 1185–1194, 2017.
- [52] R. Silversides, T. Green, and M. M. C. Merlin, "A high density converter for mid feeder voltage regulation of low voltage distribution feeders," in *2014 IEEE Energy Conversion Congress and Exposition (ECCE)*, pp. 1972–1978, Sep. 2014.
- [53] Z. Akhtar, M. Opatovsky, B. Chaudhuri, and S. Y. R. Hui, "Comparison of point-of-load versus mid-feeder compensation in lv distribution networks with high penetration of solar photovoltaic generation and electric vehicle charging stations," *IET Smart Grid*, vol. 2, no. 2, pp. 283–292, 2019.
- [54] C. K. Lee, B. Chaudhuri, and S. Y. Hui, "Hardware and control implementation of electric springs for stabilizing future smart grid with intermittent renewable energy sources," *IEEE Journal of Emerging and Selected Topics in Power Electronics*, vol. 1, no. 1, pp. 18–27, 2013.
- [55] C. K. Lee, N. R. Chaudhuri, B. Chaudhuri, and S. R. Hui, "Droop control of distributed electric springs for stabilizing future power grid," *IEEE Transactions on Smart Grid*, vol. 4, no. 3, pp. 1558–1566, 2013.
- [56] J. G. Nielsen, M. Newman, H. Nielsen, and F. Blaabjerg, "Control and testing of a dynamic voltage restorer (dvr) at medium voltage level," *IEEE Transactions on Power Electronics*, vol. 19, pp. 806–813, May 2004.
- [57] S.-C. Tan, C. K. Lee, and S. Hui, "General steady-state analysis and control principle of electric springs with active and reactive power compensations," *IEEE Transactions on Power Electronics*, vol. 28, no. 8, pp. 3958–3969, 2013.
- [58] S. Yan, C.-K. Lee, T. Yang, K.-T. Mok, S.-C. Tan, B. Chaudhuri, and S. R. Hui, "Extending the operating range of electric spring using back-to-back converter: hardware implementation and control," *IEEE Transactions on Power Electronics*, vol. 32, no. 7, pp. 5171–5179, 2017.
- [59] H. Fujita and H. Akagi, "The unified power quality conditioner: the integration of series-and shunt-active filters," *IEEE transactions on power electronics*, vol. 13, no. 2, pp. 315–322, 1998.
- [60] https://powerperfector.com/case_studies/, note = [Last Accessed: Jun. 12 2020].
- [61] Z. Akhtar, B. Chaudhuri, and S. Y. R. Hui, "Smart loads for voltage control in distribution networks," *IEEE Transactions on Smart Grid*, vol. 8, no. 2, pp. 937–946, 2017.
- [62] D. Chakravorty, Z. Akhtar, B. Chaudhuri, and S. Y. R. Hui, "Comparison of primary frequency control using two smart load types," in *Power and Energy Society General Meeting (PESGM), 2016*, pp. 1–5, IEEE, 2016.

- [63] D. Chakravorty, B. Chaudhuri, and S. Hui, "Estimation of aggregate reserve with point-of-load voltage control," *IEEE Transactions on Smart Grid*, 2017. in Early Access.
- [64] L. P. Kunjumammed, B. C. Pal, C. Oates, and K. J. Dyke, "Electrical oscillations in wind farm systems: Analysis and insight based on detailed modeling," *IEEE Transactions on Sustainable Energy*, vol. 7, no. 1, pp. 51–62, 2016.
- [65] A. A. Aquino-Lugo, R. Klump, and T. J. Overbye, "A control framework for the smart grid for voltage support using agent-based technologies," *IEEE Transactions on Smart Grid*, vol. 2, pp. 173–180, March 2011.
- [66] M. Zeraati, M. E. Hamedani Golshan, and J. M. Guerrero, "A consensus-based cooperative control of pev battery and pv active power curtailment for voltage regulation in distribution networks," *IEEE Transactions on Smart Grid*, vol. 10, pp. 670–680, Jan 2019.
- [67] P. Jahangiri and D. C. Aliprantis, "Distributed volt/var control by pv inverters," *IEEE Transactions on Power Systems*, vol. 28, pp. 3429–3439, Aug 2013.
- [68] N. R. Chaudhuri, C. K. Lee, B. Chaudhuri, and S. R. Hui, "Dynamic modeling of electric springs," *IEEE Transactions on Smart Grid*, vol. 5, no. 5, pp. 2450–2458, 2014.
- [69] Y. Yang, S.-S. Ho, S.-C. Tan, and S.-Y. R. Hui, "Small-signal model and stability of electric springs in power grids," *IEEE Transactions on Smart Grid*, vol. 9, no. 2, pp. 857–865, 2016.
- [70] R. Majumder, B. Chaudhuri, A. Ghosh, R. Majumder, G. Ledwich, and F. Zare, "Improvement of stability and load sharing in an autonomous microgrid using supplementary droop control loop," *IEEE transactions on power systems*, vol. 25, no. 2, pp. 796–808, 2010.
- [71] N. Pogaku, M. Prodanovic, and T. C. Green, "Modeling, analysis and testing of autonomous operation of an inverter-based microgrid," *IEEE Transactions on power electronics*, vol. 22, no. 2, pp. 613–625, 2007.
- [72] Y. Wang, X. Wang, Z. Chen, and F. Blaabjerg, "Small-signal stability analysis of inverter-fed power systems using component connection method," *IEEE Transactions on Smart Grid*, vol. 9, no. 5, pp. 5301–5310, 2017.
- [73] X. Guo, Z. Lu, B. Wang, X. Sun, L. Wang, and J. M. Guerrero, "Dynamic phasors-based modeling and stability analysis of droop-controlled inverters for microgrid applications," *IEEE Transactions on Smart Grid*, vol. 5, no. 6, pp. 2980–2987, 2014.
- [74] A. U. Krismanto and N. Mithulananthan, "Identification of modal interaction and small signal stability in autonomous microgrid operation," *IET Generation, Transmission & Distribution*, vol. 12, no. 1, pp. 247–257, 2017.
- [75] N. Bottrell, M. Prodanovic, and T. C. Green, "Dynamic stability of a microgrid with an active load," *IEEE Transactions on Power Electronics*, vol. 28, no. 11, pp. 5107–5119, 2013.

- [76] L. Liang, Y. Hou, D. J. Hill, and S. Y. R. Hui, "Enhancing Resilience of Microgrids with Electric Springs," *IEEE Transactions on Smart Grid*, vol. 9, no. 3, pp. 2235–2247, 2018.
- [77] L. Liang, Y. Hou, and D. J. Hill, "Enhancing Flexibility of An Islanded Microgrid with Electric Springs," *IEEE Transactions on Smart Grid*, 2017. in Early Access.
- [78] L. Zhu and D. J. Hill, "Modeling and Stability of Microgrids with Smart Loads," *IFAC-PapersOnLine*, vol. 50, no. 1, pp. 10021–10026, 2017.
- [79] J. E. Ormrod, "Harmonic state space modelling of voltage source converters," 2013.
- [80] J. Kwon, X. Wang, F. Blaabjerg, C. L. Bak, V.-S. Sularea, and C. Busca, "Harmonic interaction analysis in a grid-connected converter using harmonic state-space (hss) modeling," *IEEE Transactions on Power Electronics*, vol. 32, no. 9, pp. 6823–6835, 2017.
- [81] A. J. Collin, G. Tsagarakis, A. E. Kiprakis, and S. McLaughlin, "Development of low-voltage load models for the residential load sector," *IEEE Transactions on Power Systems*, vol. 29, no. 5, pp. 2180–2188, 2014.
- [82] P. Kundur, N. J. Balu, and M. G. Lauby, *Power system stability and control*, vol. 7. New York, NY, USA: McGraw-hill, 1994.
- [83] D. Das, D. Kothari, and A. Kalam, "Simple and efficient method for load flow solution of radial distribution networks," *International Journal of Electrical Power & Energy Systems*, vol. 17, no. 5, pp. 335–346, 1995.
- [84] BS EN 50160, "Voltage characteristics of electricity supplied by public electricity networks," tech. rep., July 2004.
- [85] <https://www.energy.ca.gov/programs-and-topics/topics/renewable-energy/solar-equipment-lists>. [Last Accessed: Jun. 13 2020].
- [86] I. Richardson, M. Thomson, D. Infield, and C. Clifford, "Domestic electricity use: A high-resolution energy demand model," *Energy & Buildings*, vol. 42, no. 10, pp. 1878–1887, 2010.
- [87] Andrea Ballanti and Luis Ochoa, "WP2 PartA - Final Report 'Off-Line Capability Assessment'." <https://www.semanticscholar.org/paper/Title-%3A-WP-2-Part-A-Final-Report-%E2%80%9COff-Line-%E2%80%9D/8ab7e9466319f973a6ca2981349abc1cd0f65f6d>, 2015. [Last Accessed: Jun. 13 2020].
- [88] CIGRE Working Group C4.605, Rep.5, "Modeling and Aggregation of Loads in Flexible Power Networks," tech. rep., Feb. 2014.
- [89] E. UK Department for Business and I. Strategy. <https://www.statista.com/statistics/426988/united-kingdom-uk-heating-methods/>. [Last Accessed: Jun. 13 2020].
- [90] CIGRE Task Force C6.04, "Benchmark Systems for Network Integration of Renewable and Distributed Energy Resources," tech. rep., Apr. 2014.

- [91] R. Fu, D. Chung, T. Lowder, D. Feldman, K. Ardani, R. Fu, D. Chung, T. Lowder, D. Feldman, and K. Ardani, “U.S. Solar Photovoltaic System Cost Benchmark: Q1 2018,” tech. rep., Sept. 2018.
- [92] National Grid, “STOR Annual Market Report 2016-2017 Data.” <https://www.nationalgrideso.com/industry-information/balancing-services/reserve-services/short-term-operating-reserve-stor?market-information=&order=title&page=0&search=&sort=asc>, 2017. [Last Accessed: Jun. 13 2020].
- [93] L. Badesa, F. Teng, and G. Strbac, “Simultaneous scheduling of multiple frequency services in stochastic unit commitment,” *IEEE Transactions on Power Systems*, 2019.
- [94] “System Needs and Product Strategy,” report, National Grid, 2017.
- [95] National Grid, “Future Energy Scenarios,” tech. rep.
- [96] “United Kingdom Generic Distribution System.” <https://github.com/sedg/ukgds>. [Last Accessed: Jun. 13 2020].
- [97] Department of Energy and Climate Change, “Energy Consumption in the UK (ECUK) 2016 Data Tables,” tech. rep., 2014.
- [98] A. Navarro, L. F. Ochoa, and P. Mancarella, “Learning from residential load data: Impacts on lv network planning and operation,” in *2012 Sixth IEEE/PES Transmission and Distribution: Latin America Conference and Exposition (T&D-LA)*, pp. 1–8, IEEE, 2012.
- [99] ELEXON, “Load Profiles and their use in Electricity Settlement,” tech. rep., Nov. 2013.
- [100] F. Teng, M. Aunedi, and G. Strbac, “Benefits of flexibility from smart electrified transportation and heating in the future UK electricity system,” *Applied energy*, vol. 167, pp. 420–431, 2016.
- [101] Northern Powergrid, “An Application Guide for using Load Drop Compensation on HV Systems,” tech. rep., Jan. 2018.
- [102] “Rural population and migration statistics.” <https://www.gov.uk/government/publications/rural-population-and-migration/rural-population-201415>. [Last Accessed: Jun. 13 2020].
- [103] H. Arbabi and M. Mayfield, “Urban and rural—population and energy consumption dynamics in local authorities within England and Wales,” *Buildings*, vol. 6, no. 3, p. 34, 2016.
- [104] A. Sturt and G. Strbac, “Efficient stochastic scheduling for simulation of wind-integrated power systems,” *IEEE Transactions on Power Systems*, vol. 27, no. 1, pp. 323–334, 2012.
- [105] F. Teng, V. Trovato, and G. Strbac, “Stochastic scheduling with inertia-dependent fast frequency response requirements,” *IEEE Transactions on Power Systems*, vol. 31, no. 2, pp. 1557–1566, 2016.

- [106] UK Power Networks, “Conflicts and synergies of demand side response.” <https://innovation.ukpowernetworks.co.uk/wp-content/uploads/2019/05/A5-Conflicts-and-Synergies-of-Demand-Side-Response.pdf>, 2014. [Last Accessed: Jun. 10 2020].
- [107] “FICO Xpress BCL Reference Manual.” <https://www.msi-jp.com/xpress/learning/square/bcl-2015.pdf>. [Last Accessed: Jun. 13 2020].
- [108] “Technical Report on the events of 9 August 2019,” report, National Grid ESO, 2019.
- [109] T. Chen, J. Guo, B. Chaudhuri, and R. S. Y. Hui, “Virtual inertia from smart loads,” *IEEE Transactions on Smart Grid*, 2020. in Early Access.
- [110] J. Fang, H. Li, Y. Tang, and F. Blaabjerg, “On the inertia of future more-electronics power systems,” *IEEE Journal of Emerging and Selected Topics in Power Electronics*, vol. 7, no. 4, pp. 2130–2146, 2018.
- [111] J. Brisebois and N. Aubut, “Wind farm inertia emulation to fulfill hydro-québec’s specific need,” in *2011 IEEE Power and Energy Society General Meeting*, pp. 1–7, IEEE, 2011.
- [112] F. Blaabjerg and K. Ma, “Future on power electronics for wind turbine systems,” *IEEE Journal of emerging and selected topics in power electronics*, vol. 1, no. 3, pp. 139–152, 2013.
- [113] G. Lalor, A. Mullane, and M. O’Malley, “Frequency control and wind turbine technologies,” *IEEE Transactions on power systems*, vol. 20, no. 4, pp. 1905–1913, 2005.
- [114] A. F. Hoke, M. Shirazi, S. Chakraborty, E. Muljadi, and D. Maksimovic, “Rapid active power control of photovoltaic systems for grid frequency support,” *IEEE Journal of Emerging and Selected Topics in Power Electronics*, vol. 5, no. 3, pp. 1154–1163, 2017.
- [115] P. Zarina, S. Mishra, and P. Sekhar, “Deriving inertial response from a non-inertial pv system for frequency regulation,” in *2012 IEEE International Conference on Power Electronics, Drives and Energy Systems (PEDES)*, pp. 1–5, IEEE, 2012.
- [116] J. Fang, H. Li, Y. Tang, and F. Blaabjerg, “Distributed power system virtual inertia implemented by grid-connected power converters,” *IEEE Transactions on Power Electronics*, vol. 33, no. 10, pp. 8488–8499, 2017.
- [117] R. H. S. Yuen and E. Waffenschmidt, “Power supply supporting virtual inertia for grid control (micro-spring converter),” Jan. 31 2019. US Patent App. 16/071,665.
- [118] A. Junyent-Ferr, Y. Pipelzadeh, and T. C. Green, “Blending hvdc-link energy storage and offshore wind turbine inertia for fast frequency response,” *IEEE Transactions on sustainable energy*, vol. 6, no. 3, pp. 1059–1066, 2014.
- [119] A. Delavari and I. Kamwa, “Virtual inertia-based load modulation for power system primary frequency regulation,” in *2017 IEEE Power & Energy Society General Meeting*, pp. 1–5, IEEE, 2017.

- [120] Z. Wang, Y.-Q. Bao, C. Shen, and C. Chen, "Power system virtual inertia implemented by thermostatically controlled loads," in *2019 IEEE Innovative Smart Grid Technologies-Asia (ISGT Asia)*, pp. 604–607, IEEE, 2019.
- [121] National Grid, "Nets security and quality of supply standard." <https://www.nationalgrideso.com/codes/security-and-qualitysupply-standards>. [Last Accessed: Jun. 13 2020].
- [122] "Changes to the distribution code and engineering recommendation g59: Generator connection requirements." <https://www.ofgem.gov.uk/publications-and-updates/changes-distribution-code-and-engineering-recommendation-g59-generator-connection-requirements-review-engineering-recommendation-g59-3-1>. [Last Accessed: Jun. 13 2020].
- [123] K. Yeager and J. Willis, "Modeling of emergency diesel generators in an 800 megawatt nuclear power plant," *IEEE Transactions on Energy Conversion*, vol. 8, no. 3, pp. 433–441, 1993.
- [124] N. Chaudhuri, B. Chaudhuri, R. Majumder, and A. Yazdani, *Multi-terminal direct-current grids: Modeling, analysis, and control*. John Wiley & Sons, 2014.
- [125] Y. Wang, X. Wang, Z. Chen, and F. Blaabjerg, "Small-signal stability analysis of inverter-fed power systems using component connection method," *IEEE Transactions on Smart Grid*, vol. 9, no. 5, pp. 5301–5310, 2018.
- [126] A. Yazdani and R. Iravani, *Voltage-sourced converters in power systems: modeling, control, and applications*. John Wiley & Sons, 2010.
- [127] Q. Huang and R. Kaushik, "An improved delayed signal cancellation pll for fast grid synchronization under distorted and unbalanced grid condition," *IEEE Transactions on Industry Applications*, vol. PP, no. 99, pp. 1–1, 2017.
- [128] N. Bottrell, M. Prodanovic, and T. C. Green, "Dynamic stability of a microgrid with an active load," *IEEE Transactions on Power Electronics*, vol. 28, pp. 5107–5119, Nov 2013.
- [129] N. Kroutikova, C. a. Hernandez-Aramburo, and T. C. Green, "State-space model of grid-connected inverters under current control mode," *IET Electric Power Applications*, vol. 1, pp. 329–338, May 2007.
- [130] C. C. Chang, D. Gorinevsky, and S. Lall, "Dynamical and voltage profile stability of inverter-connected distributed power generation," *IEEE Transactions on Smart Grid*, vol. 5, pp. 2093–2105, July 2014.
- [131] N. Pogaku, M. Prodanovic, and T. C. Green, "Modeling, analysis and testing of autonomous operation of an inverter-based microgrid," *IEEE Transactions on Power Electronics*, vol. 22, pp. 613–625, March 2007.
- [132] J. Guo, B. Chaudhuri, and S. Y. R. Hui, "Flexible demand through point-of-load voltage control in domestic sector," *IEEE Transactions on Smart Grid*, 2018. in Early Access.

- [133] “Voltage characteristics of electricity supplied by public distribution systems,” *BS EN Standard*, vol. 50160, 1995.
- [134] G. Delille, L. Capely, D. Souque, and C. Ferrouillat, “Experimental validation of a novel approach to stabilize power system frequency by taking advantage of load voltage sensitivity,” in *Proc. of IEEE PowerTech*, Eindhoven, Netherlands, June 2015.
- [135] A. Emadi, “Modeling of power electronic loads in ac distribution systems using the generalized state-space averaging method,” *IEEE transactions on Industrial Electronics*, vol. 51, no. 5, pp. 992–1000, 2004.
- [136] D. Dong, B. Wen, P. Mattavelli, D. Boroyevich, and Y. Xue, “Modeling and design of islanding detection using phase-locked loops in three-phase grid-interface power converters,” *IEEE Journal of Emerging and Selected Topics in Power Electronics*, vol. 2, no. 4, pp. 1032–1040, 2014.
- [137] J. He and Y. W. Li, “Analysis, design, and implementation of virtual impedance for power electronics interfaced distributed generation,” *IEEE Transactions on Industry Applications*, vol. 47, no. 6, pp. 2525–2538, 2011.
- [138] P. N. Vovos, A. E. Kiprakis, A. R. Wallace, and G. P. Harrison, “Centralized and distributed voltage control: Impact on distributed generation penetration,” *IEEE Transactions on Power Systems*, vol. 22, pp. 476–483, Feb 2007.
- [139] J. Elizondo, R. Y. Zhang, J. K. White, and J. L. Kirtley, “Robust small signal stability for microgrids under uncertainty,” in *2015 IEEE 6th International Symposium on Power Electronics for Distributed Generation Systems (PEDG)*, pp. 1–8, IEEE, 2015.
- [140] Z. Miao, L. Piyasinghe, J. Khazaei, and L. Fan, “Dynamic phasor-based modeling of unbalanced radial distribution systems,” *IEEE transactions on power systems*, vol. 30, no. 6, pp. 3102–3109, 2015.

Appendix A

Derivation of Equation (2.2)

An electrical equivalent of a radial distribution network is given in Fig. A.1.

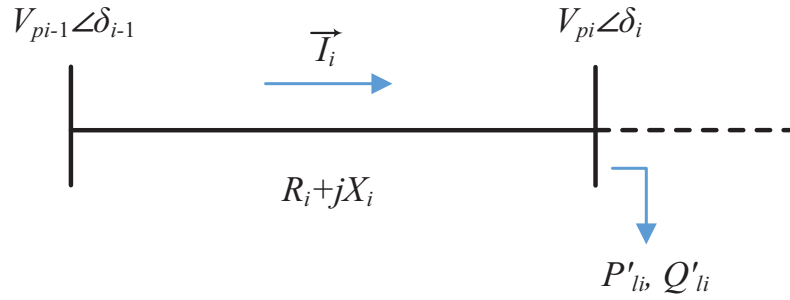


Fig. A.1 Electrical equivalent of a radial distribution network

The line current (\vec{I}_i) can be expressed by (A.1).

$$\vec{I}_i = \frac{V_{pi-1} \angle \delta_{i-1} - V_{pi} \angle \delta_i}{R_i + jX_i} = \frac{P'_{li} - jQ'_{li}}{V_{pi}^*} \quad (\text{A.1})$$

Therefore, we have:

$$V_{pi-1} V_{pi} \angle (\delta_{i-1} - \delta_i) - V_{pi}^2 = (P'_{li} - jQ'_{li}) (R_i + jX_i) \quad (\text{A.2})$$

Further, we have:

$$V_{pi-1} V_{pi} \cos(\delta_{i-1} - \delta_i) - V_{pi}^2 + j V_{pi-1} V_{pi} \sin(\delta_{i-1} - \delta_i) = (P'_{li} R_i + Q'_{li} X_i) + j (P'_{li} X_i - Q'_{li} R_i) \quad (\text{A.3})$$

(A.4) and (A.5) can be then obtained by separating the real and imaginary parts of (A.3).

$$V_{pi-1} V_{pi} \cos(\delta_{i-1} - \delta_i) = V_{pi}^2 + P'_{li} R_i + Q'_{li} X_i \quad (\text{A.4})$$

$$V_{pi-1} V_{pi} \sin (\delta_{i-1} - \delta_i) = P'_{li} X_i - Q'_{li} R_i \quad (\text{A.5})$$

(A.6) can be then obtained by squaring and adding (A.4) and (A.5).

$$V_{pi-1}^2 V_{pi}^2 = \left(V_{pi}^2 + P'_{li} R_i + Q'_{li} X_i \right)^2 + \left(P'_{li} X_i - Q'_{li} R_i \right)^2 \quad (\text{A.6})$$

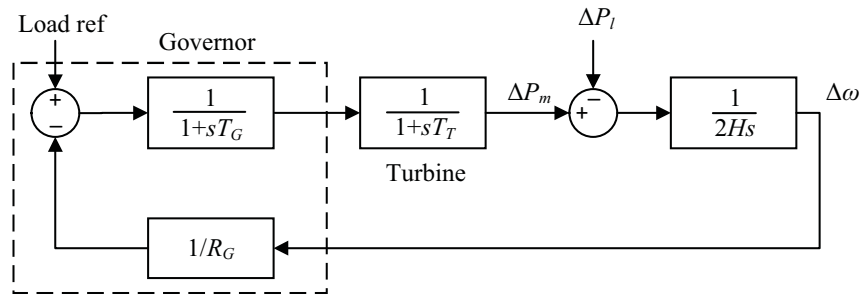
(A.6) can be reorganised as (A.7).

$$V_{pi}^4 + 2.0 \left[P'_{li} R_i + Q'_{li} X_i - 0.50 V_{pi-1}^2 \right] V_{pi}^2 + \left(R_i^2 + X_i^2 \right) \left(P_{li}'^2 + Q_{li}'^2 \right) = 0 \quad (\text{A.7})$$

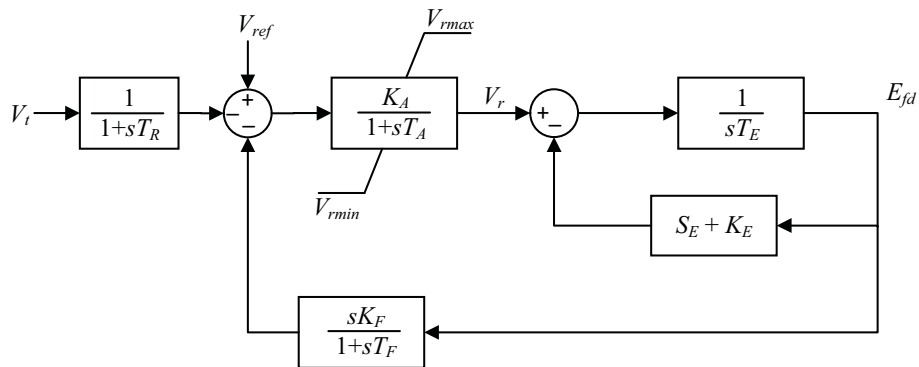
Equation (2.2) in Chapter 2 is then the positive solution of (A.7).

Appendix B

Summary of Generator Parameters



(a) Block diagram of the turbine and governor



(b) Block diagram of the excitation system (IEEE DC1A)

Fig. B.1 (a) Block diagram of the turbine and governor; (b) Block diagram of the excitation system (IEEE DC1A)

Table B.1 Parameters of the Isolated Microgrid (IMG)

Generator					
L_d	1.56	L_q	1.06	L'_d	0.296
$T_{do'}$	3.7	H	1.0716		
Turbine and Governor					
T_T	0.4	T_G	0.2	R_G	0.05
Excitation System					
T_R	0.02	K_A	46	T_A	0.06
K_F	0.05	T_F	1.5	K_E	0.05
T_E	0.46	V_{rmax}	1.0	V_{rmin}	-0.9

Note that the inductance parameters are in p.u. on machine base of 3.125 MVA, 2400 V. Time constants are in sec.

Appendix C

Equivalent DG Models

The configuration of an equivalent DG inverter for voltage regulation is given in Fig. C.1. Compared to the PVC-Q configuration shown in Fig. 5.1, the only difference is that the non-critical load has been removed here. The denotation and filter parameters are the same as that in Fig. 5.1.

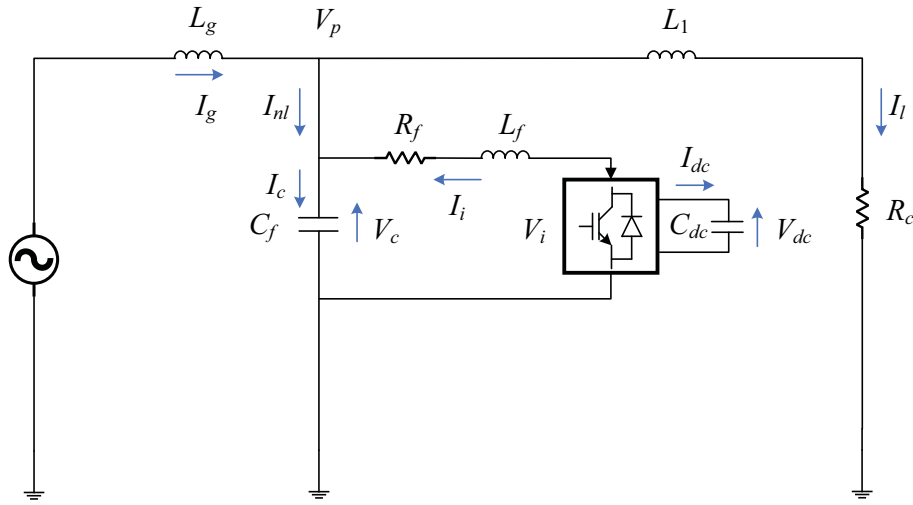


Fig. C.1 Equivalent DG configuration

The point-of-coupling (PoC) voltage control scheme for DG inverter is shown in Fig. C.2. Unlike the case with PVC-Q, the d -axis is now aligned with the PoC voltage ($V_p = V_{pd}$) to achieve decoupled control. The compensator (K_{vp}) is simply an integrator with $k_{ivp} = 6500$ and the theoretical maximum value of V_{cdmax} can be equal to the feeder-side voltage (peak value) i.e. $230\sqrt{2}$. The principle of control loop tuning is to allow similar phase margin (90°) with comparable bandwidth to that of PVC-Q. This can be backed up by the bode plot of the

open loop of PoC voltage control loop shown in Fig. C.3 along with the step response of the closed loop system.

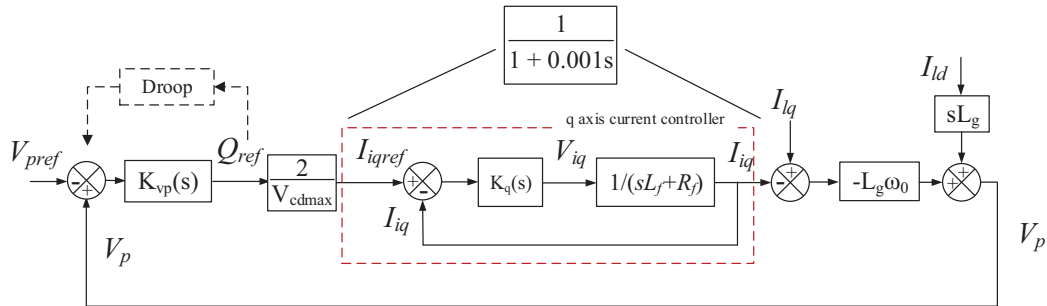


Fig. C.2 PoC voltage control scheme

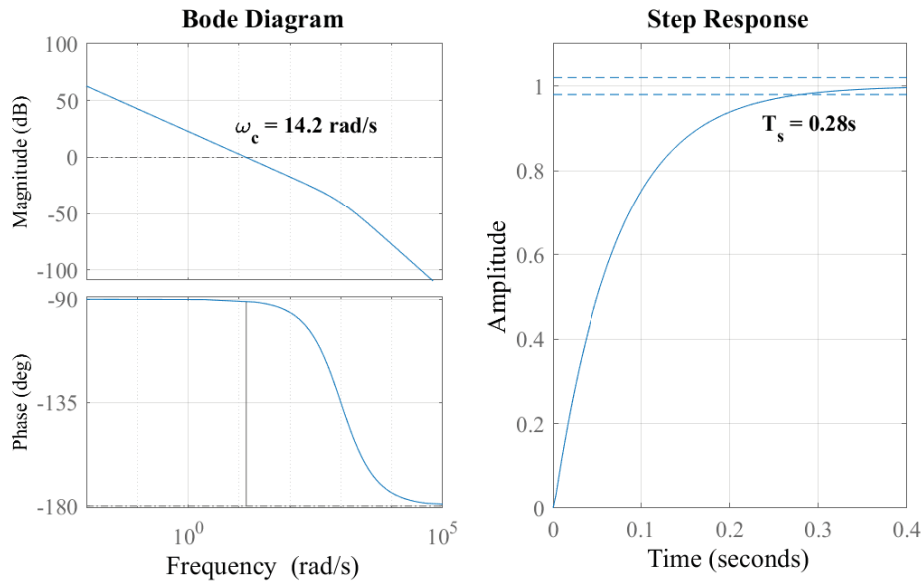


Fig. C.3 Bode plot and step response of the PoC voltage control loop

Appendix D

System Parameters

Table D.1 Parameters of the Isolated Microgrid (IMG)

Parameter	Value
Maximum power output P_{max}/Q_{max}	10kW/ 5kVar
Nominal power reference P_g^*/Q_g^*	5kW/ 0kVar
CDG frequency range	49.5Hz-50.5Hz
Droop gain m_1/m_2	6.28e-4 / 6.28e-4
Droop gain n_1/n_2	3.81e-3 / 3.81e-3
PI for voltage controller K_{pvg}/K_{ivg}	0.05 / 300
Time constant for current controller τ_g	0.5ms
Filter resistance/inductance [71]	0.1 Ω / 1.35mH
Filter capacitance [71]	50 μ F
Coupling inductance	0.5mH
Loads Ld1, Ld2 Z_{ll}/pf	50 Ω / 0.95
Line impedance (R_1/X_1) [71]	0.23 Ω / 0.1 Ω
Line impedance (R_2/X_2) [71]	0.35 Ω / 0.58 Ω

Table D.2 Parameters of the Smart Load

Parameter	Value
Nominal droop gain m_{SL}	0.02
PI for PLL K_{ppll}/K_{ipll}	0.3 / 0.5
Natural frequency & damping ratio for PLL's LPF	25 Hz / 0.707
PI for SeC's voltage controller K_{pvl}/K_{ivl}	0.05 / 50
PI for ShC's DC voltage controller K_{pdc}/K_{idc}	5 / 100
Time constant of current controllers τ_l	0.25ms
SeC's filter resistance/inductance R_{fse}/L_{fse} [54]	0.09 Ω / 500 μ H
SeC & ShC's filter capacitance C_{fse}, C_{fsh} [58]	13.2 μ F
ShC's filter resistance/inductance R_{fsh}/L_{fsh} [58]	0.09 Ω / 500 μ H
ShC's coupling inductance L_{csh} [58]	11mH
Rated DC link voltage/capacitor C_{dc} [58]	400V / 1500 \times 3 μ F
Load nominal active power P_{SL}^* /power factor	6kW/ 0.95
Power voltage sensitivity n_p/n_q [134]	1.5 / 2

Appendix E

Eigen Values and Participation Factors for IMG with a SL

Table E.1 State Variable Description II

No.	Component	Description
19-21	CDG1	voltage (dq) and current ($d - axis$) controllers
22-25		currents and voltages of the LC filter (dq)
26-27		currents of the coupling inductance (dq)
28-30	CDG2	voltage (dq) and current ($d - axis$) controllers
31-34		currents and voltages of the LC filter (dq)
35-36		currents of the coupling inductance (dq)
37-38	Line1	line currents (dq)
39-40	SeC	voltage and current controllers ($q - axis$)
41-44		currents and voltages of the LC filter (dq)
45-48	ShC	currents and voltages of the LC filter (dq)

Table E.2 Oscillatory Modes of the Test System (Case 3)

Mode No.		1	2	3	4	5	6	7	8	9	10	11	12	13	14	15	16
Frequency (Hz)		12.18	22.23	4.59	12.95	17.92	23.37	28.61	81.98	629.11	682.33	815.88	888.14	1937.23	2025.40	2039.52	2076.25
Damping (%)		7.53	16.15	88.42	81.17	43.75	48.36	30.87	12.79	16.77	17.91	14.01	14.04	16.18	15.46	15.51	15.44
Dominant States & Corresponding Participation Factor	1	1.00	0.06	0.28	0.09		0.11	0.19									
	2	0.95	0.06	0.47	0.11		0.12	0.19									
	3	0.12	0.13				0.15	0.69									
	4	0.72		0.20				0.24									
	5	0.69		0.34				0.26									
	6	0.16	0.06				0.12	0.76									
	7	0.09					0.05	0.91				0.41	0.44				
	8	0.10	0.06					1.00				0.41	0.44				
	9	0.06	0.26	1.00	0.40		0.24										
	10		0.43	0.39	0.98		1.00	0.13									
	11		0.25	0.14	1.00		0.82	0.10									
	12		0.53	0.16	0.42		0.85	0.12									
	13		0.44	0.22	0.64		0.79	0.09									
	14		0.31		0.17		0.32	0.11	0.24								
	15		1.00	0.07			0.43	0.15	0.05								
	16		0.05						1.00	0.06	0.07						
	17		0.64				0.38	0.17	0.42	0.06	0.07						
	18		0.32		0.10		0.27	0.14	0.66								
	19	0.06					0.10	0.75		0.15	0.11	0.08	0.07				
	20		0.16		0.07		0.23	0.40		0.14	0.12	0.08	0.07				
	21							0.12									
	22							0.20		0.79	0.66	0.60	0.52				
	23						0.08	0.14		0.76	0.68	0.60	0.52				
	24									0.83	0.81	1.00	0.99				
	25									0.80	0.82	1.00	1.00				
	26							0.26				0.14	0.15				
	27		0.08				0.10	0.19				0.14	0.15				
	28	0.06					0.06	0.75		0.18	0.14	0.07	0.05				
	29	0.05						0.60		0.17	0.14	0.07	0.05				
	30							0.12									
	31							0.19		0.95	0.80	0.50	0.43				
	32							0.21		0.93	0.82	0.50	0.43				
	33									1.00	0.97	0.83	0.82				
	34									0.98	1.00	0.82	0.82				
	35							0.25				0.12	0.12				
	36							0.28				0.11	0.12				
	37							0.16				0.09	0.09				
	38						0.06	0.12				0.09	0.09				
	39					1.00											
	40					1.00											
	41														1.00		0.96
	42														1.00		0.96
	43														0.99		1.00
	44														0.99		1.00
	45													0.58		0.99	
	46													0.96		0.59	
	47													0.58		1.00	
	48													1.00		0.62	